

PL-TR-96-2268

ENVIRONMENTAL GEOPHYSICAL AND SEISMIC STUDIES

**Steven Cardimona
David Harkrider
Stephan Koester
Victor Oancea
Brian Sullivan**

**Boston College
Institute for Scientific Research
Chestnut Hill, MA 02167**

30 June 1996

Scientific Report No. 1

19970205 044


Approved for public release; distribution unlimited




**PHILLIPS LABORATORY
Directorate of Geophysics
AIR FORCE MATERIEL COMMAND
HANSCOM AIR FORCE BASE, MA 01731-3010**

DTIC QUALITY INSPECTED 3

"This technical report has been reviewed and is approved for publication."


JAMES F. LEWKOWICZ
Contract Manager
Earth Sciences Division


JAMES F. LEWKOWICZ
Director
Earth Sciences Division

This report has been reviewed by the ESD Public Affairs Office (PA) and is releasable to the National Technical Information Service (NTIS).

Qualified requestors may obtain copies from the Defense Technical Information Center. All others should apply to the National Technical Information Service.

If your address has changed, or you wish to be removed from the mailing list, or if the addressee is no longer employed by your organization, please notify PL/IM, 29 Randolph Road, Hanscom AFB, MA 01731-3010. This will assist us in maintaining a current mailing list.

Do not return copies of this report unless contractual obligations or notices on a specific document requires that it be returned.

REPORT DOCUMENTATION PAGE			Form Approved OMB No. 0704-0188	
Public reporting burden for this collection of information is estimated to average 1 hour per response, including the time for reviewing instructions, searching existing data sources, gathering and maintaining the data needed, and completing and reviewing the collection of information. Send comments regarding this burden estimate or any other aspect of this collection of information, including suggestions for reducing this burden, to Washington Headquarters Services, Directorate for Information Operations and Reports, 1215 Jefferson Davis Highway, Suite 1204, Arlington, VA 22202-4302, and to the Office of Management and Budget, Paperwork Reduction Project (0704-0188), Washington, DC 20503.				
1. AGENCY USE ONLY (Leave blank)		2. REPORT DATE 30 June 1996		3. REPORT TYPE AND DATES COVERED Scientific No. 1
4. TITLE AND SUBTITLE ENVIRONMENTAL GEOPHYSICAL AND SEISMIC STUDIES			5. FUNDING NUMBERS PE 62101F PR 7600 TAGM WU AE Contract: F19628-95-C-0116	
6. AUTHOR(S) Steven Cardimona Victor Oancea David Harkrider Brian Sullivan Stephan Koester				
7. PERFORMING ORGANIZATION NAME(S) AND ADDRESS(ES) Boston College Institute for Scientific Research 140 Commonwealth Avenue Chestnut Hill, MA 02167			8. PERFORMING ORGANIZATION REPORT NUMBER	
9. SPONSORING/MONITORING AGENCY NAME(S) AND ADDRESS(ES) Phillips Laboratory 29 Randolph Road Hanscom AFB, MA 01731-3010 Contract Manager: James F. Lewkowicz/GPE			10. SPONSORING/MONITORING AGENCY REPORT NUMBER PL-TR-96-2268	
11. SUPPLEMENTARY NOTES				
12a. DISTRIBUTION / AVAILABILITY STATEMENT Approved for public release; distribution unlimited			12b. DISTRIBUTION CODE	
13. ABSTRACT (Maximum 200 words) Our research objectives are directed toward understanding electromagnetic propagation in dielectric media with conductive losses; investigation of the complementary use of both seismic and ground penetrating radar (GPR) technologies; investigating the use lattice-gas cellular automata methods to determine the characteristics of the ground water hydrology from noninvasive measurements made at the ground surface; the development of algorithms and approaches to create a new improved 5x5 global grid of Rayleigh and Love surface wave group velocities; and the collection and interpretation of seismic data to determine crustal structure. We teamed with scientists from the Earth Sciences Division of Phillips Laboratory (PL/GPE) to conduct a field test of the complementary technologies, seismic and GPR. Additionally, our researchers helped install a large-aperture seismic array surrounding the existing Pinedale Seismic Array to collect data for the purpose of characterizing the region geophysically.				
14. SUBJECT TERMS Electromagnetic propagation, dielectric media, Ground Penerating Radar (GPR), lattice- gas cellular automata methods, Raleigh and Love surface waves, large aperature seismic array			15. NUMBER OF PAGES 124	
			16. PRICE CODE	
17. SECURITY CLASSIFICATION OF REPORT UNCLASSIFIED	18. SECURITY CLASSIFICATION OF THIS PAGE UNCLASSIFIED	19. SECURITY CLASSIFICATION OF ABSTRACT UNCLASSIFIED	20. LIMITATION OF ABSTRACT SAR	

TABLE OF CONTENTS

1. INTRODUCTION	1
2. ELECTROMAGNETIC PROPAGATION IN DIELECTRIC MEDIA WITH CONDUCTIVE LOSSES	1
3. FIELD TEST OF THE COMPLEMENTARY TECHNOLOGIES: SEISMIC AND GPR	3
4. USE OF LATTICE-GAS CELLULAR AUTOMATA METHODS	4
5. SURFACE WAVE REGIONALIZATION	5
6. COLLECTION AND INTERPRETATION OF SEISMIC DATA TO DETERMINE CRUSTAL STRUCTURE	6
7. REFERENCES	8
8. APPENDIX	9
Preliminary Geophysical Characterization of Groundwater Remediation Field Laboratory, Dover Air Force Base, Delaware	10
Modeling Ground Penetrating Radar Transmission Properties in Conductive and Dispersive Media	11
Isotropic and Deviatoric Moment Inversion of Regional Surface Waves from Nevada Test Site Explosions: Implications for Yield Estimation and Seismic Discrimination	12
Preliminary Report on Surface Wave Regionalization	13
The Western Wyoming Seismic Refraction Profile	15
The Wyoming Large-Aperture Seismic Array	16
High-Resolution Seismic Reflection Survey at Dover AFB: A Comparison of Three Seismic Sources	17
Lattice Gas Cellular Automaton Models for Complex Dynamics	27
Data Report for the 1995 Wind River Mountains - Green River Basin, Wyoming Seismic Refraction Profile	97

1. INTRODUCTION

Our research objectives are directed toward understanding electromagnetic propagation in dielectric media with conductive losses; investigation of the complementary use of both seismic and ground penetrating radar (GPR) technologies; investigating the use of lattice-gas cellular automata methods to determine the characteristics of the ground water hydrology from non-invasive measurements made at the ground surface; the development of algorithms and approaches to create a new improved 5x5 global grid of Rayleigh and Love surface wave group velocities; and the collection and interpretation of seismic data to determine crustal structure. Oftentimes to properly evaluate a research application, it has to be tested with new and old seismic data bases and these results compared to those using existing approaches. Papers and abstracts of papers giving more detail on these efforts are included in the Appendix.

2. ELECTROMAGNETIC PROPAGATION IN DIELECTRIC MEDIA WITH CONDUCTIVE LOSSES

Understanding the propagation of radar signals in dielectric media with conductive losses is fundamental to GPR measurement interpretation. With a matrix method which describes plane-wave propagation, we have attempted to model electromagnetic and elastic waves in layered media. The Ray theory (Goodman, 1994) and finite difference techniques (Roberts, 1994) have been used to model electromagnetic waves in the earth; however dispersion and attenuation are non-trivial to incorporate into these time-domain algorithms. The main advantages of the matrix method are: (1) it is an exact solution; (2) it is developed in the frequency domain so that attenuation and dispersion effects are easily incorporated; (3) results are obtained in real-time on a workstation, without the requirement of a supercomputer for the calculations; and (4) extensions of the method model point scatterers and lateral heterogeneity in the earth media.

The matrix method for solving electromagnetic wave propagation outlined above is more generic than simply a solution to Maxwell's equation (Ursin, 1983). As a solution to an eigenvalue problem, the matrix method has been used to model elastic waves in a realistic earth (Kennett et al., 1979); e.g., we have used it to model compressional and shear waves in anisotropic media. The ability to model both radar and seismic data will greatly benefit the effort toward combining the two technologies.

Seismic waves are sensitive to the mechanical properties of the shallow subsurface, and radar is sensitive to the chemistry in the soils. In the course of research, we explored this difference between the data sets, and worked on understanding more of the complementary nature of the two non-invasive geophysical methods.

For synthesis of GPR, we arranged Maxwell's equations describing the physics of electromagnetic fields in general media into a system of equations to be solved as an eigenvalue problem. A differential system describes the propagation of the waves within the plane-wave approximation. The local eigenvalues of the system are the permissible vertical wavenumbers and include attenuation, while the local eigenvectors are used to match boundary conditions across interfaces between layers in the medium. The eigenvectors and eigenvalues are incorporated into a fundamental matrix describing propagating waves in the realistic earth, where vertical variations in permittivity, permeability and conductivity (as functions of frequency) can all be modeled

The fundamental matrix which describes the propagation of electromagnetic energy through a layered medium gives exactly the reflection and transmission response of the medium for a monochromatic plane wave at a given angle of incidence. Calculation of the amplitude variation has direct applicability to depth of penetration (skin-depth) studies; however, there is more potential information in the calculation since the matrix method is a full wave optics solution, where amplitude and phase are calculated together (as opposed to ray optics in which amplitude and phase are separate computational problems). We have explored ways to use the phase information in the GPR signal for detection of changes in physical quantities.

Calculation of the reflection response at many different frequencies, and integrating over those frequencies, gives synthetic radar signals in the time domain. We used a narrow-band zero-phase wavelet (a Ricker wavelet) as our source function for modeling radar data. The matrix method deals directly with the vector nature of the electric and magnetic fields, so that we can explore source and medium polarization effects. The most common form of ground penetrating radar data collection is in monostatic mode, which uses the geometry of a coincident source and receiver and yields vertical incidence radar returns. Calculation of the time-domain response at zero horizontal wavenumber generates a vertical-incidence synthetic radar record and for more than one receiver gives a synthetic monostatic radar record section. We introduced lateral variation in the earth model from one receiver to the next in order to approximate monostatic record sections over structures that are not horizontally planar.

The eigenvalue solution to wave propagation requires the medium be horizontally homogeneous. Introducing a perturbation to the laterally homogeneous background model is non-trivial, mainly in that it requires a convolution involving the response to the perturbation and the full wavefield itself. With a point scatterer as the perturbation to the background earth model, and assuming near-vertical incidence waves upon the scatterer, we hope to achieve analytic results for the convolution integral, giving an approximate form for the 3-D response of a scatterer that can be introduced into the 1-D matrix algorithm. With each scatterer acting as a 'Huygens' source, a superposition of the response from numerous scattering points can simulate laterally heterogeneous media.

3. FIELD TEST OF THE COMPLEMENTARY TECHNOLOGIES: SEISMIC AND GPR

Coupled with the computer modeling effort, there were field efforts in which we coordinated the collection of both ground penetrating radar and shallow high resolution seismic data at one or more sites. The data collected at these sites has allowed us to evaluate our near-surface Earth model and continue to fine tune it, when necessary, for the individual sites.

Our researchers and programmers are involved with the processing, analyzing and interpretation of geophysical data from field experiments at Dover AFB in 1995 and 1996 and at Hanscom AFB in 1996. The 1996 field tests collected only seismic refraction data as a check on seismic velocity structure and to 'image' the water table, something neither of the 1995 instruments was able to measure. The 1995 Dover data base consists of shallow seismic reflection records, ground penetrating radar, and electromagnetic induction measurements. Additionally, data taken by other researchers at Dover AFB in 1995 was exchanged. We created a data base of all the measurements collected, and distributed it to all the researchers. This data base includes terrain conductivity, elevation information, the seismic and radar data we collected, and the radar data collected by other researchers. Initial analysis of these measurements has been completed. This analysis provided: (1) comparison of seismic sources tested at Dover AFB for common mid-point reflection profiling and seismic characterization of the Groundwater Remediation Field Lab (GRFL) site; (2) description of the seismic data and the low frequency ground penetrating radar acquired at Dover AFB as one of the first direct comparisons of coincident shallow high resolution seismic data and ground penetrating radar that image similar targets; (3) comparison of ground penetrating radar collected by the two most commonly used systems with an array of source frequencies for each instrument; and (4)

integration of all geophysical site characterization data at the GRFL as an extensive case study for a well characterized shallow aquifer site.

Our scientists organized a simple field experiment at Hanscom AFB in order to test field equipment that was to be used in a field experiment at Dover AFB. As part of the Hanscom experiment, they conducted a seismic refraction survey near to a contaminated site on Hanscom Air Field. Initial data analysis was meant to help determine field geometry and data acquisition parameters for another field experiment at Dover AFB. Further work will involve determination of bedrock profile map under seismic acquisition line at the Hanscom site. Our researchers organized and help conduct a field experiment at Dover AFB, Dover DE. We conducted a seismic refraction survey of the Groundwater Remediation Field Laboratory site. The primary goals were to map --if possible-- the aquitard boundary (the confining clay unit for the perched aquifer at the site) and determine general seismic velocity structure of the shallow subsurface to complement seismic reflection work carried out in 1995. Initial analysis of the data has been directed toward the second of these two goals.

4. USE OF LATTICE-GAS CELLULAR AUTOMATA METHODS

Cellular automata form a subclass of artificial neural networks which can be described as lattices of individual finite state automata updated in discrete time steps, with uniform structure and polynomial connectivity. The state of each lattice site at a given time step is defined in a deterministic or probabilistic way by a given neighborhood of lattice sites at a previous time step.

Special cases of cellular automata are capable of describing complex collective behavior. The simulation of fluid dynamics is an example which proves cellular automata are complementary and powerful tools to model phenomena that would normally be the exclusive domain of partial differential equations.

This class was named lattice-gas cellular automata and has not only become a 'toy model' for the exploration of the microscopic basis of hydrodynamics, but also tools for the numerical study of complex problems in fluid mechanics.

While the lattice gas may, in principle, be used for nearly any problem in hydrodynamic simulation, many of the most successful applications have involved either a complex fluid, a complex geometry, or both.

Lattice-gas cellular automata methods (LGCA) are an attempt to use the theory of discrete molecular dynamics to model physical processes such as fluid flow through porous media and wave propagation in heterogeneous media. Solving these problems via separate partial differential equations keeps the parameterizations separate. Using the single LGCA theory to describe both of these parameters (e.g., elastic wave velocities) to the desired physical properties (e.g., hydraulic conductivity). This type of mapping is most important in the environmental area where it is often necessary to determine the characteristics of the ground water hydrology from non-invasive geophysical measurements made at the ground surface.

5. SURFACE WAVE REGIONALIZATION

Our scientists and researchers have attempted to improve the existing global grids of Rayleigh and Love surface wave group velocities. The grid is used to estimate surface wave arrival times for use in seismic surface wave association codes; in other words, for determining which of many recorded surface waves is associated with a particular seismic event. In the original grid, the emphasis was on surface wave energy in the 17-23 second band used for measuring the surface wave magnitude, M_s which is used for yield estimation and as a discriminant when compared with the body wave magnitude, m_b . Additionally, this grid contained 16 Rayleigh wave regions of which 9 were oceans or shallow seas; South America, Australia, and Antarctica were considered the same group velocity region. The drawback with this model, excluding the 17-23 second range, the velocities and more important the shape of these regionalized dispersion curves from 10-50 seconds did not agree with observations and were of no use for phase matched filtering, a common technique for finding and extracting surface wave signals from noise.

As a starting point, we requested and received from the Air Force Technical Applications Center (AFTAC) their regional surface wave dispersion subroutines and data base, so that we could include new global crustal structure information in it. The global model we initially used was Mooney's 1994 Global Crustal Model. This model is described on a 5x5 degree grid and gives the thickness of ice, water, soft sediments, hard sediments, upper crust, and lower crust. The initial version we received additionally had an eight layer P-velocity model of the regions. We added shear velocity and density to Mooney's model. However, we later received Mooney, Laske and Masters (1995) Global Crustal Models with gridded global crustal structure. This model was an improvement over the 1994 model in that there are now 89 distinct structure types versus the previous 52 types

and shear velocities and densities have added the 8 layers making up each of the 89 models. Our researchers then incorporated the models into AFTAC's codes for surface wave ray or path tracing. We completed the calculation of the fundamental Rayleigh and Love phase and group velocities for the 1995 Global Crustal Models including the crust mantle interface (Moho) at a 5x5 degree grid or each crust type at specified periods using our dispersion code. The periods of AFTAC's observed velocities were overlapped by starting at 38 seconds and going down to 7 seconds. Global contour maps of Rayleigh and Love group velocities at periods of 20 and 10 seconds were plotted. Our original purpose for using crustal structures was for calculating regional dispersion, i.e., for periods less than 20 seconds.

Using over 4000 source-receiver pairs, Stevens (1996) was able to perform a tomographic determination of Rayleigh group velocities from 300 to 12.5 seconds and refine the Okal dispersion values in the shield and sub-divide the mountain region into two. In addition, he obtained vastly improved group velocities for the trench and subduction region for a total of 8 distinct dispersion regions. This 10x10 degree model is implemented at the Prototype International Data Center. Again using Global Tectonic Regionalization (GTR1) as a guide, we interpolated the Stevens-Okal regionalization into a 5x5 degree global model. Arbitrarily reducing the grid size for tomographic determined velocities can create problems, but in this case the inversion path lengths across the age boundaries for the oceanic determined dispersion curves of Yu & Mitchell (1979) and Mitchell & Yu (1980) were based on smooth boundaries, and so in the oceans the smaller the grid the closer to the actual path lengths used in the original inversions. This was also added to our composite model.

We received test data from AFTAC which was to be used compare our model's to five other current models. The test data was for five events; three events are in the Nevada Test Site (NTS), one in China, and one in Kazakh. Each data set had the location of the stations recording the events and the observed travel time and great circle group velocities to the stations. We were able to read the test data and calculate a group travel time between the events and recording stations in the test data file for each of the six proposed regionalizations and their regional group velocity dispersions curves. Statistics were determined for all five events such as the number of stations, the distribution of range and azimuthal, and the average period for which a group arrival time was determined. For the five events tested, the composite model was the best in reduction of the average difference over the stations and it's standard deviation.

6. COLLECTION AND INTERPRETATION OF SEISMIC DATA TO DETERMINE CRUSTAL STRUCTURE

In an effort to determine the crustal and upper mantle structure in a wide region around the Pinedale Seismic Array. Our researchers helped install a large-aperture seismic array surrounding the existing Pinedale Seismic Array to collect data for the purpose of characterizing the region geophysically. The array operated for 2.5 months starting near the end of July 1995 and consisted of five broadband stations each located approximately 80-100 km from the Pinedale Seismic Array. Each station contains broadband and/or long-period sensors installed in a shelter mounted to a concrete pad, a refraction technology data acquisition system, a 530-Mbyte hard disk, and a GPS clock for accurate timing. Power at each site came from solar panels that we installed or by direct line power. The large-aperture array was designed to provide data for three separate studies:

- measure teleseismic surface wave propagation (phase and group velocity, attenuation) across the region,
- receiver function analysis of teleseismic P-waves at individual array stations,
- modeling of surface and body waves from regional earthquakes.

Additionally, we recorded and are interpreting a pair of large chemical explosions detonated in the western United States in August-September 1995. These two Ammonium Nitrate Fuel Oil (ANFO) explosions were detonated within a week of each other near the Gas Hills, Wyoming for the purpose of investigating the structure of the crust and upper mantle. These explosions were monitored at varying seismic sites along the Green River Seismic Profile, including one site that was common to both explosions. The data were collected and processed at the common site for both explosions. These explosions were recorded by the Pinedale Large-Aperture Array installed around the existing seismic array. The second source of measurements, used to described the refraction profile, came from 47 individual seismic stations that were installed and deployed for a period up to three days. The stations were uniformly spaced by 3.2 km starting from Big Sandy, Wyoming, west to the border of Wyoming and Idaho. The data from the 47 stations were displayed for two chemical explosions detonated near the Gas Hills, Wyoming. The profile data collected is essential to determine the crustal structure beneath the Wind River Mountains. Included in the 47 stations were three different types of station configurations. The data was recorded on three different instruments. These recorders are Terra Technology Recorders, Refraction Technology Recorders, and PDAS Recorders, each having a different format for storing data. Therefore, the data had to be processed in a different manner to produce a uniform data set. This involves numerous

quality checks of the data before and after processing. The processing of the seismic data in a similar fashion as the other station configurations allowed us to combine the data and display it as a single refraction profile.

The refraction data set, including the two blasts recorded at the 47 seismic stations, was downloaded onto an Exabyte tape which is now available to other scientists who want to use the Wyoming refraction data set. More analysis was conducted on the similarity of the two ANFO explosions used in this experiment. The data for both explosions were collected and processed at a common site. Spectral amplitude ratios were examined for different seismic phases including a pre-event noise sample.

7. REFERENCES

- Goodman, D., Ground-penetrating radar simulation in engineering and archaeology, Geophysics, **59**, 224-272, 1994.
- Harkrider, D.G., J.L. Stevens, and C.B. Archambeau, Theoretical Rayleigh and Love waves from an explosion in prestressed source regions, Seismol. Soc. Am. Bull., **84**, 1410-1442, 1994.
- Kennett, B.L.N. and N.J. Kerry, Seismic waves in a stratified half space, Geophys. J. R. Astr. Soc., **57**, 557-583, 1979.
- Roberts, R., Finite-difference time-domain forward modeling of GPR data, Proc. Fifth Intl. Conf. on GPR, **1**, 185-203, 1994.
- Stevens, J.L., N. Rimer, J.R. Murphy, T.G. Barker, E. Bailey, E.J. Halda, W.J. Proffer, S.H. Rodgers, and B. Shkoller, Simulation of seismic signals from partially coupled nuclear explosions in spherical and ellipsoidal cavities, S-CUBED Final Report, (SSS-FR-91-12735), Contract Number 90-N3039000-000, La Jolla, California, 1991.
- Ursin, B., Review of elastic and electromagnetic wave propagation in horizontally layered media, Geophysics, **48**, 1063-1081, 1983.

APPENDIX

PRELIMINARY GEOPHYSICAL CHARACTERIZATION OF GROUNDWATER
REMEDATION FIELD LABORATORY, DOVER AIR FORCE BASE, DELAWARE

Kadinsky-Cade, Katherine
Phillips Laboratory Geophysics Directorate, Earth Sciences Division

Cardimona, Steven
Institute for Scientific Research, Boston College

ABSTRACT:

During a two week period in June 1995, the Earth Sciences Division of Phillips Laboratory performed an integrated geophysical survey at a site that will be used for a series of groundwater remediation studies. This survey was carried out with field support by the Colorado School of Mines, Kansas Geological Survey and Elohi Geophysics, Inc. The groundwater remediation work will be part of the Air Force's contribution to the Strategic Environmental Research and Development Program (SERDP). The geophysical survey helps provide site characterization information that can aid in the siting of test cells for future remediation experiments. An important focus of this work is to compare coincident surface seismic and ground penetrating radar (GPR) measurements. The site consists of a 10 to 15 meter thick sandy aquifer overlying a clay aquitard. The site is heterogeneous, with clay lenses and gravel present within the aquifer. A variety of seismic sources were tested at the site, including a Betsy firing rod shooting 12 gauge blanks, a sledgehammer, a slidehammer and a portable vibrator. We used 100 Hz geophones throughout the seismic survey. Recording was done in a common depth point reflection profiling configuration. A downhole seismic survey was performed by lowering a hydrophone into a monitoring well at the site. Continuously recorded GPR profiles at 300 and 500 MHz were collected to complement a set of 100 and 200 MHz measurements obtained by the University of Delaware at the same site. The surface data are being supplemented by cone penetrometer measurements (resistivity and uphole seismic) performed by Applied Research Associates, Inc. We made terrain conductivity measurements to aid in the interpretation of the GPR data. Precise terrain elevation measurements are being used for static corrections. Data processing is currently in progress. It is commonly pointed out that the seismic and GPR techniques tend to be successful in mutually exclusive areas (GPR attenuated by high conductivity clay media and seismic plagued by poor coupling in sandy soils). At this site both techniques seem to work reasonably well, and variations in the imaging capability of each technique across the site will be the subject of an interesting research study.

MODELING GROUND PENETRATING RADAR TRANSMISSION PROPERTIES IN CONDUCTIVE AND DISPERSIVE MEDIA

Steve Cardimona, Institute for Scientific Research, Boston College
Katharine Kadinsky-Cade, Air Force Phillips Lab, Earth Sciences
Both at: PL/GPE, 29 Randolph Road, Hanscom AFB, MA, 01731-3010

Maxwell's equations describing the propagation of electromagnetic plane waves in dielectric media with conductive losses are solved exactly by finding solutions to an eigenvalue problem for electric and magnetic field intensities in media with depth-dependent properties. For a given frequency and horizontal wavenumber (propagation angle), the local eigenvalues of the differential system define the permissible vertical wavenumbers within the medium and include the attenuation due to non-zero conductivity. The matrix of eigenvectors and its inverse are used to match the boundary conditions, i.e., the continuity of the tangential components of the electric and magnetic field intensities across the interfaces between layers. Using the local eigenvalues and eigenvectors of the system we compute a fundamental matrix for the layered medium, from which we obtain the reflection and transmission properties of the complete subsurface structure. The time-domain wavefield solution can then be built up through a summation (slow-Fourier transform) over the contributions at all horizontal wavenumbers of interest and an integration (a fast Fourier transform) over the frequencies in the source wavelet. The reflection coefficient can be integrated, for example, to yield the backscattered wavefield which allows us to synthesize surface collected ground penetrating radar data. We use this method to explore the transmission properties of attenuative and dispersive layered media by varying the parameters of conductivity, magnetic permeability, electric permittivity, peak probing frequency, and angle of incidence. Computation of the transmissivity as a function of depth for a variety of parameters is accomplished rapidly since the integration over wavenumber and frequency to get the time-domain wavefield is not performed. In this way we can easily investigate the sensitivity of the ground penetrating radar signal to variations in realistic, near-surface medium properties.

**Isotropic and Deviatoric Moment Inversion of Regional Surface Waves
from Nevada Test Site Explosions:
Implications for Yield Estimation and Seismic Discrimination**

Bradley B. Woods and David. G. Harkrider
Seismological Laboratory, CalTech, Pasadena, CA

AFOSR F49620-93-1-0221

Institute of Scientific Research, Boston College, Boston, MA

AFPL F19628-95-C-0116

ABSTRACT:

Seismic moments of Nevada Test Site (NTS) explosions were determined from regional surface wave spectra. Two methods were used. In one the moment is solved for assuming only an explosive source, or average scalar moment; in the other a joint inversion for an isotropic (explosive) source plus a constrained double couple moment component representing tectonic strain release (TSR). Although the general moment tensor solution to this joint inversion problem is non-unique, if some assumptions are made concerning the non-isotropic moment components, then the remaining source parameters can be solved by a linear least-squares inversion scheme. We examined the errors in determining the isotropic moment component (M_I) by this latter method of constrained linear inversion solutions in a canonical study using a theoretical network of long-period (6-60 sec.) surface wave data. The network azimuthal coverage was chosen to represent that of a long-period North American super-network of 55 stations used for the actual NTS events. We compared these errors in moment estimate to those obtained from surface wave magnitude (M_S) and spectral scalar moment (M_0) measurements for the same surface wave observations. For a ratio of $M_{(expl)}/M_{(eq)}$ less than 1.0 we found that the inverted M_I solution is a much better estimate of the actual isotropic moment than either M_S or M_0 , and the standard deviation in this estimate is substantially less than that using the other two methods for the great majority of isotropic source + double couple sources. Even when the inversion constraints are off in dip and rake each by 30° , the mis-estimate of the isotropic moment is less than 35 percent of the actual value. In the case of a vertical strike-slip fault, the inverted isotropic moment solution which assumes this fault orientation is exact to three figures, whereas M_S and M_0 under-estimate the moment by 45 percent and 32 percent, respectively because of uneven azimuthal coverage.

This moment tensor inversion method was applied to determine the isotropic source for 111 NTS underground explosions using vertical and tangential component surface wave data from this regional network. We also calculated M_S and M_0 for these same events and compared the results. Isotropic source errors were smallest using the spectral domain inversion method. However, this spectral domain method cannot attain as low a magnitude threshold as the time domain moment or M_S method. The extensive moment data set analyzed were combined with larger yield explosions from prior moment studies to create a comprehensive data set with which to obtain conclusive, well-constrained long-period explosion source scaling relationships at the separate NTS sub-sites.

Regressing on the results presented here and the results of others for larger events with published yields, we obtained a M_I versus yield relation with which we were to estimate the surface wave inferred yields of the 111 NTS events before and after correcting each event for its sub-site bias.

Preliminary Report on Surface Wave Regionalization

D. G. Harkrider and J. L. Stevens

Institute of Scientific Research, Boston College, Boston, MA

AFPL F19628-95-C-0116

SCUBED, Division of Maxwell Industries, La Jolla, CA

AFTAC F19628-95-C-0110

Summary

In the late 1960's, Kimbal and Kovacs of GEOTECH, developed a 1x1 degree global grid of Rayleigh and Love surface wave group velocities. The grid was used to estimate surface wave arrival times for use in seismic surface wave association codes; in other words, for determining which of many recorded surface waves is associated with a particular seismic event. The emphasis was on surface wave energy in the 17-23 second period band used for measuring the surface wave magnitude, M_s , which is used for yield estimation and as a discriminant when compared with the body wave magnitude, m_b . There were 16 Rayleigh wave regions of which 9 were oceans or shallow seas. South America, Australia and Antarctica were considered the same group velocity region. Excluding the 17-23 second period range, the velocities and more important the shape of these regionalized dispersion curves from 10-50 seconds did not agree with observations and were of no use for phase matched filtering, a common technique for finding and extracting surface wave signals from noise.

In 1977, Okal introduced a 15x15 degree global grid for long period Rayleigh waves and in 1989 using the 5x5 degree global tectonic regionalization (GTR1) of Jordan, 1981, as a guide, Okal&Talandier, 1989, presented a 10x10 degree grid of Rayleigh group velocities. They used the seven basic regions of Okal 1977 (four oceanic regions, shield, trench and mountain) with velocities in the period range from 300 to 35 seconds. The ocean velocities were from Yu&Mitchell, 1977, and Mitchell&Yu, 1980, and the regionalization was based on ocean ages. Mitchell and Yu also determined separate SV and SH velocity profiles to approximate the anisotropy of the oceanic lithosphere and low velocity zone. Shield, mountain, trench and subduction zone velocities were from Nakanishi, 1981 and Hwang&Mitchell, 1987. Since 1989, Okal and students have extended the velocities down to 17 second.

Jordan's model GTR1 has 6 regions with 3 ocean regions based on age and was presented mainly as a geographic framework in order to test new tectonic models or velocity structures as more observations and dispersion values become available. The regional dispersion was phase velocities from 20 to 120 seconds based on representative curves from Brune&Dorman, Landisman et al. and the Knopoff UCLA group. Rosa (1986) performed a numerical differentiation of the scanned phase velocities to obtain group velocities. Since our interest and test data was mostly near the end-point of 20 seconds (the least reliable of the differenced curves), we were not able to use the majority of our test data source-receiver pairs.

Using over 4000 source-receiver pairs, Stevens, 1996, was able to perform a tomographic determination of Rayleigh group velocities from 300 to 12.5 seconds and refine the Okal dispersion values in the shield and sub-divide the mountain region into two. In addition, he obtained vastly improved group velocities for the trench and subduction region for a total of 8 distinct dispersion regions. This 10x10 degree model is implemented at the Prototype International Data Center. Again using GTR1 as a guide, we interpolated the Stevens-Okal regionalization into a 5x5 degree global

model. Arbitrarily reducing the grid size for tomographic determined velocities can create problems but in this case the inversion path lengths across the age boundaries for the oceanic determined dispersion curves of Yu&Mitchell (1979) and Mitchell&Yu (1980) were based on smooth boundaries and so in the oceans the smaller the grid the closer to the actual path lengths used in the original inversions.

For the purpose of obtaining a more detailed regionalization for use with regional dispersion and magnitudes, we decided to use Mooney's global crustal structure model for calculating shorter period Rayleigh and Love wave dispersion. Originally Mooney had a 5x5 degree global grid of 52 crustal P-velocity structures down to the crust mantle interface(Moho). The crust was divided into 5-7 layers. In 1995, Mooney, Laske&Masters included S-velocity and density in the crustal models. The result was 89 seismic structures. The 5-6 layer P-velocities and interface depths were obtained from refraction and reflection profiles. The structures included Moho velocities and densities. There can be a water or ice layer at the surface. S-velocities and densities were obtained from surface wave inversions, refraction profiles, observed relations between Poisson ratio, density, and depth and when all else failed: intuition. Their latest model was 1995 but a "final corrected model" is due the summer of 1996. Rayleigh and Love waves were calculated for periods between 7 and 50 secs. Because the structures only went to Moho depths, the oceanic group velocities are featureless over the oceans at periods greater than 17 secs. This resulted from the common observation that the depth of influence in kms. on the fundamental Rayleigh wave is approximately twice the period in secs. and that all the ocean structures in this model were identical below a depth of 20 kms. Because of this it was suggested that at periods near 20 secs., the Mooney et al. models be used for continents and regions of thick crust with a 5x5 degree interpolation of the ocean models of Okal and the trenches and subduction regions of Stevens. This was accomplished again using GTR1 as guide and is our composite grid of 94 dispersion regions.

The 6 models: (1)Kimbali-Kovacs, (2)Okal, (3)Mooney, (4)Stevens, (5) Stevens 5x5, and (6)Mooney-Stevens were tested with the group arrival times of the narrow band filtered period of maximum energy in the range of 17-23 secs from 3 test sites: NTS, Lop Nor and Kazakh. The number of recording stations ranged from 23 to 41. As one might hope, the percentage in error of the arrival times was reduced by each addition of the new models. Even the Mooney model with its poor oceanic dispersion was better than the Okal model, which was a major improvement over the Kimbali-Kovacs model. The reduction in arrival time error is essentially in the order of the listed models except that the Mooney model was better for the Chinese and Kazakh test-sites. The arrival time error for the Mooney-Stevens model was slightly larger than both Steven's models but the standard deviation of this error over the recording stations for all events was much smaller for this composite model. This indicates the possibility of a base line error in this model rather than in the regionalization it self. This may be true of all the models since the station averaged arrival time was slower than observed for all events.

The Western Wyoming Seismic Refraction Profile

S H Koester (Boston College, Institute for Scientific Research,
PL/GPE, 29 Randolph Road, Hanscom AFB, MA 01731;
617-377-2652; email: koester@doc.plh.af.mil)

J J Cipar (Phillips Laboratory, Earth Sciences Division, Hanscom Air
Force Base, MA 01731; 617-377-3767)

J R Steeves (Analytical Systems Engineering Corporation, Burlington,
MA 01803)

J A Cipar (R. J. Grey JHS, Acton, MA 01720)

F Lorenz and P Lorenz (Geoforschungszentrum, Potsdam, Germany)

J Granillo (University of Texas at El Paso, El Paso, TX 79968)

E M O'Pray (Analytical Systems Engineering Corporation, Burlington,
MA 01803)

T Anderson (University of Connecticut, Storrs, CT 06269)

A 47-station refraction profile was deployed in western Wyoming to monitor the chemical explosions from Project Deep Probe in August, 1995. The profile extended from the edge of the Wind River Mountains at Big Sandy, Wyoming, west to the border of Wyoming and Idaho. The first data set was collected on August 8th and 9th by the 14 stations closest to Idaho. The second data set was collected on August 16th and 17th by the remaining 33 stations. Each station was spaced approximately 3.2 km from each other. The data was recorded by short period sensors that were digitized and stored by either a Refraction Technology recorder with a GPS clock, a Terra Technology recorder with WVB radio timing, or a PDAS recorder with a GPS clock. All data were digitized at 100 samples/sec on three components during both periods of recording with the exception of the Terra Technology recorders which were digitized at 100 samples/sec on the vertical component.

We plan to use the Deep Probe explosion east of Riverton, Wyoming, recorded by our profile to study the crustal structure beneath the Wind River Mountains in south-western Wyoming as well as the Wyoming and Salt River Ranges near Idaho. The Deep Probe explosions in Canada and the US will be used to explore the deep structure of western North America.

The Wyoming Large-Aperture Seismic Array

John Cipar (Earth Sciences Division, Phillips Laboratory, Hanscom AFB, MA 01731; 617-377-3767; e-mail: cipar@doc.plh.af.mil)
Stephan Koester (Boston College, Institute for Scientific Research; 617-377-2652; e-mail: koester@doc.plh.af.mil)
James Steeves, Eileen O'Pray (Analytical Systems Engineering Corporation, Burlington, MA 01803)
Thomas Anderson (University of Connecticut, Storrs, CT);
James Cipar (R J. Grey JHS, Acton, MA)

A five station seismic array has been installed in southwestern Wyoming since late July, 1995. The array is located in the Green River basin, west of the Wind River Mountains. The five stations are arranged in the form of a cross with the central station near Big Piney, Wyoming. Each outlying station is located about 50 km from the central site. Broadband and/or long-period sensors are installed at each station on a concrete pad surrounded by an insulated, wooden enclosure. Data are recorded on Refraction Technology data acquisition systems equipped with 530-Mbyte disks and GPS clocks. For the first two weeks of recording, during the period of the - Canadian/US Deep Probe experiment, data were recorded continuously at 40 samples/sec. Presently the array is recording continuously at 20 sps (10 sps at 2 sites). Power is supplied either from solar panels or by line power at certain sites. Current plans are to operate the array into early October, 1995.

We plan to use the data from this array to study:

- regional wave propagation in the central Rocky Mountains
- spatial variability of earthquake/explosion discriminants
- crustal structure beneath the array

Examples of data from the array such as the August, 1995 Chinese nuclear test, regional earthquakes, and Deep Probe and mining explosions will be displayed.

HIGH-RESOLUTION SEISMIC REFLECTION SURVEY AT DOVER AFB: A COMPARISON OF THREE SEISMIC SOURCES

Steve Cardimona

Boston College, PL/GPE, 29 Randolph Road, Hanscom AFB, MA 01731

Katharine Kadinsky-Cade

Earth Sciences Division, US Air Force Phillips Lab, 29 Randolph Road, Hanscom AFB, MA 01731

Richard Miller

Kansas Geological Survey, 1930 Constant Ave., Lawrence, KS 66047

Jay J. Pulli and Walter Turpening

Elohi Geophysics, Inc., 11606 Brook Meadows, Meadows, TX 77477

ABSTRACT

In June of 1995, the Earth Sciences Division of the Air Force Phillips Lab, with survey equipment from the University of Delaware and assisted by the Kansas Geological Survey and Elohi Geophysics, conducted a geophysical site characterization of the SERDP-funded Groundwater Remediation Field Lab (GRFL) located at Dover AFB, Delaware and administered by Applied Research Associates for USAF Armstrong Lab. Seismic data were collected in order to 1) compare the results using three different compressional sources and 2) cover the field site well enough to characterize the seismic response of the shallow subsurface. This paper will focus primarily on the first of these two goals.

Seismic data were collected along three north-south profiles set 10 meters apart, each profile with a different compressional source: a 5.5kg sledgehammer, a 12-gauge firing rod from Betsy Seisgun Inc. shooting 150 grain blanks, and a portable piezoelectrically driven vibrator, developed by Elohi Geophysics, operating with a 90Hz-450Hz sweep. An east-west cross line was collected using the sledgehammer source in order to tie the three profiles together. A laser theodolite provided station location and elevation control. The primary targets were the water table (that had been marked on maps at a depth of about 3 meters) and a sand-clay interface at about 15 meters depth. We collected 24-channel CMP data using a half meter spacing of both source and 100Hz geophones. An end-on spread geometry was used, with a 1 meter offset between source and nearest geophone. Field QC after initial walkaway noise testing with each source did not show any one source to be outstanding

We have associated the strongest reflection event with the sand-clay interface interpreted as the top of the aquitard. A practical early result of the seismic survey showed the water table to be at over 8 meters. Seismic data comparison in this study is based on spectral content, total energy and signal-to-noise ratios, as well as a discussion of coherency of the primary reflection event at the water table. The problem with the water table being deeper than expected is that the water table reflection may interfere with the primary seismic target, the sand-clay interface. With a wavelength of about 4 meters at 100 Hz, interpretation of the data must take into account the possible interference of the two reflections in the seismic images.

With a surface velocity of 400m/sec, the first Fresnel zone for 100Hz signals at 15 meters depth is about 5.5 meters under each seismic line, therefore overlapping between profiles. Thus, despite the separation of the three lines, they are sampling similar regions of the target area. Nevertheless, initial inspection of the seismic shot gather data showed that they are characterized by rapid variations in amplitude and phase across short distances.

Both the firing rod and the vibratory source gave an initial look at the near surface during data acquisition via the use of augers necessary for deployment of these sources. The site had rapid lateral

changes in the upper meter. Clays and gravel stringers with lateral variability on the order of a half meter were the norm. Cone penetrometer data suggest that this heterogeneity extends deeper as well. Our comparison of the data acquired using the different sources is with the caveat that there is an extreme variability in the near surface.

BACKGROUND AND SITE CHARACTERISTICS

Dover Air Force Base, Dover, Delaware, is the site of the Groundwater Remediation Field Laboratory (GRFL), a national test site administered by the Air Force Armstrong Laboratory (AL) with funds from the Strategic Environmental Research and Development Program (SERDP), a partnership between DOD, DOE and EPA. In 1995, AL and their contractor Applied Research Associates (ARA) had laid the groundwork for the GRFL which will provide an infrastructure in which a number of test cells will be able to operate simultaneously. The GRFL is intended to offer a place where researchers may test remediation technologies that address a variety of LNAPL and DNAPL targets in the subsurface. Geophysical characterization of the site was begun by The Air Force Phillips Lab (PL) and the University of Delaware in March-June 1995, collecting ground penetrating radar (GPR) at multiple source frequencies, shallow high resolution seismic reflection data and terrain conductivity. ARA continued through the end of the summer collecting soil samples, cone penetrometer data, and more GPR.

The test site consists of an unconfined aquifer extending to a depth of 15-18 meters, with a clay aquitard below. The water table is at about 8.5 meters. The surface of the site is a 3.5 acre grassy field that has a gentle dip to the east, with only minor topographic undulations of less than .5 meter. Initial goals of the seismic survey were to characterize the seismic response of the site and to collect reflection profile data coincident with specific lines of the more densely spaced GPR data. Previous work in coastal plain sedimentary environments (Miller, et al., 1986) suggested that most compressional source types should be adequate for the seismic reflection data acquisition, and our initial plan was to choose the best source for making a comparison between the seismic and the radar data. After preliminary source parameter testing in April 1995, we determined that a seismic source comparison at this site might be worthwhile. The seismic reflection data were acquired in June 1995.

DATA ACQUISITION AND FIELD QC

All seismic data were collected with a 24-channel Geometrics StrataView recorder. The geophones were single component, 100Hz Mark Products L40A instruments with 14cm spikes. Standard CDP cable and roll switch were used to collect the reflection data. Figure 1 shows the field site geometry and layout of CMP lines. We collected 24-channel CMP data using a half meter spacing of both source and geophones. An end-on spread geometry was used, with a 1 meter offset between source and nearest receiver. Three compressional sources were tested and used for CMP profiling: a 5.5kg sledgehammer, a Betsy Seisgun, Inc. 12-gauge firing rod, and the Earth Reaction Seismic Source (ERSS) portable vibrator from Elohi Geophysics.

In one day we collected 332 source points of sledgehammer data along a line through the central portion of the field. At each source point we stacked eight hits of the hammer, for a total of over 2600 blows. Figure 2 shows a representative shot gather from the sledgehammer CMP collection. The air wave and a slow direct wave (~250m/sec) overlap with the ground roll at near offsets. A shallow refractor at ~475m/sec is strong in the far offset traces. Although source repeatability was not optimum due to four different hammer operators and the length of day in the field, stacking eight blows per shot point did a very good job of equalizing source wavelet and signal strength.

Ten meters to the east of the sledgehammer line we collected 187 shot points with a 12-gauge firing rod shooting 150 grain blank loads. Holes were drilled about one meter deep, and three different

packing techniques were tried: no packing (air-filled), water-filled and dirt-filled. There was not much difference noticeable in the shot data between water-filled holes and dirt-filled holes. The bulk of the CMP data were collected with dirt-filled holes for source coupling. Figure 3 shows a representative shot gather. Whereas the sledgehammer had a large ratio of ground roll to body wave energy, the firing rod's strongest arrival is the 475m/sec refraction event that on some records is even stronger than the air wave.

Ten meters to the west of the sledgehammer line we collected 228 source points of CMP data with the ERSS vibrator (Figure 4). The ERSS was operated with a linear sweep 90Hz to 450Hz three seconds long. Each source point was a stack of eight sweeps. Deployment of the ERSS is by hydraulic augering in ground anchors and hooking the source to them one at a time. The hydraulic auger also is used to remove anchors. The ERSS weighs about 90 pounds and the hook clamping system is set to generate 300 pounds of hold-down force. At test time, a pilot was not recorded with each sweep so uncorrelated data were recorded and cross correlation done with a synthetic sweep during processing. The FK-spectra of the vibrator records show low groundroll and airwave energy relative to that of body waves. The shot records (Figure 5), as with most all vibrator data, do not show clear refraction arrivals.

Planting the geophones was not difficult over all; however deployment of the ERSS and the Betsy Seisgun required penetrating deeper into subsurface. As evidenced by the auger work for each of these sources, the variability of the upper meter of the subsurface was extreme on a scale of a half meter (from one shot point to the next shot point). Clay stringers and gravel lenses were the norm across the entire field, and cone penetrometer data indicate this variability extends well below the upper half meter. The lateral variability makes it difficult to compare directly the stacked sections from each source relative to strength and continuity of common reflection events. Nevertheless, we will discuss these issues as well as make some observations regarding the resolution of reflectors in the data.

DATA PROCESSING AND INTERPRETATION

Each CMP data set for this comparison went through the following processing history:

- Bandpass filter (zero-phase Butterworth 80-300Hz with Hamming taper)
- F-K filter to remove airwave and groundroll
- First arrival mute (direct wave and shallow refraction)
- NMO correction (after constant velocity stacks to get best velocity functions)
- CMP stack
- Signal to noise enhancement with single-adjacent trace mixing
- Display with 50ms AGC

Figure 6 displays the three CMP profiles for comparison. The sledgehammer and vibrator lines are cut short to coincide with the length of the firing rod line. In the sledgehammer CMP profile (Figure 6a), there are three major reflection events at ~34-38ms, ~40-48ms and at ~25-28ms. In the south end of the line, the deeper reflections dominate, while at about CMP location 350 the shallower event becomes prominent. Both of the deeper events shallow somewhat from south to north as they approach the middle of the profile, and the shallower event has a similar dip.

The shallow refractor witnessed in the shot gather data at about 1m depth corresponds with what might be the bottom of a tilled zone for this field that at one time had been farmland. The ~36ms reflection event corresponds to a reflection off the water table at 8.1m. The ~44ms reflection event corresponds to the top of the clay confining layer at 14m depth. Data processing of all three seismic lines suggested that the near surface velocity increased toward the north. During data acquisition it was noted that the north end of the field was extremely different at the shallowest level. Geophones and survey markers were harder to plant due to much more compacted surface. The different nature of the shallowest layering might be due to the construction of the running track to the northeast of

the study area (Figure 1). This velocity change from south to north could explain the apparent shallowing of the reflection events that are more likely horizontal or even deepening (as limited cone penetrometer data suggests).

The firing rod CMP profile (Figure 6b) mirrors the sledgehammer line, with the 42-44ms reflection event dominating the record. The profile stops just about at the point where the shallower reflection event becomes prominent in the sledgehammer line. North of CMP location 245 the firing rod line shows this shallower event as well. The top-of-clay reflection is much more continuous across the profile, with better signal to noise evident than in the sledgehammer line. The water table reflection is just as discontinuous as in the sledgehammer profile. There is a suggestion in the firing rod profile of something deeper than the top-of-clay; however, it seems to track the prominent event above it, and thus is very likely a side lobe of the top-of-clay event.

With low groundroll and airwave, and little direct wave, the vibrator data offers the possibility for the shallowest imaging, although the first reflector is not seen until two-way time of ~25ms in the north portion of the profile (Figure 6c) as seen in the sledgehammer and firing rod profiles. The vibrator profile shows the water table reflection and the top-of-clay as with the other sources, however the water table reflection appears to be the stronger and more continuous of the two.

Figure 7 shows amplitude spectra for each stacked section using a 60 ms window, starting at 5ms two-way time for the signal. Comparing the average spectra after stack across each section, the vibrator data is the most broadband with a peak at 125Hz. The sledgehammer offers the next best frequency content, with a peak at 93Hz and with more usable information out to 200Hz than with the firing rod. The firing rod peaks at 85Hz, and rolls off a little more quickly at higher frequency than does that of the sledgehammer.

Presumably, the lower resolution in the impulsive data records result in a little more interference between the two primary reflection events. This may explain the difference between the impulsive sources that show the top-of-clay event as the most coherent and the vibrator profile that shows the water table as the most coherent event.

Amplitude spectra for single traces in each stacked section vary quite a bit. The three sources have similar maximum amplitudes on a trace-by trace basis (Figure 7). The sledgehammer was the strongest after summing eight blows, whereas the vibrator was the weakest. Average amplitude spectra across each section show the firing rod has a more consistent source spectrum, retaining its amplitude and leaving an average amplitude that is about twice the strength of the sledgehammer and four times the strength of the average for the vibrator. Using a time window deeper in the profiles (90ms-150ms) to get an estimate of noise characteristics, the average noise amplitude peaks at 187Hz for the sledgehammer and the firing rod, and at 202Hz for the vibrator. Using the peak values from the averaged spectra in Figure 7 to get the best signal and the worst noise, the signal to noise ratio (S/N) for the firing rod is the greatest at 4.3. The sledgehammer S/N=2.1 and the vibrator S/N=1.7 are close to each other and at less than half that of the firing rod.

CONCLUSIONS

Although this work constitutes a case study for an area where it is somewhat difficult to achieve superb seismic results, it also offers a good comparison of three near-surface seismic sources for CMP data collection and interpretation. In this paper we have focused specifically on the source comparison. Future reports will cover the more detailed interpretation of the data and the seismic characterization of the Dover AFB site.

With respect to resolution of reflection events in this study, the most broadband signal was obtained by the portable vibratory source. The vibrator offered continuity of reflection events similar to that

of the impulsive seismic sources, although events were difficult to interpret from shot gathers and no acquisition QC could be done directly on the recorder while collecting the uncorrelated data. The firing rod source offered by far the best signal to noise ratio and arguably the best lateral continuity of reflection events. The eight blows of the sledgehammer offered a source strength that was in between those of the firing rod and the vibrator, with a frequency content somewhat better than the firing rod. The sledgehammer was certainly the fastest source for collecting the most CMP data in a limited time, and was no more labor intensive than the other two sources that required the use of two-person augers. As each source excelled in one certain aspect, there was no single winner in our comparison. Specific survey and site limitations, and desired targets and results, must still dominate the choice of compressional source for near-surface exploration.

ACKNOWLEDGMENTS

We would like to thank Prof. John Madsen and the University of Delaware for loaning to us their seismic recorder and laser theodolite. Lt. Col. Robert Gauthier was an integral part of our field team. We also want to thank Mark Noll from ARA and the civil engineering department at Dover AFB for their support during our field work. Rex Morey of ARA supplied the site base map used in this paper. Any use of trade, product or firm names in this report is for descriptive purposes only and does not imply endorsement by the U.S. Government.

REFERENCES

- Miller, R.D., Pullan, S.E., Waldner, J.S., and Haeni, F.P., 1986, Field comparison of shallow seismic sources, *Geophysics*, v. 51, p. 2067-2092.

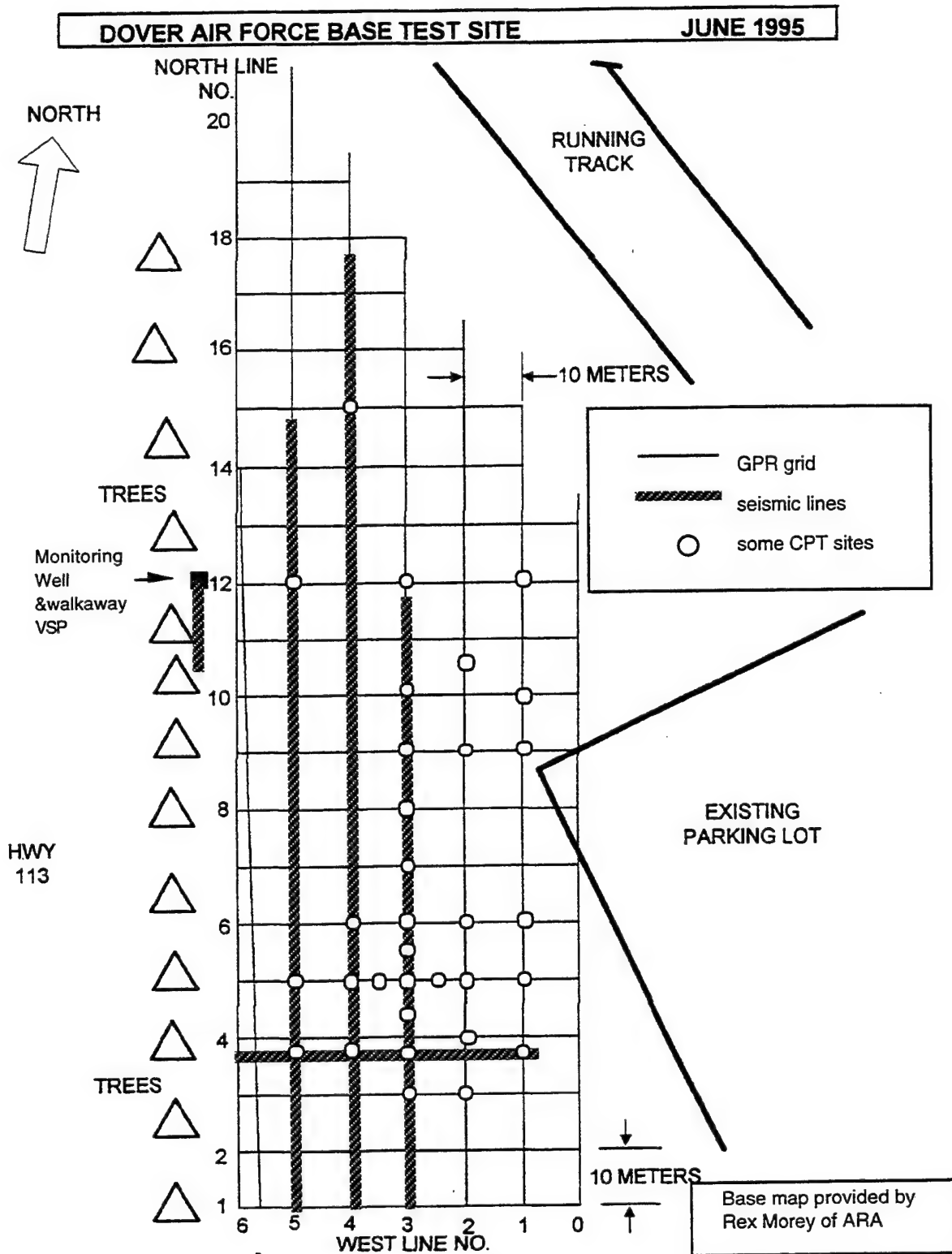


Figure 1. Geophysical survey layout at Dover AFB Groundwater Remediation Field Lab site

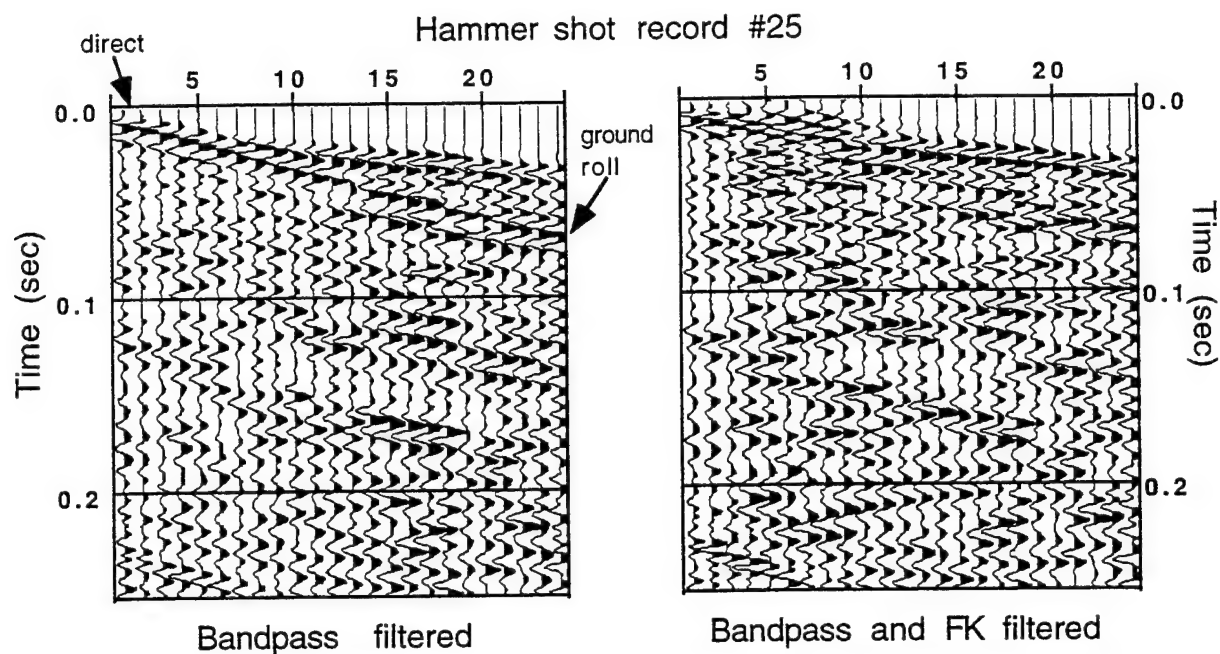


Figure 2. Example shot record for sledgehammer. Butterworth band-pass at 80-300Hz; FK-filter to remove energy at velocities less than 350m/sec

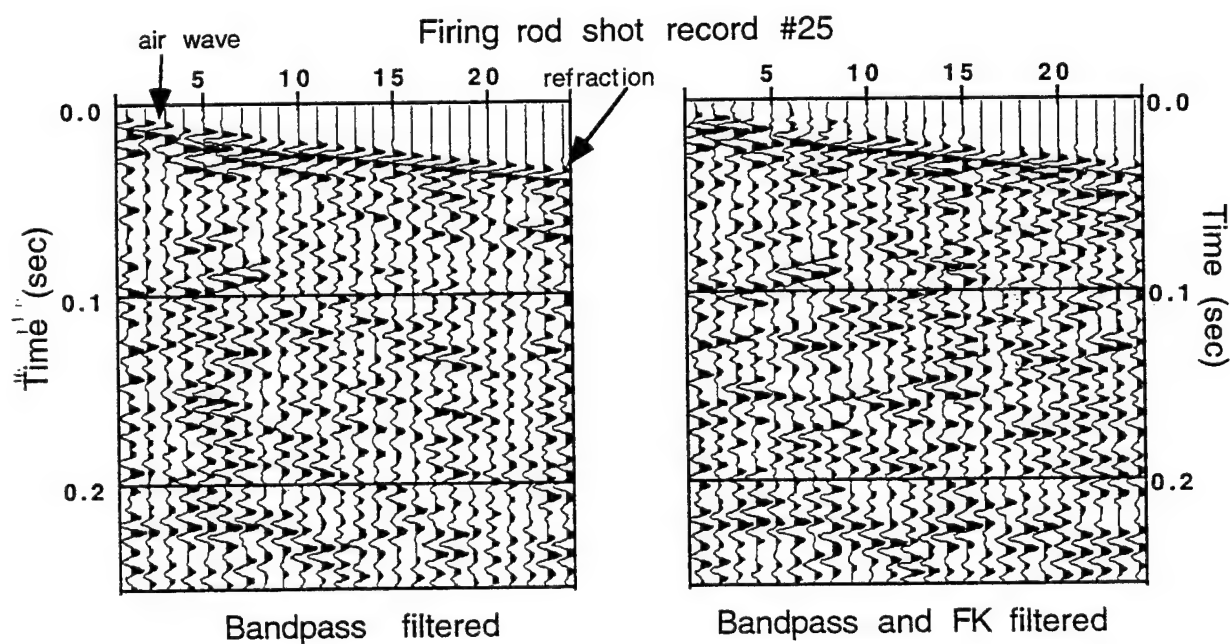


Figure 3. Example shot record for firing rod. Filter parameters as in Figure 2.



Figure 4. Deploying the Earth Reaction Seismic Source (ERSS)

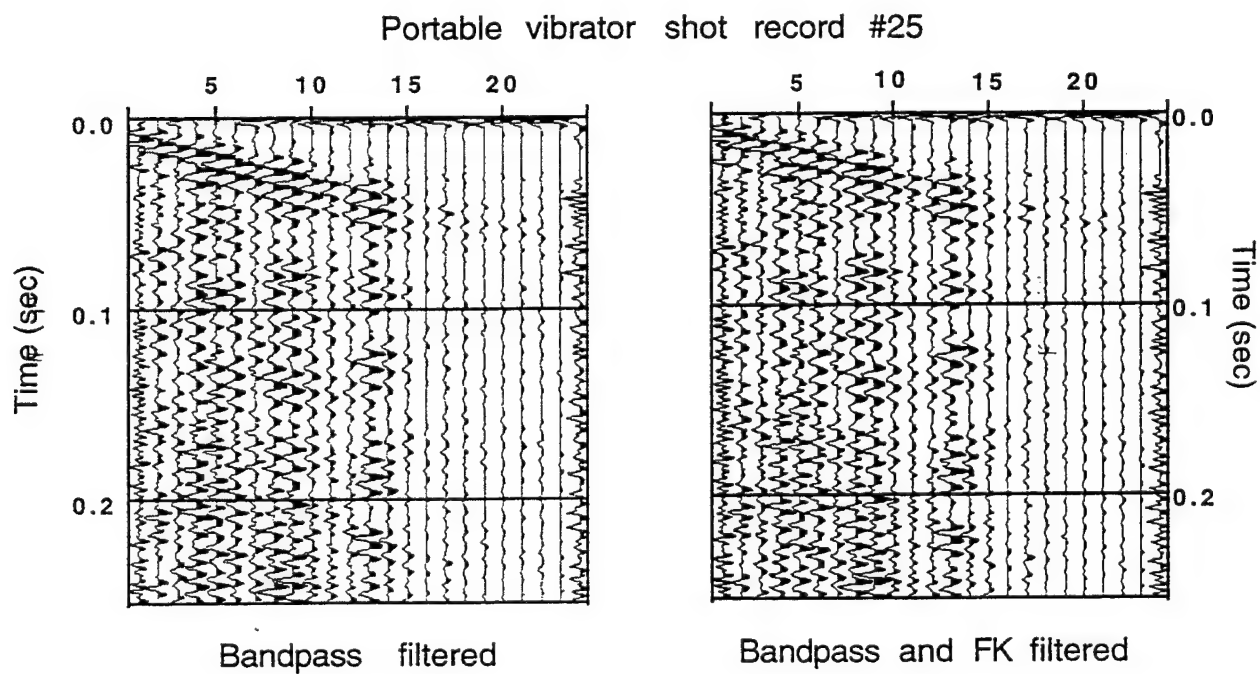


Figure 5. Example shot record for the portable vibrator. Filter parameters as in Figure 2

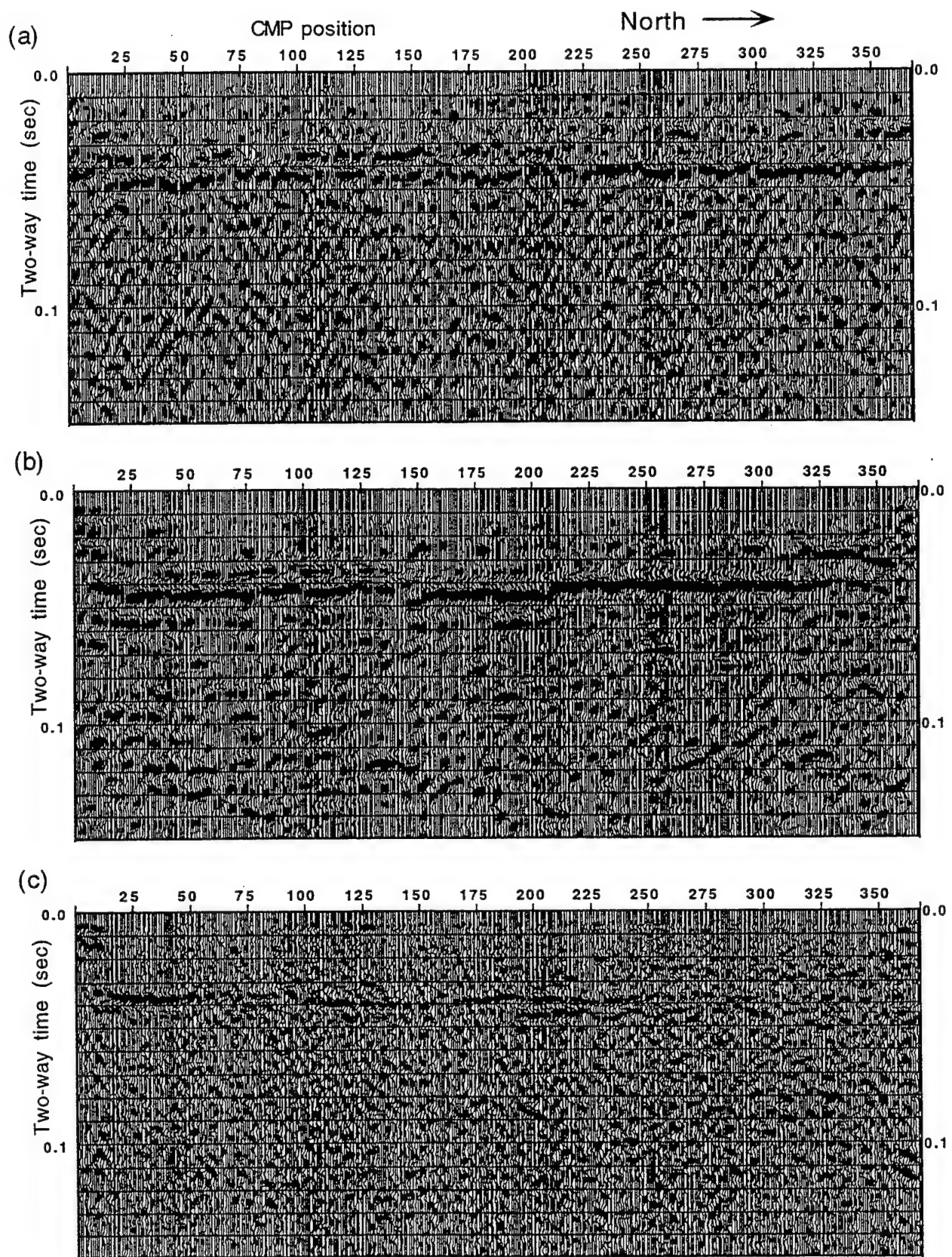


Figure 6. CMP profiles for (a) sledgehammer, (b) firing rod and (c) vibrator

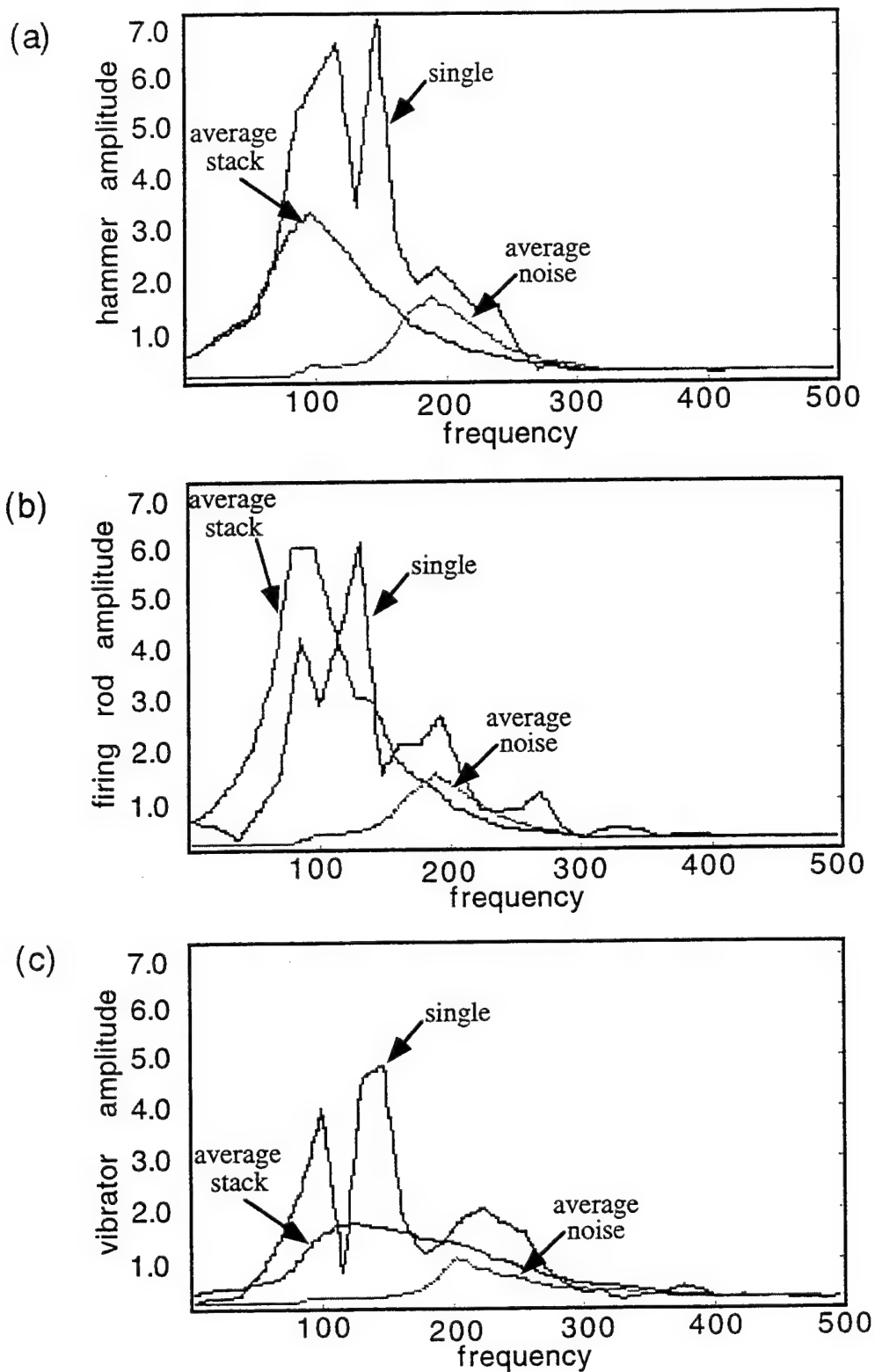


Figure 7. Amplitude spectra for (a) sledgehammer, (b) firing rod and (c) vibrator: "single" is single stacked trace; "average stack" is average over entire stacked section; "average noise" is average over entire stack section for noise window.

LATTICE GAS CELLULAR AUTOMATON MODELS FOR COMPLEX DYNAMICS

VICTOR OANCEA

**Institute for Scientific Research
Boston College**

M. NAFI TOKSOZ and CHEO K. LEE

**Earth Resources Laboratory
Massachusetts Institute of Technology**

CONTENTS

1. Introduction

2. Lattice-gas cellular automaton models of fluids

2. 1. Fluid dynamics

2. 1. 1. The continuum approach

2. 1. 2. The kinetic approach

2.2. The FHP models

2. 2. 1. The kinetic equations of lattice-gas models

2. 2. 2. The Boolean kinetic of lattice-gas models

2. 2. 3. High Reynolds number flows

2. 3. The Lattice Gas-Boltzmann method

2. 4. The Lattice Gas-Boltzmann / BGK method

2. 5. The 3D lattice-gas models

3. Numerical experiments

3.1. Poiseuille flow

3. 2. Flow past a barrier (von Kármán streets)

3. 3. Channel flow in expanded geometry

3. 4. Free boundaries flow

4. Applications

4.1. Flow through porous media

4. 1. 1. Immiscible multi-phase flow through porous media

4. 1. 2. Phase separation

4. 1. 3. Viscous fingering

4.2. Transport of particle suspensions

4.3. Free boundary flows

5. Conclusions

1. INTRODUCTION

The idea of cellular automata dates back to the work of von Neumann and Ulam in the 1940s (von Neumann 1966) who were looking for simple rules of spatial and temporal evolution to mimic collective, complex behavior of biological systems.

The first goal was to provide a theory for how an artificial life, capable of self-reproduction could be constructed, starting with the simplest rules possible. So appeared the idea of a collection of very simple finite-state machines (cellular automata) with, for simplicity, only binary values, the state of each depending only of the state of its immediate environment.

The natural space on which to put all this is a lattice with elementary finite-state machines placed at the vertices. The rules for updating this array of small machines (lattice cellular automata) can be done concurrently in one clock step, that is, in parallel.

In the last decades the interest from reproducing biological-like behavior automaton has shifted towards physics and computation: simulation of partial differential equations (Zuse 1970), time-reversible automata (Margolus 1984), simulation of quantum-mechanical phenomena (Feynman 1982), "statistical mechanics" of cellular automata (Wolfram 1983), cellular-automata as discrete dynamical systems (Vichniac 1984) and alternative to partial differential equations (Toffoli 1984).

Special cases of cellular automata are capable to describe complex collective behavior and the simulation of fluid dynamics is one in which the cellular automata proved they are complementary and powerful tools to model phenomena that would normally be the exclusive domain of partial differential equations.

This class was named lattice-gas cellular automata and have not only become a "toy models" for the exploration of the microscopic basis of hydrodynamics, but also tools for the numerical study of complex problems in fluid mechanics.

While the lattice gas may, in principle, be used for nearly any problem in hydrodynamic simulation, many of the most successful applications have involved either a complex fluid, a complex geometry, or both.

In the following we first introduce the FHP model (Boon 1991, Clouquer et al. 1987, Cornubert et al. 1991, Dubrulle et al. 1991, Frisch and Rivet 1986, Frisch et al. 1986, Hayot 1987, Henon 1987a, 1987b, 1992, d'Humieres and Lallemand 1987, 1990, Kadanoff et al. 1987, Orszag and Yakhot 1986, Rivet and Frisch 1987, Rivet et al. 1987, Shimomura et al. 1987, Sommers and Rem 1991, Vichniac 1990, Zanetti 1990, 1991), the first of the wide class of fluid models known as lattice-gas automata (LGA), describe its hydrodynamic limit, and illustrate its ability to simulate the Navier-Stokes equations for both 2D and 3D flow. Further on, we will introduce the later developments of the LGA's, namely, the lattice Boltzmann/LGB (Benzi et al. 1992, Frisch 1991, Higuera et al. 1989, Higuera and Jimenez 1989, Higuera and Succi 1989,

d'Humieres 1992, McNamara and Zanetti 1988, Rivet and Frisch 1988), and Bhatnagar-Gross-Krook models /LBGK (Alexander et al. 1992, Behrend et al. 1994, Boghosian and Taylor 1995, Chen et al. 1992, Chen et al. 1994, Qian et al. 1992, Qian and Orszag 1993).

In the remainder of this overview, we present some of the main applications and numerical experiments that has been performed with lattice-gas models: binary fluid mixture and phase-separation transitions (Alexander et al. 1992, Appert 1993, Appert et al. 1991, Burges and Zaleski 1987, Chan and Liang 1990, Rothman and Keller 1988, Rothman 1992, Rothman and Kadanoff 1994, Rothman and Zaleski 1994), multi-phase flow through porous media (Behrend 1995, Ferreol and Rothman 1995, Flekkoy and al. 1992, Gunstensen 1992, Gunstensen and Rothman 1992, Gutfraid and Ippolito 1995, Lutzko et al. 1990, Olson 1995, Pot 1994, Rothman 1988 and 1990, Shan and Chen 1992, Schwartz 1995), diffusion (Burges and Zaleski 1987, Brieger and Bonomi 1991, Chopard and Droz 1988, d'Humieres et al. 1988, van der Hoef and Frenkel 1991, McNamara 1990, Qian et al. 1992), reaction-diffusion equation (Dab et al. 1990, Liu and Goldenfeld 1991, Wells et al. 1991, Gerits and Ernst 1993, Lawniczak and al. 1991), magneto-hydrodynamics (Chen et al. 1992, Hatori and Montgomery 1987, Martinez et al. 1993), free boundary flows (Cliffe et al. 1991, Mujica-Fernandez 1991, Eggels 1995, Eggels and Sommers 1995, Skordos 1995, Teixeira 1992, Alexander et al. 1992), transport of particle suspensions (Behrend et al. 1994, Behrend 1995, Ladd 1990, Ladd 1991, Ladd 1994a, Ladd 1994b, Ladd et al. 1995).

2. Lattice-gas cellular automaton models of fluids

Fluid dynamics is an especially good domain for a cellular automaton formulation because, in this case, at the microscopic level, we have many simple atomic elements colliding rapidly with simple interactions which coincides with our intuitive picture of dynamics on a cellular space. While at the microscopic level, physical fluids consists of discrete particles, on a large scale, they seem continuous and can be described by the partial differential equations of hydrodynamics, and in fact, the form of these equations are quite insensitive to microscopic details (changes in molecular interactions laws can affect the transport parameters, such as viscosity, but do not alter the basic form of the macroscopic equations).

This remarkable similitude has not only had implications for statistical mechanics and kinetic theory but also for the numerical simulation of certain hydrodynamic flows.

2. 1. Fluid dynamics

It will be very useful later, in the construction of the discrete model of fluids, to analyze the complementarity between the microscopic (kinetic) approach and the continuum (macroscopic) approach in the recovery of the main equations of fluid dynamics.

2. 1. 1. The continuum approach

The usual way of deriving the Navier-Stokes equations (Batchelor 1967, Landau and Lifschitz 1959, Reif 1988) is to start from the conservation's laws of mass and momentum, applied to small (but big enough to avoid their microscopic structure) surfaces and volumes in a fluid field.

If $\mathbf{v}(\mathbf{x}, t)$ is the vector field of the "macroscopic" fluid cells and Σ a generalized volume in this field, then the total mass, flowing out from Σ has to balance the fluid flow through the surface S (Wolfram 1986, Hasslacher 1987, Rothman and Zaleski 1996) :

$$\oint_{\partial \Sigma} \rho \mathbf{v} \cdot d\mathbf{S} = \int_{\Sigma} \rho \nabla \cdot \mathbf{v} dV \quad (1)$$

where \mathbf{v} is the velocity vector, $\partial \Sigma$ is the boundary of Σ , S is the surface and \mathbf{n} is the normal vector of the surface (positive in the outward direction).

From the Gauss law ($\oint_{\partial \Sigma} \mathbf{A} \cdot d\mathbf{S} = \int_{\Sigma} (\nabla \cdot \mathbf{A}) dV$ where \mathbf{V} is a volume in \mathbf{R}^3 and \mathbf{A} a n -differential form) we have:

$$\oint_{\partial \Sigma} \rho \mathbf{v} \cdot d\mathbf{S} = - \partial_t \int_{\Sigma} \rho dV = \int_{\Sigma} \nabla \cdot (\rho \mathbf{v}) dV \quad (2)$$

From which we obtain the continuity equation (where ∂_t stands for $\frac{\partial}{\partial t}$):

$$\partial_t \rho + \nabla \cdot (\rho \mathbf{v}) = 0 \quad (3)$$

Now, if p is the pressure exerted by the fluid on the unit surface area of an enclosed volume, and $\mathbf{F} = m \mathbf{a} = \rho V \frac{d\mathbf{v}}{dt}$, is the Newton's second law, the total force acting on a volume of fluid due to the remainder of the fluid can be written as: $\mathbf{F} = - \oint_{\partial \Sigma} p d\mathbf{S}$.

Using again the Gauss law, we obtain:

$$\mathbf{F} = - \oint_{\partial \Sigma} p d\mathbf{S} = - \int_{\Sigma} \nabla p dV = \int_{\Sigma} (-\nabla p) dV \quad (4)$$

and therefore the force acting on the unit mass of fluid is $(-\nabla p)$.

Then, from Newton's second law for the unit mass of fluid, and from (4) we have:

$$\mathbf{F} = -\nabla p = \rho \frac{d\mathbf{v}}{dt} = \rho \{ \partial_t \mathbf{v} + (\mathbf{v} \cdot \nabla) \mathbf{v} \} \quad (5)$$

where we used that dv/dt is a total derivative (e.g. $dv = \frac{\partial v}{\partial t} dt + \frac{\partial v}{\partial x} dx + \frac{\partial v}{\partial y} dy + \frac{\partial v}{\partial z} dz$).

Finally, from Eqs. (4) and (5) we obtain the Euler's equation for an ideal dissipation-free fluid, as:

$$\partial_t v + (v \cdot \nabla) v = -\frac{1}{\rho} \nabla p \quad (6)$$

Equations (3) and (6) are a set of inviscid equations for an ideal compressible flow, the pressure variation law being given by the thermodynamic equation of state.

For real fluids we have to take into account the dissipative effect of the viscosity and therefore, for this purpose, it is useful to analyze the momentum flux time change rate.

If ρv is the momentum of the fluid passing through the elementary volume dV , then its time rate of change can be expressed as:

$$\partial_t(\rho v_i) = (\partial_t \rho) \cdot v_i + \rho \cdot (\partial_t v_i) \quad (7)$$

where v_i are the velocity components on the space dimensions.

From (3), (6) and (7) we have then:

$$\partial_t(\rho v_i) = -\partial_i p - \rho v_k \cdot \partial_k v_i - v_i \cdot \partial_k(\rho v_k) \quad (8)$$

where we used the Einstein summation convention (repeated subscripts imply a summation).

Equation (8) is equivalent with:

$$\partial_t(\rho v_i) = -\partial_i p - \partial_k(\rho v_i v_k) \quad (9)$$

which can be written as:

$$\partial_t(\rho v_i) = -\partial_k(p \delta_{ik} + \rho v_i v_k) \quad (10)$$

where δ_{ik} is the Kronecker delta, and the expression $\Pi_{ik}^0 = p \delta_{ik} + \rho v_i v_k$ is the inviscid momentum flux density tensor (Landau and Lifshitz 1959).

Finally, we can write the momentum balance (Euler's equation) in the condensed form:

$$\partial_t(\rho v_i) = -\partial_k(\Pi_{ik}^0) \quad (11)$$

where Π_{ik}^0 is as above and has the significance of the i^{th} component of momentum flowing in the k^{th} direction.

We can generalize this expression for the case of viscous flows as:

$$\partial_t(\rho v_i) = -\partial_k(\Pi_{ik}) \quad (12)$$

where Π_{ik} is the momentum stress tensor, which accounts also for the viscous effects in the fluid.

Usually, Π_{ik} is written in the form:

$$\Pi_{ik} = \Pi_{ik}^0 + \Pi_{ik}^{\text{visc}} \quad (13)$$

where Π_{ik}^0 has the same meaning as before and Π_{ik}^{visc} is the viscous stress tensor which accounts for the viscosity effects (shear and compression) in a Newtonian fluid. To describe the effects of viscous stress, one may introduce an unknown tensor π_{ik} , so as $\Pi_{ik}^{\text{visc}} = -\rho \pi_{ik}$, and therefore, the momentum stress tensor now reads:

$$\Pi_{ik} = \Pi_{ik}^0 - \rho \pi_{ik} = p \delta_{ik} + \rho v_i v_k - \rho \pi_{ik} = \pi'_{ik} + \rho v_i v_k \quad (14)$$

where π_{ik} is the viscosity stress tensor and $\pi'_{ik} = p \delta_{ik} - \rho \pi_{ik}$ is called the stress tensor.

The general form of π_{ik} can be deduced from some basic facts: in the assumption of small velocity gradients $\pi'_{ik} \propto \partial_k v_i$, and $\pi_{ik} = 0$ for $\mathbf{v} = 0$ and under rotation (uniform rotation doesn't produce transport of momentum overall).

The general form that fulfill these assumptions can be written as:

$$\pi_{ik} = A(\partial_k v_i + \partial_i v_k) + B \delta_{ik} \partial_j v_j \quad (15)$$

and, therefore, the viscous stress tensor will be:

$$\Pi_{ik}^{\text{visc}} = -\rho A(\partial_k v_i + \partial_i v_k) - \rho B \delta_{ik} \partial_j v_j = -\mu(\partial_k v_i + \partial_i v_k) - \xi \delta_{ik} \partial_j v_j \quad (16)$$

where μ is the dynamic shear viscosity and ξ is the bulk viscosity.

Now, from Eqs. (12), (13), and (16) we obtain:

$$\partial_t(\rho v_i) = -\partial_i \left[p \delta_{ik} + \rho v_i v_k - \mu(\partial_k v_i + \partial_i v_k) - \xi \delta_{ik} \partial_j v_j \right] \quad (17)$$

that finally can be written as:

$$\partial_t(\rho v_i) + \partial_k(\rho v_i v_k) = -\partial_i p + \partial_k[\mu(\partial_k v_i + \partial_i v_k)] + \partial_i(\xi \partial_j v_j) \quad (18)$$

which is the momentum conservation equation for a compressible viscous fluid.

In the assumption of an incompressible fluid ($\rho = \rho_0$, constant) and $\partial_k v_k = 0$, the Navier-Stokes equations will read:

$$\partial_t v_i + (v_j \partial_j) v_i = -\frac{1}{\rho} \partial_i p + \nu \frac{\partial^2}{\partial_k \partial_k} v_i \quad (19)$$

where $\nu = \frac{\mu}{\rho}$ is the kinematic shear viscosity. In vector form, Eq. (19) will be:

$$\partial_t \mathbf{v} + (\mathbf{v} \cdot \nabla) \mathbf{v} = -\frac{1}{\rho} \nabla p + \nu \nabla^2 \mathbf{v} \quad (20)$$

2. 1. 2. The kinetic approach

The Navier-Stokes equations of fluid dynamics, are highly non-linear and therefore they allows for analytic solutions only for special cases. Usually they can be resolved only by approximation techniques, the analysis of Navier-Stokes equations still remaining a mater of ingenious techniques covering only particular regimes and specific geometry (Frisch et al. 1987, Hasslacher 1987, Wolfram 1986). Therefore, complementary technique had to be developed, in order to approach other real-world applications of the fluid dynamics.

The kinetic approach, is such an alternative, in which we introduce some “smoothed” values of the “real” fluid parameters, in order to reduce the number of degrees of freedom to just a few and to be able to describe its micro-dynamics. This assumption ignores all the system characteristics below a certain threshold of the time and space scales, and recover the “mean” behavior of the fluid, in the statistical meaning, after averages on sufficiently long time and over large enough microscopic ensembles.

The basic equations of the kinetic theory give the evolution equation of $f(\mathbf{t}, \mathbf{x}, \Omega)$, the one-particle phase-space distribution function, in the presence of the collisions. The distribution function $f(\mathbf{t}, \mathbf{x}, \Omega)$, gives the complete statistical description of the atomic “ensembles” and is used to define the average values of the fluid. Usually the average values are computed over physical volumes $dV \approx L^3$, where the characteristic length, L , is much larger than l_m , the particle mean free path, and much smaller than L_g , the global space length (it is quite obvious that we have $l_m \ll L \ll L_g$).

In the absence of collisions, we have the equation of conservation of the phase-space, (the Liouville's theorem):

$$\frac{df}{dt} = 0 \quad (21)$$

where d/dt is a total derivative. For an isolated system we can write df/dt as (using the Einstein summation rule):

$$\frac{df}{dt} = \partial_i f + v \cdot \nabla f \equiv \partial_i f + v_i \partial_i f \quad (22)$$

which represents the local change in f per unit time due only to the motion of particles.

Now, if we want to introduce the collision effects, the Liouville's equation becomes:

$$\frac{df}{dt} = C(f) \quad (23)$$

where $C(f)$ is a function that models the rate of change of f caused by collisions.

A simple approximation for the collision operator was given first by Boltzmann as a gain-minus-loss operator: $C(f) = (G - L)$.

Following Landau's argumentation, let's assume a two body collision process, of particles 1 and 2, with incoming distribution functions, f_{10} , f_{20} , and outgoing distribution functions, f_{1c} , f_{2c} . If particle 1 occupied the phase-space $d\Omega_{01}$ before the collision and $d\Omega_{0c}$ after collision (the same for type-2 particle: $d\Omega_{02}$ is phase-space before the collision, and $d\Omega_{0c}$ after the collision), $d\Omega_{0c}$ will not be in $d\Omega_{01}$ after collision and the particle 1 is said to be lost.

The probability of loss will be proportional with the number of particles already in the volume dV , namely f_{10} , the number of type-2 particles that enter the volume from the phase-space range $d\Omega_{02}$, namely $g_2 \cdot d\Omega_{02}$, the total volume of allowed outgoing phase-space, $d\Omega_{1c} d\Omega_{2c}$, and the probability of the collision process $P_f \{\Omega\}$.

If $N(t, \mathbf{x})$, is the density function of particles over all space, therefore $[N(t, \mathbf{x}) dV]$ is the mean number of particles in the volume dV and the total number of losses L , from the phase-space volume element $dV d\Omega$, due to the binary collision process, can be written:

$$L = \int P_f \{\Omega\} f_1 f_2 d\Omega_2 d\Omega_{2c} d\Omega_{1c} dV d\Omega \quad (24)$$

Similarly, particle gain into the phase-space volume $d\Omega$ can only come from the reversed processes, f_{1c} , f_{2c} to f_{10} , f_{20} , with fixed $d\Omega_{01}$ and summed over all $d\Omega_{1c}$, $d\Omega_{2c}$, $d\Omega_{02}$:

$$G = \int P_f\{\Omega\} f_{1c} f_{2c} d\Omega_2 d\Omega_{2c} d\Omega_{1c} dV d\Omega \quad (25)$$

The Boltzmann form of the ($G - L$) collision term assumes only two-body collisions, pairwise statistically independent, with detailed (or at most semi-detailed) balance symmetry for collision probabilities.

From (23), (24) and (25) we finally obtain the Boltzmann transport equation:

$$(\partial_t + \mathbf{v}_i \partial_i) \cdot f = G - L \quad (26)$$

If the system is uniform in space, any distribution function f will relax monotonically to the macroscopic Maxwell-Boltzmann form:

$$f_{M-B} = \rho \cdot \exp\{-E(\rho, v)\} \quad (27)$$

where the macroscopic variables ρ, v and T (density, macro-velocity and temperature) are independent of position (\mathbf{x}).

In the non-equilibrium case, any distribution function will relax monotonically in velocity space to a local Maxwell-Boltzmann form and therefore ρ, v and T will depend of space and time.

In order to recover the Euler equation, at the macroscopic scale, from the Boltzmann transport equation, we use the conservation laws for the collisions (we assumed that collisions preserve the conservation laws for mass and momentum exactly, in obtaining the Boltzmann equation):

$$\int C(f) d\Omega = 0 \quad (28)$$

and respectively:

$$\int \mathbf{v} \cdot C(f) d\Omega = 0 \quad (29)$$

The integration of the Boltzmann equation will then read:

$$\int (\partial_t + \mathbf{v}_i \partial_i) \cdot f d\Omega = \int (G - L) d\Omega \quad (30)$$

and respectively:

$$\int \mathbf{v} \cdot (\partial_t + \mathbf{v}_i \partial_i) \cdot f d\Omega = \int \mathbf{v} \cdot (G - L) d\Omega \quad (31)$$

From (30) we obtain, after integration and using (28), the continuity equation:

$$\left[\partial_t \rho + \partial_i (\rho v_i) \right] = 0 \quad (32)$$

where $\rho(t, \mathbf{x}) = \int f(t, \mathbf{x}, \Omega) d\Omega$ is the macroscopic density of the gas, and $\mathbf{v} = \frac{1}{\rho} \int \mathbf{u} \cdot f(t, \mathbf{x}, \Omega) d\Omega$ is the macroscopic velocity vector of the gas, and \mathbf{u} its microscopic velocity vector.

From (31) we will obtain, after integration, the momentum tensor equation:

$$\left[\partial_t (\rho v_i) + \partial_j \Pi_{ij} \right] = 0 \quad (33)$$

where the momentum flux tensor is given by:

$$\Pi_{ij} = \int v_i v_j f d\Omega \quad (34)$$

As we assumed before, to obtain the Boltzmann equation, in each elementary volume of gas, dV , we have a local Maxwell-Boltzmann distribution, and in this assumption it can be shown from (34) that the momentum flux tensor has the form: $\Pi_{ij} = \rho v_i v_j + \delta_{ij} p$, where p is the pressure.

With this expression for Π_{ij} , we obtain from (33) the same expression for the Euler's equation as in (12), from the continuum hypothesis.

To recover the Navier-Stokes equation from the kinetic theory, as usual we assume that the gas reaches local equilibrium in a collision time, the one-particle distribution function $f(t, \mathbf{x}, \Omega)$, has a local Maxwell-Boltzmann form, f_l , and the collective modes develop at large distances and at times much greater than the molecular collision times.

Following the Hilbert's approach (later used in a some-what different form by Chapman and Enskog to derive the transport coefficients for the macro-dynamic equations), it can be assumed for $f(t, \mathbf{x}, \Omega)$, a perturbation expansion of type (Hasslacher 1987, Wolfram 1986):

$$f = f_l (1 + \epsilon^{(1)} + \epsilon^{(2)} + \dots) \quad (35)$$

which can be written also in spatial gradient expansion as:

$$f = f_l (1 + b_1(\mathbf{v}) \cdot (\lambda \nabla) + b_2(\mathbf{v}) \cdot (\lambda \nabla)^2 + \dots) \quad (36)$$

where λ is the mean free path (mfp) of gas particles and \mathbf{v} is the macro velocity. The expansion has to verify at its n -th order the integral equation:

$$B_n = f_l C(\mathcal{E}^{(n)}) \quad (37)$$

where C is the Boltzmann collision operator from (23) and B_n is an operator that depends only on lower order spatial derivatives. This generates a recursive relation for $\mathcal{E}^{(n)}$, whose solubility conditions at order (n) are the $(n-1)^{\text{th}}$ order hydrodynamic equations.

If we assume $n=1$ (the first order expansion in \mathcal{E}) will have:

$$f = f_l(1 + \mathcal{E}^{(1)}) \quad (38)$$

and from (26) we can write (keeping only the first order expansion in the collision operator and putting $\mathcal{E}^{(0)} = 0$ in the streaming operator):

$$\left[\partial_t + \mathbf{v}_i \partial_i + \mathbf{a}_i \frac{\partial}{\partial \mathbf{v}_i} \right] \cdot f_l = f_l C(\mathcal{E}^{(1)}) \quad (39)$$

which is of the form (37): $B_1 = f_l C(\mathcal{E}^{(1)})$.

From the solubility conditions (the Euler equation for ρ , \mathbf{v} and T , and the ideal gas equation of state) of (39), B_1 must be orthogonal to the five of the zero eigenmodes of $C(\mathcal{E}^{(1)}) = 0$ (the solution are 1, \mathbf{v} and \mathbf{v}^2).

In this way we obtain a sequence of hydrodynamic equations, with explicit forms for the transport coefficients, and from which the order zero gives the Euler equation, order one gives the Navier-Stokes equation and order two and higher give the generalized hydrodynamic equations (they have some validity only in some special situations). Solving explicitly for the various $\mathcal{E}^{(n)}$, provides a way of evaluating the transport coefficients (e.g. viscosity) of the macro hydrodynamic equations.

2. 2. The FHP models

The kinetic approach, in its essential features, was used to devise the simplest deterministic local rules, made for a collection of few-bit, finite-state machine, that has the Navier-Stokes equations as its macro-dynamical description (we named here the lattice-gas cellular automaton fluid).

In constructing the lattice model of a fluid, one introduces major simplifications (of considerable computational convenience), by discretizing space (point particles on a lattice), time and velocity. Each node on the lattice will be updated each time step according to a set of collision rules, connecting the neighboring nodes of the lattice, rules that satisfy conservation laws of mass (i.e. particle number), momentum and energy (fig. 1).

The first fully deterministic lattice-gas model with discrete time, positions and velocities was introduced by Hardy, de Pazzis and Pomeau in 1976, on a square lattice (HPP), but it has had only limited applications because its hydrodynamic limit is anisotropic (consequence of the constraints imposed by the square lattice). The difficulties of the HPP model in coping with the full fluid dynamics were overcome in the model proposed by Frisch, Hasslacher and Pomeau (FHP) in 1986 (Frisch et al. 1986), for the 2D, and that of d'Humieres, Lallemand and Frisch for the 3D case (d'Humieres et al. 1986).

The FHP model (Frisch et al. 1987, Hasslacher 1987, Wolfram 1986) is constructed of discrete, identical particles which move from site to site on a triangular matrices, colliding when they meet, always conserving particle number and momentum. No more than one particle may reside at a given site and move with a given velocity (the exclusion principle) and thus each node of the lattice can be described by a six-bit word whose ones represent particles moving with the velocities associated with their bit positions within the word.

Each discrete time step of the lattice-gas is composed of two steps: first, each particle hops to a neighboring site, in the direction given by its velocity, and in the second one, the particle may collide, conserving mass and momentum (In Figure 1: Each arrow represents a particle of unit mass moving with unit speed, one lattice unit per time step, in one of six possible directions given by the lattice links).

The precise collision rules are parameters of the model, and could be deterministic or non-deterministic. In the deterministic case, for a head-on collision with input particles on channels $(i, i+3)$, there are two possible pairs of output channels, such as mass and momentum are conserved, namely $(i+1, i+4)$ (see figure 2a). We can decide to choose always only one of these channels, and consequently we have a deterministic model. The deterministic models are not invariant under mirror-symmetry.

Alternatively, for the non-deterministic models, we can make either, a random choice, with equal probabilities to restore mirror-symmetry, either a pseudo-random choice, dependent on a specific parameter (e.g. parity of time or space index, etc.).

The head-on collision rules, conserve in addition of the mass and momenta, the difference of particle numbers in any pair of opposite directions $(i, i+3)$, which gives a total of four scalar quantities. It means that in addition of mass and momentum conservation, we have a spurious conservation law. The consequence is that the large-scale dynamics of such a model will differ drastically from ordinary hydrodynamics, unless the spurious conservation law is removed. One simple way is to introduce triple collisions: $(i, i+2, i+4) \rightarrow (i+1, i+3, i+5)$ (see figure 2b).

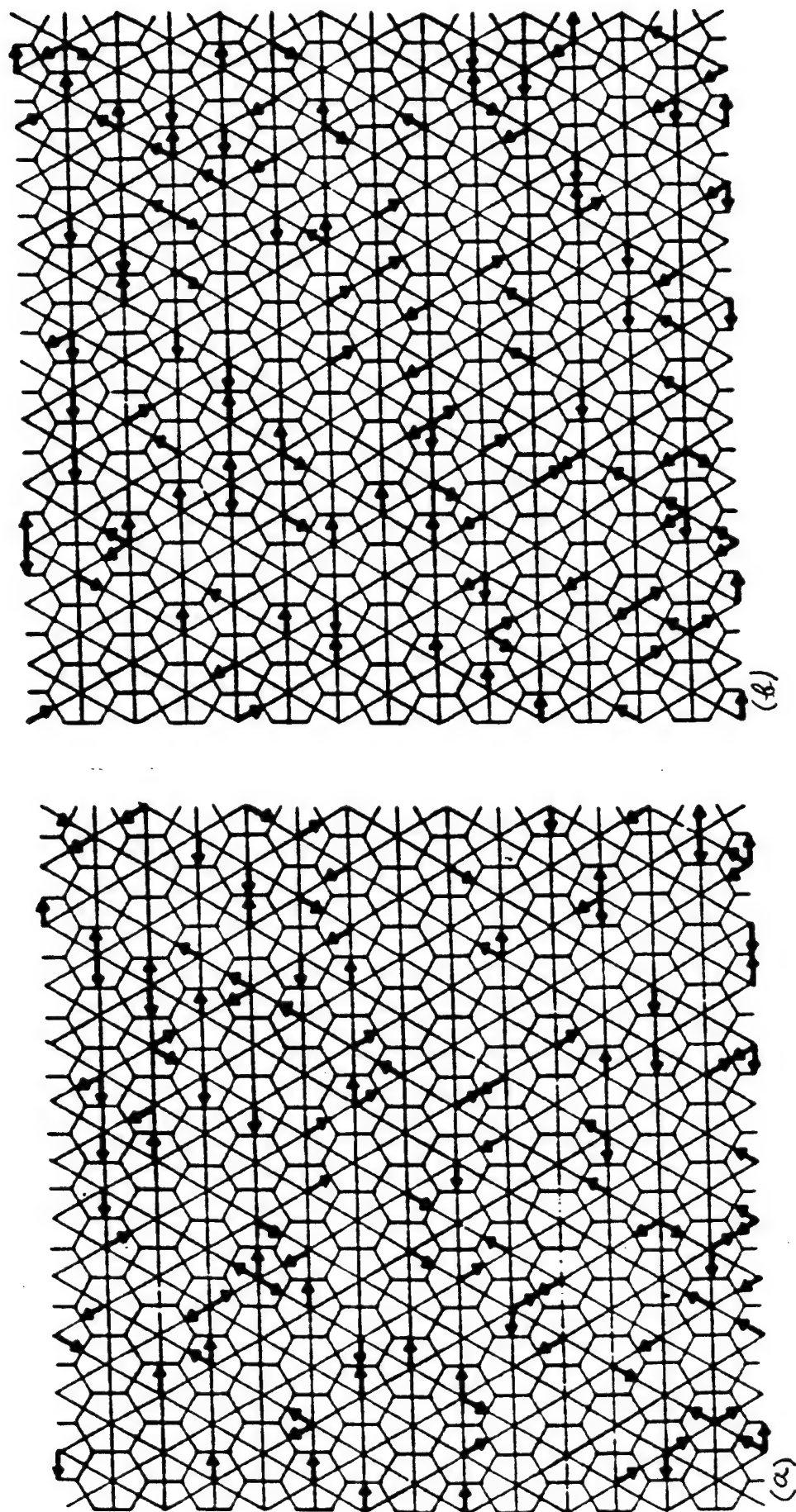


FIGURE 1. Two successive microscopic configurations in the typical cellular automaton fluid model discussed in Section 2. Each arrow represents a discrete "particle" on a link of the hexagonal grid. Continuum behavior is obtained from averages over large numbers of particles.

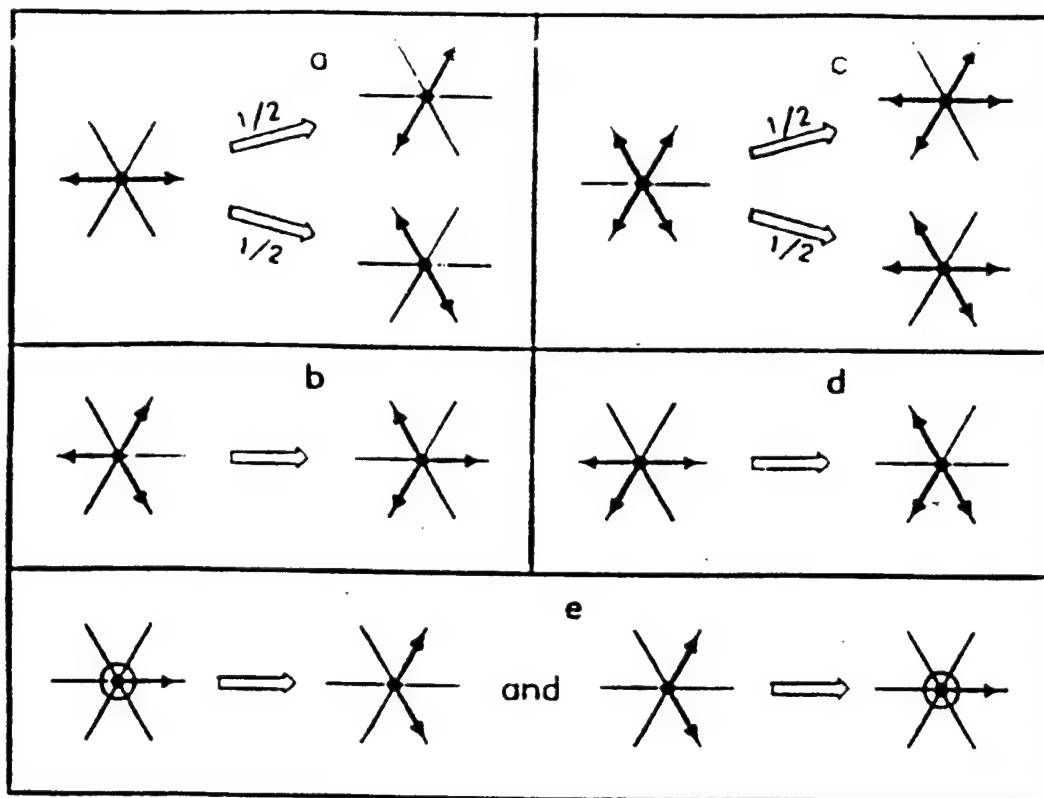
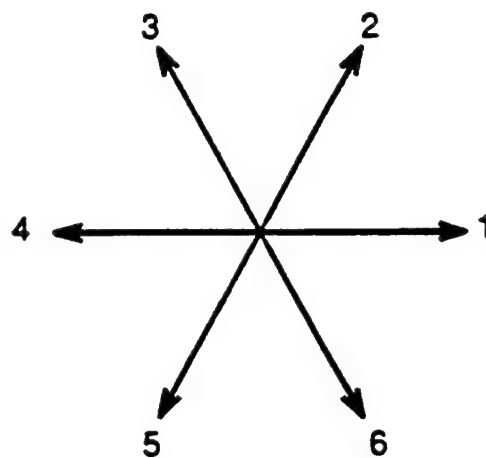


FIGURE 2. Collision rules for the FHP models: (a) head-on collision with two output channels given equal weights; (b) triple collision; (c) dual of head-on collision under particle-hole exchange; (d) head-on collision with spectator; (e) binary collisions involving one rest particle (represented by a circle).



PARTICLE DIRECTIONS IN THE HEXAGONAL MODEL

FIGURE 3. The velocity vector of each particle can point in one of six possible directions. All particles have the same speed c .

Several FHP models has been defined on a triangular lattice (Frisch et al. 1987, McNamara and Zanetti 1987, Chen et al. 1992, Qian et al. 1992, Rothman and Keller 1987). The first one (FHP-I) involves the simplest set of collision rules with no spurious conservation law: pseudo-random binary head-on and triple collisions. FHP-I is not invariant under duality particle/hole exchange, but can be made so by inclusion of the duals of the head-on collisions (see figure 2c). It can be further completed by inclusion of the head-on collisions with "spectator" (particle which remains unaffected in a collision, see figure 4d).

A second type of FHP model (FHP-II), is a seven-bit variant of the FHP-I, including a zero-velocity "rest particle" (see figure 2e for the additional collision rules, and figure 3, for the configurations of the seven bit model). Binary collisions involving rest particles remove spurious conservation, and do so more efficiently at low densities than triple collisions. Finally, the FHP-III model, is a collision-saturated version of the FHP-II model .

The dynamics of the FHP models are invariant under all discrete transformations that conserve the triangular lattice: discrete translations, rotations by $\pi/3$, and mirror-symmetries with respect to a lattice line.

There are two main ways in deriving the usual fluid dynamics equations from the discrete lattice-gas models structure: One starts from the kinetic theory approach (Wolfram 1986, Hasslacher 1987, Rothman and Zaleski 1994) and concentrates on average particle distribution functions, and the other, equivalent approach, concentrates on the microscopic distribution functions (Frisch et al 1987, Rothman and Zaleski 1994). In the following the main aspects of both approaches will be emphasized.

2. 2. 1. The kinetic equations of lattice-gases

The lattice form of the kinetic single-particle distribution function laws, can be obtained from the continuous expressions by making the following identifications between the continuous and discrete probabilistic formalism:

$$f(t, \mathbf{x}, \Omega) \rightarrow f_i(\mathbf{x}, t) \quad (40)$$

$$\int f(t, \mathbf{x}, \Omega) d\Omega \rightarrow \sum_i f_i(\mathbf{x}, t) \equiv \rho \quad (41)$$

$$\rho \mathbf{v} \rightarrow \sum_i \mathbf{c}_i f_i(\mathbf{x}, t) = \rho \mathbf{u} \quad (42)$$

where f_i is the discrete single-particle distribution function, giving the probability of finding a particle with velocity \mathbf{c}_i at position \mathbf{x} and moment t . The \mathbf{c}_i are the components of the particle unit speed on the directions given by (see figure 4):











n	jx	jy		folds
0	0	0		1
1	0	0		1
1	2	0		6
2	0	0		1
2	2	0		6
2	3	2		6
3	0	0		1
3	2	0		6
3	3	2		6
3	4	0		6

FIGURE 4. List of configurations for the seven-bit models. Configurations with four particles and more are obtained by duality replacing particles by holes and holes by particles.

$$\mathbf{c}_i = \left\{ \cos \frac{2\pi i}{6}, \sin \frac{2\pi i}{6} \right\}, \quad i = 1, 2, \dots, 6. \quad (43)$$

With these notations, the lattice-gas equivalent of Liouville's theorem (21) from the continuum kinetic theory (conservation of the probability in the absence of collisions), can be written as:

$$f_i(\mathbf{x} + \mathbf{h}, t + k) - f_i(\mathbf{x}, t) = 0 \quad (44)$$

where $\mathbf{h} = \mathbf{c}_i d_x$, $k = d_t$, and $d_x, d_t \ll 1$.

If we expand the first term of the equation (44) out to $O^2(h, k)$ using the Taylor series expansion:

$$f_i(\mathbf{x}_0 + \mathbf{h}, t_0 + k) = \sum_{\lambda=0}^{m-1} \frac{1}{\lambda!} (h \partial_x + k \partial_t)^\lambda f_i(\mathbf{x}_0, t_0) + O(h^3, k^3) \quad (45)$$

we obtain :

$$d_t \partial_t f_i + d_x \mathbf{c}_i \cdot \nabla f_i + \frac{1}{2} d_t^2 \partial_t^2 f_i + \frac{1}{2} d_x^2 (\mathbf{c}_i \cdot \nabla)^2 \partial_t f_i + d_x d_t (\mathbf{c}_i \cdot \nabla) \partial_t f_i = 0 \quad (46)$$

and to the lowest (first) order in h and k we have:

$$\partial_t f_i + \mathbf{c}_i \cdot \nabla f_i = 0 \quad (47)$$

which is the lattice-gas analogous of (22), the kinetic transport equation in the absence of collisions, which expresses the conservation of fluid (the continuity equation). It is the first example of macroscopic equation for the average behavior of a cellular automaton fluid and it implies, as expected, that f_i is unaffected by particle motion in a spatially uniform system.

Now we can write the full Boltzmann equation, including the collisions, similar to (23) from the kinetic theory:

$$\partial_t f_i + \mathbf{c}_i \cdot \nabla f_i = C_i(f) \quad (48)$$

where $C_i(f)$ is the discrete lattice-gas equivalent of the Boltzmann collision operator. It gives the time evolution of f_i in terms of two-particles and higher order distribution functions that appear in $C_i(f)$.

The distribution function f_i typically determine the macroscopic average quantities.

In a uniform system we have $\nabla f_i = 0$ and from (48) will have:

$$\partial_t f_i = 0 \quad (49)$$

Accordingly we can write the lattice-gas form of (28) and (29) from the kinetic theory (with the usual conventions (40), (41) and (42)) as:

$$\sum_i C_i(f) = 0 \quad (50)$$

and respectively:

$$\sum_i \mathbf{c}_i C_i(f) = 0 \quad (51)$$

Further on we have (again just following the path from the kinetic theory) the continuity equation and the momentum conservation equation, that follow from (40)-(41), (49) and (50) as:

$$\partial_t \rho + \partial_\alpha (\rho u_\alpha) = 0 \quad (52)$$

which is the usual continuity equation for the lattice-gases.

Momentum conservation yields respectively:

$$\partial_t \sum_i c_i f_i + \sum_i c_i (c_i \cdot \nabla f_i) = 0 \quad (53)$$

where we now define the momentum flux tensor (Landau and Lifschitz 1959) as:

$$\Pi_{\alpha\beta} = \sum_i c_{i\alpha} c_{i\beta} f_i \quad (54)$$

where the Greek indices label the space dimensions. The momentum stress tensor $\Pi_{\alpha\beta}$ has to be isotropic up to order 4 in order that the leading terms in the momentum equation (corresponding to the convective and viscous terms in the Navier-Stokes equation) be isotropic.

Finally the momentum conservation equation becomes:

$$\partial_t (\rho v_\alpha) + \partial_\alpha \Pi_{\alpha\beta} = 0 \quad (55)$$

For local equilibrium the macroscopic distribution $f_i(\mathbf{x}, t)$ depends only on $\mathbf{v}(\mathbf{x}, t)$ and $\rho(\mathbf{x}, t)$, and assuming that they vary slowly in space and time (which is quite normal for

hydrodynamic processes), and in sub-sonic limit ($\|\mathbf{u}\| \ll 1$), the distribution function $f_i(\mathbf{x}, t)$ can be approximate by a series expansion in macroscopic variables (Chapman-Enskog):

$$f_i = f \left\{ 1 + A \mathbf{c}_i \cdot \mathbf{u} + B \left[(\mathbf{c}_i \cdot \mathbf{u})^2 - \frac{1}{2} \|\mathbf{u}\|^2 \right] + D \left[(\mathbf{c}_i \cdot \nabla)(\mathbf{c}_i \cdot \mathbf{u}) - \frac{1}{2} \nabla \cdot \mathbf{u} \right] + \dots \right\} \quad (56)$$

where A, B, C are undetermined coefficients and we kept only the terms for the standard hydrodynamic phenomena (the first three terms account for the change in microscopic particles densities as a consequence of changes in macroscopic fluid density, and the fourth term represents the first order dependence of the particle densities on macroscopic spatial variations in the fluid density). We used also the relations (41), (42) and:

$$\sum_i c_{i\alpha} c_{i\beta} = \frac{M}{D} \delta_{\alpha\beta} \quad (57)$$

where $M=6$ for a hexagonal lattice and D is the number of space dimensions (2 in this case).

From (41) and (56) we obtain immediately $f = \frac{\rho}{6}$, while from (42) and (56), we obtain $A = 2$. The coefficients B and C has to be obtain only from the explicit solution of (48), including the collision terms. For uniform equilibrium systems with $\mathbf{u} = 0$, all f_i are given by: $f_i = f = \frac{\rho}{6}$.

In this case, the momentum flux tensor (54) is equal with the pressure tensor, given as in standard kinetic theory of gases by:

$$P_{\alpha\beta} = \sum_i c_{i\alpha} c_{i\beta} f = \frac{1}{2} \rho \delta_{\alpha\beta} \quad (58)$$

where we used also (57) for the second equality. It gives the state equation relating the scalar pressure to the number of density of the lattice-gas fluid: $p = \rho/2$.

When $\mathbf{u} \neq 0$, the momentum flux tensor can be evaluated, in the Chapman-Enskog approximation, using the relations:

$$\sum_i c_{i\alpha} c_{i\beta} c_{i\gamma} = 0 \quad (59)$$

and respectively:

$$\sum_i c_{i\alpha} c_{i\beta} c_{i\gamma} c_{i\delta} = \frac{M}{D(D+2)} (\delta_{\alpha\beta} \delta_{\gamma\delta} + \delta_{\alpha\gamma} \delta_{\beta\delta} + \delta_{\alpha\delta} \delta_{\beta\gamma}) \quad (60)$$

Finally we obtain:

$$\Pi_{\alpha\beta} = \frac{\rho}{2} \delta_{\alpha\beta} + \frac{\rho}{4} B[u_{\alpha} u_{\beta} - \frac{1}{2} |\mathbf{u}|^2 \delta_{\alpha\beta}] + \frac{\rho}{4} C [\partial_{\alpha} u_{\beta} - \frac{1}{2} \nabla \cdot \mathbf{u}] \quad (61)$$

Substituting in (55) and using the momentum and continuity equations, we obtain the Navier-Stokes like equation for the lattice-gas fluid:

$$\partial_t(\rho \mathbf{u}) + \frac{B}{4} \rho (\mathbf{u} \cdot \nabla) \mathbf{u} = -\nabla \left(\frac{1}{2} \rho + \frac{1}{2} \rho |\mathbf{u}|^2 \right) - \frac{\rho}{8} C \nabla^2 \mathbf{u} + O(\mathbf{u}^3) \quad (62)$$

The standard form of the Navier-Stokes equation for a continuum fluid in D dimensions can be written as:

$$\partial_t(\rho \mathbf{u}) + \mu \rho (\mathbf{u} \cdot \nabla) \mathbf{u} = -\nabla p + \eta \nabla^2 \mathbf{u} + \left(\zeta + \frac{1}{D} \eta \right) \nabla (\nabla \cdot \mathbf{u}) \quad (63)$$

where p is the pressure, η and ζ are, respectively, shear and bulk viscosity while μ from the convective term, is usually constrained to have value 1 by Galilean invariance.

The form of viscous term in (62) implies that the bulk viscosity $\zeta = 0$, while the value of η is determined by the coefficient C according to:

$$\eta = \rho \nu = -\frac{1}{8} \rho C \quad (64)$$

where ν is the kinematic viscosity.

The convective term in (62) has the same structure as in the standard Navier-Stokes equation but include the coefficient $C/4$, which can be removed by a simple rescaling in velocity: $\mathbf{u}^* = C/4 \mathbf{u}$, where the coefficients B and C can be obtained from the Boltzmann approximation.

From the equation of state $p = \rho/2$ we obtain for sound speed, for the hexagonal lattice,

$$c_s = \frac{c^2}{D} = \frac{1}{\sqrt{2}} \quad (65)$$

where D is the number of space dimensions, and c the lattice unit speed.

For the viscosity, it can be shown (Wolfram 1986, Hasslacher 1987, Rothman and Zaleski 1984) the relation:

$$\nu = \frac{1}{12} \frac{1}{d(1-d)^3} - \frac{1}{8} \quad (66)$$

where $1/8$ is a correction due to the finite size of the lattice, and $d = \rho/M$ is the mass density per cell.

2. 2. 2. The Boolean kinetic equations of lattice-gases

As we saw, the FHP models are defined on a triangular lattice (see figure 3) with unit spacing, and in each node there are six links (\mathbf{c}_i , $i=1,\dots,6$) to its nearest neighbors. Particles of unit mass and velocity move along these links in such a way that they reside in the nodes only at integer times. An exclusion principle governs the occupation of the links: no more than one particle can occupy any a given time a given link.

The state of a node can be describe as a six-bit Boolean variable $\mathbf{n} = \{n_i, i = 1,\dots, 6\}$, where the bit n_i indicates the presence (1) or the absence (0) of a particle in the i -th link.

The evolution of the system, from time (t) to time $(t+1)$ can be decomposed in two phases: collision and propagation. In the propagation phase each particle is displaced in the direction of its velocity: $n_i(\mathbf{r}) \rightarrow n_i(\mathbf{r} + \mathbf{c}_i)$, where \mathbf{r} denotes the sites of the lattice. The collision phase conserve the mass and momentum (in order to recover the Navier-Stokes equations on the macroscopic scale). In order to avoid the presence of the spurious invariant (the difference of particle numbers in any pair of opposite directions) triple collisions and/or rest particles is introduced.

In order to introduce the probabilistic description of the Boolean lattice-gas models, we need some basic assumptions (Frisch et al. 1987):

i. Let $s = \{s_i, i = 1,\dots, b\}$ and $s' = \{s'_i, i = 1,\dots, b\}$, denote the state of a node before and after a collision respectively, with b the number of links per node, and let:

$$A(s \rightarrow s') \quad (67)$$

be the sit-independent transition probability from s to s' . The obvious normalization condition is: $\sum_{s'} A(s \rightarrow s') = 1, \forall s$, and the semi-detailed balance condition then reads:

$$\sum_s A(s \rightarrow s') = 1, \forall s' \quad (68)$$

This equality implies that the situation where all states have the same probability is stationary with respect to collisions.

Will follow the approach from the statistical mechanics: (i) definition of the space phase, (ii) introduction within this set of statistical ensemble of initial conditions with a given probability distribution, (iii) evolution of probability distribution from the Liouville equation, (iv) calculation of the average values using the evolved probability distribution.

2. 3. The Lattice-gas Boltzmann method

Due to the boolean dynamics of LGA's all simulations performed by this technique are affected by the statistical noise, and to get resonably resolved macroscopic fields it is necessary to average over a possible combination of large regions of the lattice, long times and a wide range of initial conditions.

In addition lattice-gases usually are not Galilean invariant (presence of the so called $g(\rho)$ factor in the nonlinear advection term in the Navier-Stokes equation), they have a velocity-dependent pressure and they present spurious invariants that correspond to unphysical hydrodynamic quantities.

The problem of noise will disappear if in the boolean form of the Boltzmann equation (94) will consider real variables N_i instead of the boolean ones (McNamara and Zanetti 1988):

$$N_i(\mathbf{x} + \mathbf{c}_i, t+1) - N_i(\mathbf{x}, t) = \Delta_i(N) \quad (102)$$

where $\Delta_i(N)$ is obtained from the boolean collision term by substituting the boolean population n_i with the ensemble averaged population N_i .

In the double limit of small Knudsen and Mach numbers we can expand the lhs of (102) as (Higuera and Jimenez 1989):

$$N_i = N_i^{eq}(\rho, \mathbf{v}) + N_i^{neq}(\partial\rho, \partial\mathbf{v}) \quad (103)$$

and further decompose N_i^{eq} as:

$$N_i^{eq} = N_i^{(0)} + N_i^{(1)} + N_i^{(2)} + O(v^3) \quad (104)$$

where the upper index refers to the order in v , and N_i^{eq} has the form in (77).

The corresponding expansion of the collision operator is:

$$\Delta_i = \Delta_i(N^{(0)}) + \frac{\partial \Delta_i}{\partial N_j} N_j^{(1)} + \frac{\partial \Delta_i}{\partial N_j} (N_j^{(2)} + N_j^{(neq)}) + \frac{\partial^2 \Delta_i}{2 \partial N_j \partial N_k} N_j^{(1)} N_k^{(1)} \quad (105)$$

where all derivatives are calculated at the state of zero velocity $N_i = d = \frac{\rho}{b}$.

As for any equilibrium distribution, we have:

$$\Delta_i(N^{eq}) = 0 \quad (106)$$

and using it for the case of uniform equilibria (zero velocity), one obtains also $\Delta_i(N^{(0)})=0$.

Combining equations (105) and (106) one obtains:

$$\frac{\partial \Delta_i}{\partial N_j} N_j^{(1)} + \frac{\partial \Delta_i}{\partial N_j} (N_j^{(2)} + N_j^{(neq)}) + \frac{\partial^2 \Delta_i}{2 \partial N_j \partial N_k} N_j^{(1)} N_k^{(1)} = 0 \quad (107)$$

Plugging (107) into (105) we finally obtain:

$$\Delta_i(N) = A_{ij} (N_j - N_j^{eq}) \quad (108)$$

where A_{ij} is:

$$A_{ij} = \frac{\partial \Delta_i}{\partial N_j} \quad (109)$$

or, introducing the transition probability:

$$A_{ij} = -\frac{1}{2} \sum_{s,s'} (s - s') A(s \rightarrow s') d^{p-1} (1-d)^{b-p-1} (s_j - s_j') \quad (110)$$

and $p = \sum_i s_i$. The elements a_{ij} of the collision matrix A_{ij} , are in this case numerical parameters which can be change at will and determines the scattering rate between directions i and j (they depend only on the angle between the directions c_i and c_j).

The passage from the complete collision operator to the form (108) is clearly advantageous from the point of view of simplicity and storage requirements of the numerical scheme.

The conservation of mass and momentum gives in terms of the collision matrix:

$$\begin{aligned} \sum_{i=1}^b A_{ij} &= 0 \\ \sum_{i=1}^b c_i A_{ij} &= 0, \quad j=1, \dots, b \end{aligned} \quad (111)$$

For the FHP models the number of possible elements a_{ij} of the collision matrix is four for the 6-particle model and we have to add other two for each rest particle included (one to account for the influence of the resting particle on itself and on the other directions).

If we denote by a_θ the matrix elements such $c_i c_j = c^2 \cos \theta$, and as in the hexagonal lattice the only possible angles are $0, \pi/3, 2\pi/3$ and π , then (111) can be written as:

$$\begin{aligned} a_0 + 2a_{60} + 2a_{120} + a_{180} &= 0 \\ a_0 + a_{60} - a_{120} - a_{180} &= 0 \end{aligned} \quad (112)$$

As the matrix A_{ij} is symmetric and cyclic, the independent coefficients a_θ can be expressed in terms of non zero eigenvalues of the matrix (Wolfram 1986), as:

$$\begin{aligned} \lambda &= 6(a_0 + a_{60}) \\ \sigma &= -6(a_0 + 2a_{60}) \end{aligned} \quad (113)$$

with multiplicities 2 and 1 respectively. The eigenvectors are mutually ortogonal and do not depend on the matrix coefficients, and the eigenvectors associated with the eigenvalue λ are the $[D(D+2)/2 - 1]$ linearly independent elements of the set of vectors $Q_{i\alpha\beta}$.

To recover the macrodynamics equations of the in the lattice-Boltzmann method, one can use the same multi-scale expansions around the small parameter ε (the inverse of the wavelength of the typical spatial variation of the fields expressed in the natural units of the lattice). Keeping only the first-order terms in the multi-scale expansion, one obtains the differential equations:

$$\partial_t N_i + (c_i \cdot \partial) N_i = A_{ij} (N_j - N_i^{eq}) \quad (114)$$

In order to better distinguish between the hydrodynamic and non-hydrodynamic fields, it is useful to project the above eqautions onto the eigenvectors of the collision matrix (Frisch te al. 1987). Due to the symmetries imposed by the colision matrix, all the eigenvalues and five of the six eigenvectors ($1, c_{ix}, c_{iy}$ and the two independent components of $Q_{i\alpha\beta}$) of the collision matrix are already known. One can shwon that the other eigenvector is $(-1)^i$. Therefore, the generic population N_i , can be decomposed as:

$$N_i = \frac{1}{6} \rho + \frac{1}{3} \rho c_{i\alpha} \cdot v_\alpha + \frac{2}{3} Q_{\alpha\beta} \cdot S_{\alpha\beta} + \frac{1}{6} (-1)^i \mu \quad (115)$$

To project equation (114) onto the orthogonal basis of the eigenvectors, one can multiply successively by $1, c_{i\alpha}, Q_{i\alpha\beta}, (-1)^i$ and summing over i will obtain:

$$\begin{aligned}
\partial_t \rho + \partial_\alpha J_\alpha &= 0 \\
\partial_t J_\alpha + \partial_\alpha (\rho / 2) + \partial_\beta S_{\alpha\beta} &= 0 \\
\partial_t S_{\alpha\beta} + H_{\alpha\beta} + R_{\alpha\beta\gamma} \partial_\gamma \mu &= \lambda (S_{\alpha\beta} - S_{\alpha\beta}^{eq}) \\
\partial_t S_{\alpha\beta} + 4 R_{\alpha\beta\gamma} \partial_\gamma S_{\alpha\beta} &= \mu \sigma
\end{aligned} \tag{116}$$

with:

$$\begin{aligned}
R_{\alpha\beta\gamma} &= \frac{1}{6} \sum_i (-1)^i Q_{i\alpha\beta} c_{i\gamma} \\
S_{\alpha\beta}^{eq} &= \rho g(\rho) (v_\alpha v_\beta - \frac{1}{2} v^2 \delta_{\alpha\beta}) \\
H_{\alpha\beta} &= \partial_\alpha J_\beta + \partial_\beta J_\alpha - (\partial_\gamma J_\gamma) \delta_{\alpha\beta} \\
g(\rho) &= (3 - \rho) / (6 - \rho)
\end{aligned} \tag{117}$$

The non-isotropy introduced by the rotational discretization of the lattice affects the expression of the non-hydrodynamic fields, through the ghost field μ and the higher-order contributions to the stress tensor.

In order to recover the Navier-Stokes equations from (116), one have to use the incompressibility condition ($\rho \equiv \text{const.}$), the adiabatic approximation (the time derivative term in equation of stress tensor $S_{\alpha\beta}$ be much smaller than the other terms in the same equation), and finally to analyse the contribution of the different fields in the above equations.

From (116) one can observe that the various fields have the following order of magnitude:

$$\begin{aligned}
S &\approx v^2 + \varepsilon v \\
\eta &\approx \varepsilon v^2 + \varepsilon^2 v \\
\mu &\approx O(\varepsilon \eta)
\end{aligned} \tag{118}$$

and as the corrections at (116) are at least of second order, the rates η / S and μ / S tend to zero as $\varepsilon \rightarrow 0$ and therefore the ghost fields can be neglected with respect to the hydrodynamic fields.

Substituting the stress tensor corresponding to these assumptions in the current equation from (116) one obtains the Navier-Stokes equations, apart from the usual constant factor $g(\rho)$ which can be easily rescaled out.

2. 4. The Lattice-gas Boltzmann / Bhatnagar-Gross-Krook method

The lattice-gas Boltzmann / Bhatnagar-Gross-Krook (LBGK) method is a further abstraction of the initial concept of lattice-gas models. As in Lattice-gas Boltzmann method, the population densities are real numbers (and not boolean variables as in the original LGA models), the statistical noise is completely suppressed and the spurious invariants are easily controlled.

However, what is new in the LBGK method is that the problem of velocity-dependent pressure is resolved by using a Maxwellian distribution function that violates the semi-detailed balance of binary collisions, instead of the Fermi-dirac one used in the classical Lattice-Boltzmann method, and introduces more populated rest particles (Qian et al. 1992, Chen et al. 1992).

The Boltzmann kinetic equation was written as in the relaxation method from the computational fluid dynamics as:

$$N_i(\mathbf{x} + \mathbf{c}_i, t+1) = (1 - \tau)N_i(\mathbf{x}, t) + \tau N_{ie}(\mathbf{x}, t) \quad (119)$$

where N_i is the density function of particle i , \mathbf{c}_i its velocity and τ the relaxation parameter (from the computational fluid dynamics the relaxation parameter τ has to be between 0 and 2 to ensure the stability of the method).

The relaxation process is used in order to replace the collision term (without changing the propagation term).

The equilibrium distribution (up to the second order to have the correct nonlinear term in the Navier-Stokes equation) N_{ie} , is:

$$N_{ie}(\mathbf{x}, t) = t_p \rho \left\{ 1 + \frac{c_{i\alpha} u_\alpha}{c_s^2} + \frac{u_\alpha u_\beta}{2c_s^2} \left(\frac{c_{i\alpha} c_{i\beta}}{c_s^2} - \delta_{\alpha\beta} \right) \right\} \quad (120)$$

where α and β represent the Cartesian coordinates (with implied summation for repeated indices), c_s is the speed of sound, the index p is the square modulus of particle's velocity, and t_p is the corresponding equilibrium distribution for $\mathbf{u} = 0$. The t_p 's are determined to achieve the isotropy of the fourth-order tensor of velocities and Galilean invariance (Qian et al 1992).

The difference from the classical Lattice-Boltzmann method is that the collision matrix A_{ij} is now replaced only by a single value τ .

Using the multi-scale technique from the lattice-gas models one can obtain the Navier-Stokes equations at the second order of approximation:

$$\begin{aligned} \partial_t \rho + \partial_\alpha (\rho u_\alpha) &= 0 \\ \partial_\alpha (\rho u_\alpha) + \partial_\alpha (\rho u_\alpha u_\beta) &= -\partial_\alpha (\rho c_s^2) + \nu \partial_\beta [\partial_\beta (\rho u_\alpha) + \partial_\alpha (\rho u_\beta)] \end{aligned} \quad (121)$$

where $c_s = \frac{1}{\sqrt{3}}$ is the speed of sound, and $\nu = \frac{1}{6}(\frac{2}{\tau} - 1)$ is the viscosity and there are independent of space dimension. For small τ 's the finite size of the lattice gives a big Knudsen number and the results diverges from the previous ones because the system now describes a rarefied gas

instead of hydrodynamics. It is remarkable that by a proper choice of the equilibrium distribution the lattice-gas BGK method was able to simulate the fluid dynamics (as it leads to Navier-Stokes equations) and it suggests that through a properly chosen equilibrium distribution a wide range of non-linear partial differential equations can be simulated in a simple and efficient way.

2. 5. The 3D lattice-gas models

Three dimensional regular lattices do not have enough symmetry to ensure macroscopic isotropy and therefore the way out of this problem was to move to a higher-dimensional lattice, the face-centered hypercubic (FCHC) lattice (figure 5).

The nodes (x_1, x_2, x_3, x_4) of the lattice satisfy the condition: $x_1 + x_2 + x_3 + x_4 = \text{even}$, where x_i 's are integers numbers. In each node there are 24 links to its nearest neighbours (indicated as c_i , $i = 1, \dots, 24$) of length $\sqrt{2}$. Propagation and collision are defined in the same spirit as in FHP models.

In the applications the 3D hydrodynamics periodic boundary conditions are imposed along the x_4 direction in a layer of thickness 2 (along the x_3 direction) The thick black line in figure 5 have a different weight in the sense that two particles can propagate along these directions, according to the two values of the fourth component of the velocity $(c_i)_4 = \pm 1$.

It can be shown (Frisch et al. 1987) that the conserved fourth component of the momentum behaves as a passive scalar not influencing the other three (there is not a spurious invariant).

Consider a FCHC lattice in a space of $D = 4$ dimensions, with b_m particles of unit mass per node, moving with velocities c_i ($i = 1, \dots, b_m$). The component α ($\alpha = 1, \dots, D$) of these velocities is denoted by $c_{i\alpha}$, and the norm $\|c\|$, by c . M_c particles of unit mass and zero velocity are also present at each node of the FCHC lattice.

If $N_i(\mathbf{r}, t)$ ($i = 1, \dots, b_m$) is the mean population of moving particles at the node \mathbf{r} and time t , and $N_0(\mathbf{r}, t)$ is the mean population of each rest particle, the as usual we can write the Boltzmann equation for the lattice-gas as:

$$N_i(\mathbf{r} + \mathbf{c}_i, t+1) = N_i(\mathbf{r}, t) + \Delta_i [N_1(\mathbf{r}, t), N_2(\mathbf{r}, t), \dots, N_{b_m}(\mathbf{r}, t), M_c N_0(\mathbf{r}, t)] \quad (122)$$

with $i = 1, \dots, b_m$, which enable us to calculate the mean populations at time step $(t+1)$, provided that the function Δ_i , is known.

The usual conservation relations for mass and momentum read:

$$\sum_{i=1}^{b_m} N_i(\mathbf{r} + \mathbf{c}_i, t+1) + M_c N_0(\mathbf{r}, t+1) = \sum_{i=1}^{b_m} N_i(\mathbf{r}, t) + M_c N_0(\mathbf{r}, t) \quad (123)$$

..... $v_4 = 0$

———— $v_4 = +1$ and -1

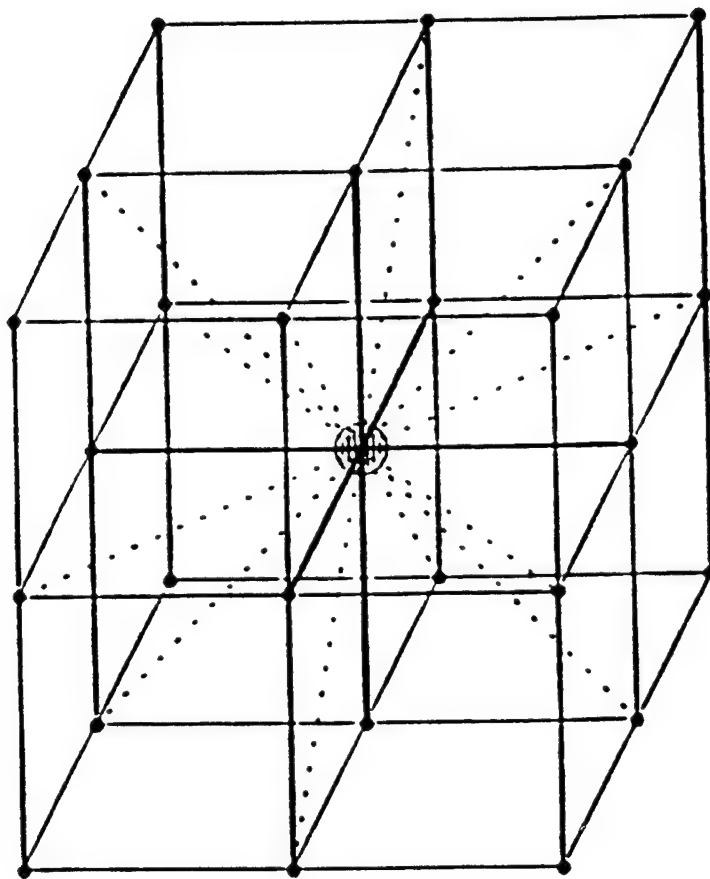


FIGURE 5. The pseudo-four-dimensional FCHC model. Only the neighborhood of one node is shown. Along the dotted links, connecting to next-nearest neighbors, at most one particle can propagate, with component $v_4 = 0$; along the thick black lines, connecting to nearest neighbors, up to two particles can propagate, with components $v_4 = \pm 1$.

and respectively:

$$\sum_{i=1}^{b_m} \mathbf{c}_i N_i(\mathbf{r} + \mathbf{c}_i, t+1) = \sum_{i=1}^{b_m} \mathbf{c}_i N_i(\mathbf{r}, t) \quad (124)$$

The macroscopic quantities ρ and $\rho \mathbf{u}$, are related with these mean populations by:

$$\rho(\mathbf{r}, t) = \sum_{i=1}^{b_m} N_i(\mathbf{r}, t) + M_c N_0(\mathbf{r}, t) \quad (125)$$

$$\rho \mathbf{u}(\mathbf{r}, t) = \sum_{i=1}^{b_m} \mathbf{c}_i N_i(\mathbf{r}, t)$$

At equilibrium, it can be shown (Frisch et al., d'Humieres et al. 1987) that the mean populations are given by a Fermi-Dirac distribution:

$$N_i^{eq}(\mathbf{r}, t) = [1 + \exp(h + \mathbf{q} \cdot \mathbf{c}_i)]^{-1} \quad (126)$$

From (126) and (125) the mean population can be expressed in terms of \mathbf{u} and ρ and the unknown functions can be expanded as a Taylor series around $\mathbf{u} = 0$.

Finally after the standard Chapman-Enskog expansion, rescaling and the multi-scale formalism, the mean population $N_i(\mathbf{r}, t)$ can be written as:

$$N_i(\mathbf{r}, t) = N_i^0(\mathbf{r}, t) + \varepsilon N_i^1(\mathbf{r}, t) + \varepsilon^2 N_i^2(\mathbf{r}, t) + \dots \quad (127)$$

where $\varepsilon = 1/L$, with l the lattice unit and L the domain dimension.

From the conservation equations and (127), up to a second order expansion one will obtain the Navier-Stokes equations:

$$\partial_t \rho + \nabla \cdot (\rho \mathbf{u}) = 0 \quad (128)$$

$$\partial_t (\rho \mathbf{u}) + \nabla \cdot \mathbf{P} = \nabla \cdot [v(\rho) \nabla (\rho \mathbf{u})] + \nabla \cdot \left[\left[v(\rho) \frac{(\mathbf{D} - 2)}{\mathbf{D}} + \xi \right] \nabla \cdot (\rho \mathbf{u}) \right]$$

where the momentum flux \mathbf{P} is expressed as:

$$\mathbf{P} = \rho c_s^2 \left[1 - g(\rho) \left(\frac{u}{c} \right)^2 [1 + 0.5(D - (\frac{c}{c_s})^2)] \right] \mathbf{I} + g(\rho) \rho \mathbf{u} \cdot \mathbf{u} \quad (129)$$

The so-called galilean factor is given by:

$$g(\rho) = \frac{Db(1-2d)}{(D+2)b_m(1-d)} \quad (130)$$

and the shear viscosity ν and the bulk viscosity ξ can be written as:

$$\nu = -\frac{b_m c^2}{D(D+2)} \psi - \frac{c^2}{2(D+2)} \quad (131)$$

$$\nu = -\frac{b_m c^2}{D} \chi - \frac{1}{2}(\frac{c^2}{D} - c_s^2)$$

The coefficients ψ and χ are derived from the collision operator Δ_i once the collision rules are established.

The Boltzmann-method will read for the FCHC case (Gunstensen and Rothman 1991):

$$N_i(\mathbf{r} + \mathbf{c}_i, t+1) = N_i(\mathbf{r}, t) + \sum_{j=0}^{b_m} A_{ij} [N_j(\mathbf{r}, t) - N_{0j}(\mathbf{r}, t)] W_{ij} \quad (132)$$

with $i = 1, \dots, b_m$, and $W_j = \begin{cases} 1, & \text{for } j \neq 0 \\ M_c, & \text{for } j = 0 \end{cases}$

The collision matrix \mathbf{A} can be decomposed as follows:

$$(A_{ij}) = \begin{pmatrix} c^o & b^o & \dots & b^o \\ b^o & & & \\ \vdots & & & \\ \vdots & & (A'_{ij}) & \\ \vdots & & & \\ b^o & & & \end{pmatrix} \quad (133)$$

The matrix \mathbf{A}'_{ij} corresponds to the collisions between the particles, while the coefficients c^o and b^o correspond to collisions between moving/rest particles and rest/rest particles respectively.

Due to the isotropy of the lattice, the coefficients of \mathbf{A} can only depend on the angle between the velocity vectors \mathbf{c}_i and \mathbf{c}_j and on the FCHC lattice only 5 coefficients are possible: a_0 , a_{60} , a_{90} and a_{180} . At these we have to add another two b^o and c^o for the rest particles.

One can compute all these coefficients in the same way has been done for the 2D Lattice-Boltzmann method.

3. Numerical experiments

Simulations and computations have been performed with lattice-gas models to check the basic properties of lattice-gases, the linear response to small perturbations and the behavior of the transport coefficients.

In the most usual simulations (e.g. the 2D FHP model with rest particles) the state of the system at time t is given by a $L_1 \times L_1$ matrix of 6-7 bit words assigned to each node, and updated regularly by collision + propagation steps.

Boundary and initial conditions are set according to the problem studied. For the wave propagation experiment, as initial conditions is used a uniformly random distribution of particles and velocities, while as boundary conditions the periodic ones are used, in order to confine the system on a torus (particles escaping at one boundary are injected at the opposite one)

For the flow experiments, requires as initial conditions, a biased velocity distribution along a given direction, and boundary conditions that assure the steady flow of incoming particles at the input side and constant density condition at the output boundary. In the experiments with solid boundaries, depending on the specific problem, one have to chose from reflection conditions corresponding to free-slip boundaries (specular reflection, see figure 6a), no-slip boundaries (bounce-back reflection, see figure 6b) or rough surfaces (combination of specular and bounce-back reflections with equal probabilities, see figure 6c). Of course, the dimensions of the obstacles has to be much smaller than size L of the space scale to avoid numerical artifacts, but that in turn implies large number of particles and therefore bigger computer resources.

Typical 2D lattices are of order of 3×10^6 nodes (1024×3027) populated with 6×10^6 particles, i.e. a density $d \approx 0.2$. Stream line maps are obtained by representing the velocity field vectors associated to the fluid elements (for Boolean LGA's by averaging the particles velocities over a number of nodes: 8×8 , 32×32 , etc. depending of the problem).

The usual restrictions regard the space size, the minimal kinematic viscosity and the velocity u which must be small compared to the upper limit c .

3. 1. Poiseuille Flow

Poiseuille flow as first example of quantitative comparison between lattice-gas flow and classical fluid dynamics results, for a system involving both viscous dissipation and non-linear behavior (d'Humieres and Lallemand 1986).

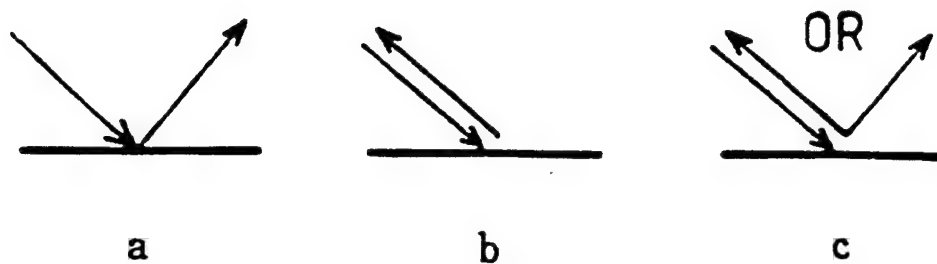


FIGURE 6. Boundary reflections: (a) free-slip; (b) no-slip; (c) combination of (a) and (b).

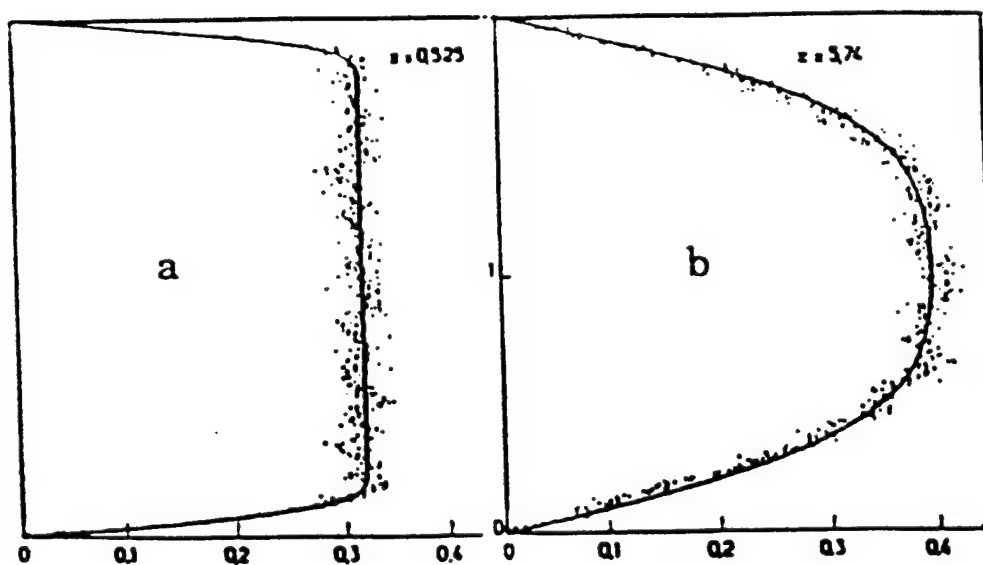


FIGURE 7. Velocity component profile in a channel (a) close to the inlet, and (b) further downstream [relative distances from inlet are ~ 0.5 (a) and ~ 0.6 (b)] (d'Humieres and Lallemand, 1986).

The results presented here was obtained on a 2D FHP lattice-gas model with 512×3072 nodes, filled with a gas with density $d = 0.22$ and uniform velocity, along the horizontal direction, $u = 0.3$.

The system is periodic in the vertical direction and wind-tunnel conditions are considered at the left and right boundary. The Reynolds number in the channel was much smaller than that corresponding to the appearance of turbulence, and steady state was attained after a large enough number of iterations.

In figure 7 the velocity profiles are presented for a region close to the input boundary (Fig. 7a) and for a region located about ten times further downstream, where a characteristic Poiseuille profile has developed.

The agreement between the lattice-gas simulations and the profiles computed by the Slichting method was good and proved that the lattice-gas models could be an alternative at the extremely laborious classical methods of fluid dynamics.

3. 2. Flow past a barrier (von Karaman streets)

Figures 8 and 9 presents simulation results of a flow past a plate (also among the first simulated by the lattice-gas models). This 2D flow is forced by injecting particles at the left boundary of the fluid space and removing them at the right boundary and thus creating a pressure gradient. The flow, at Reynolds number of approximately 300, creates vortices, known also as von Karaman streets, behind the plate. this flow qualitatively matches those that would be obtained from quasi-two-dimensional experiments or other methods of numerical simulation.

The lattice was 2816×1024 nodes with periodic conditions along the y ax and wind-tunnel condition at the left and right edges. Initially, the lattice is filled with a gas of uniform density and speed, with $d = 0.3$ and $u = 0.428$.

The presence of the plate first produces shock waves due to the reflection of the particles at the surface of the plate (figure 8), then eddies start to develop symmetrically on either edges of the plate. When time reaches sufficiently large values, it is found that the symmetry of the flow is broken and vortex shedding by the plate occurs, generating a two-dimensional von Karaman street (figure 9).

The fluid flow past a cylinder, for moderate Reynolds numbers ($R < 100$), was simulated with a lattice-Boltzmann method for the case of homogenous forced turbulent flow (see figure 10). The results were compared against a pseudo-spectral simulation for the same case. Three levels of resolution were adopted: low (64×64), moderate (128×128) and high (512×512). Were examined the range of Reynolds numbers from 10 to 80 and were covered both, the steady flows ($Re < Rec = 46$) and non-steady periodic flow. As boundary conditions, at the upstream edge the mean populations for the incoming directions are set to the equilibrium values corresponding to a prescribed value of the uniform free-stream velocity. The free stream velocity

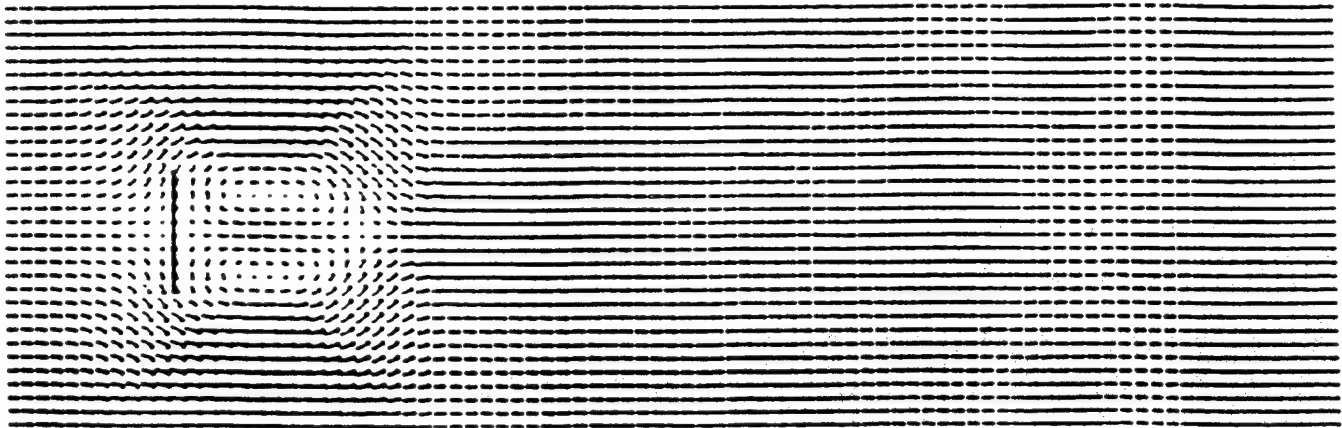


FIGURE 8. Map of the flux of particles in a 886.8×2048 channel 3000 time steps after the introduction of a flat plate of real size 216.5. The distance between the back of the plate and the point where $j_x = 0$ on the axis of the channel is defined as the size of the wake.

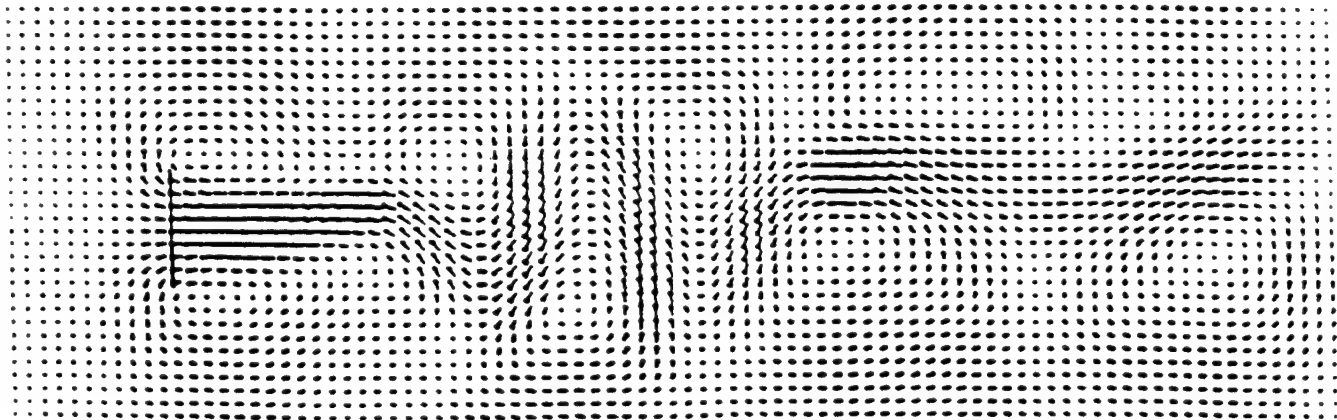


FIGURE 9. Similar to Figure 8, but after 40000 iterations showing the formation of a Karman street. To emphasize the vortices, the mean momentum has been subtracted from the local ones.

was 0.2 (Mach number = 0.3) to control the compressibility effects and spurious terms in the momentum conservation equation. At the downstream edge the outgoing populations are multiplied by a factor smaller than 1 and bounced back, to simulate the effect of a porous wall with pores open to vacuum (the reduction factor assures a uniform flow equal to the one injected upstream). On the lateral edges of the domain, were applied periodic conditions. On the points on the polygonal approximating the surface of the body, were used the bounce-back conditions.

In the first stage of simulations acoustic waves were developed but after a transient period of 8-10 residence time D/U (D is the cylinder diameter and U is the free-stream velocity) the recirculation regions attained the steady state (Figure 10).

The agreement with other numerical methods and experimental values was good in the range of $Re \approx 40$, and the discrepancies found for high Reynolds numbers are due to the moderate size of the computational domain.

The same problem has been treated in three dimensions by Frisch et al. (1988) using a 4-D FCHC lattice (see figure 11). The initial and boundary conditions are roughly a 3D transposition of those used in the 2D simulations of flow past a plate. The lattice size was $128 \times 128 \times 256$, with periodic conditions in the directions transverse to the upstream flow.

Figure 11 gives an image of the 3D perspective view of high-vorticity modulus regions, displaying a "basket and handle" structure.

3. 3. Channel flow in expanded geometry

Another well-known flow situation is that of two-dimensional backward facing step at low Reynolds number (figure 12). Here was used a lattice of size 4608×512 with an inlet part of length 512 and width 256 (Noullez et al. 1986, d'Humieres and Lallemand 1990).

The lateral boundaries of the channel and of the backward facing step are set with the stick condition. At the inlet was used the wind-tunnel condition with injection of particles distributed with uniform density and a parabolic velocity profile. The experiments were done at 50, 100 and 150 Reynolds numbers (the adjustment of the Reynolds number is done either by changing the velocity or the density, due to the dependence of $g(\rho)$ vs. ρ).

After the system reaches the steady state a recirculation zone was observed behind the step (as was observed experimentally) and the location of the reattachment point was computed (see figure 12b). The density of gas was computed and found to vary by less than 3% over the entire lattice, indicating that the flow is essentially incompressible.

As can be seen from figure 10, a good agreement with the behavior of real fluids was obtained, for different Reynolds numbers.

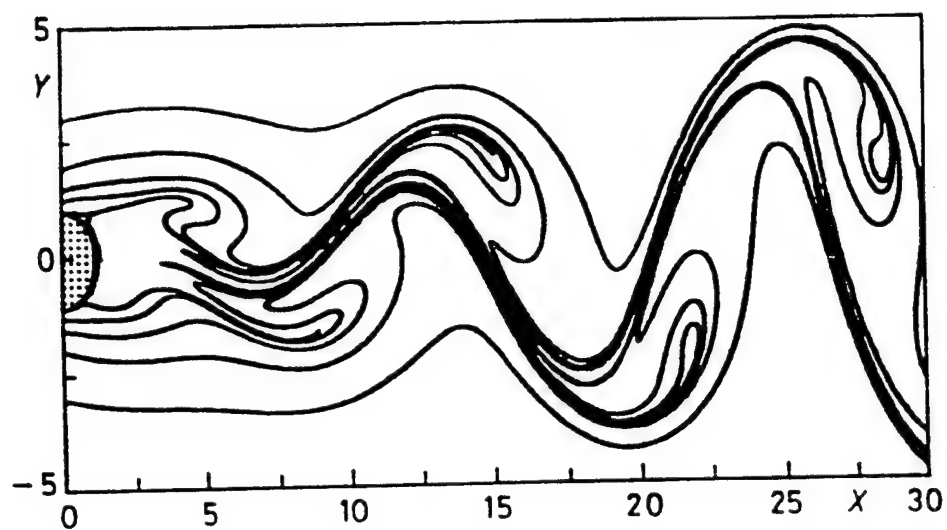


FIGURE 10. Streaklines of the far-field at $Re = 52.8$ two shedding cycles after the transient. The elliptical shape of the cylinder is due to different scales along the horizontal and vertical axes.

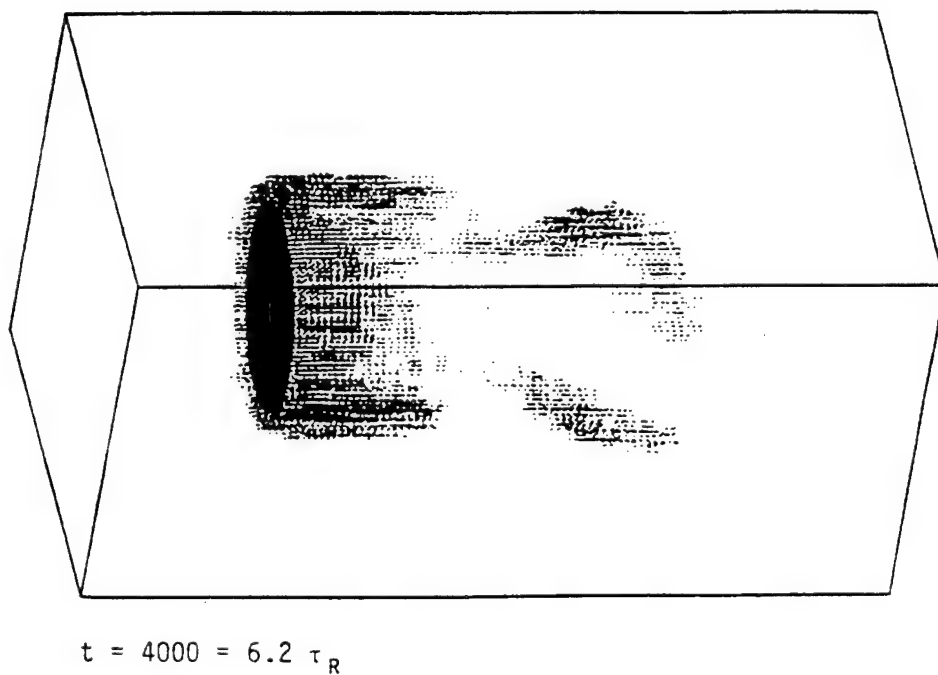
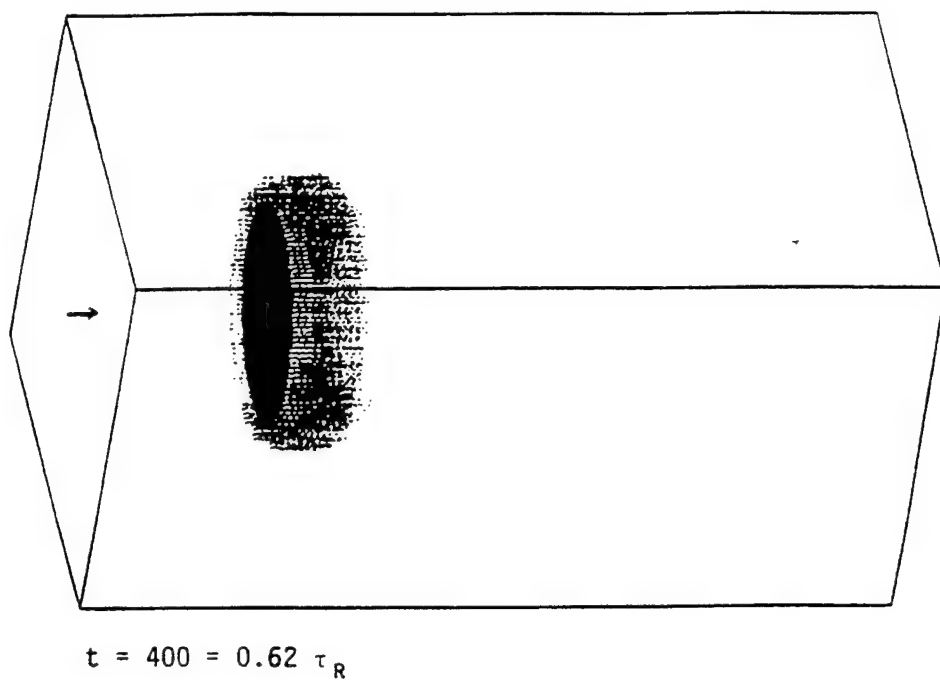


FIGURE 11. Perspective view of the high vorticity regions developed at $Re = 190$ in a 3-D flow passed a circular plate (shown in black) (Rivet, Hénon, Frisch, and d'Humieres, 1988).

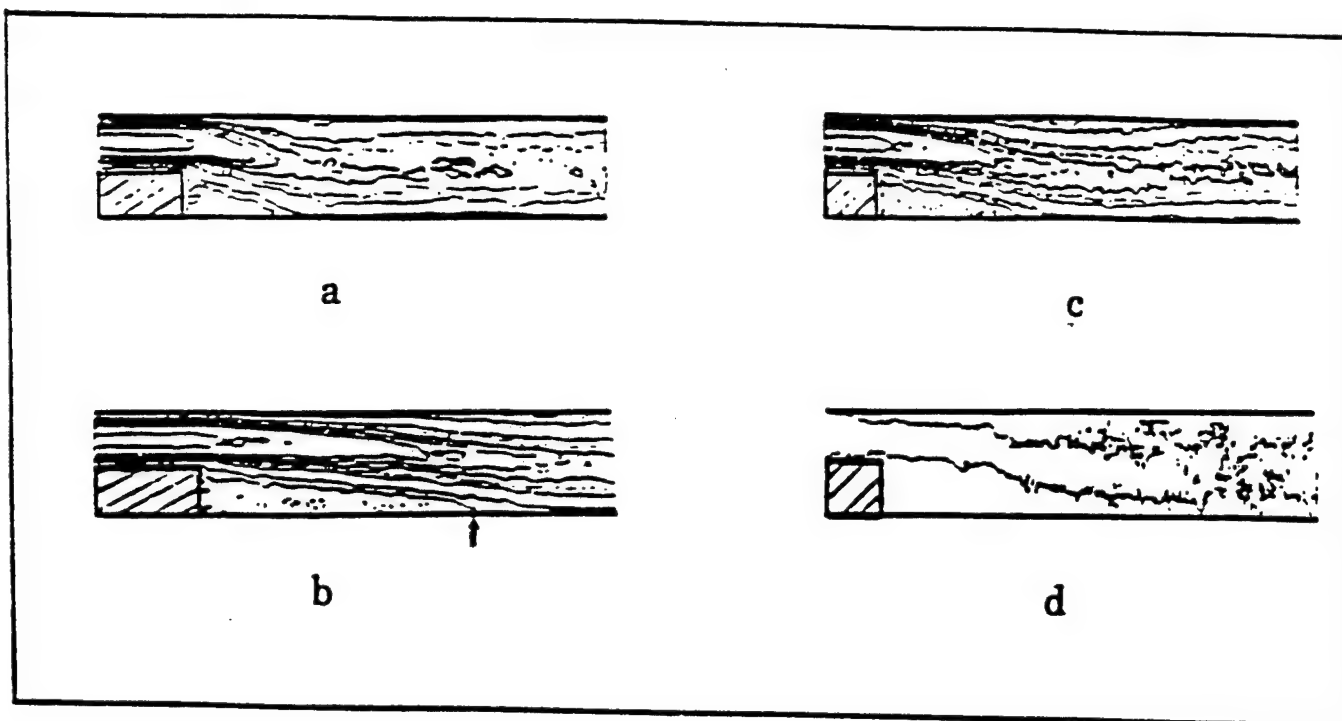


FIGURE 12. Channel flow with sudden expansion. Isomach curves for velocity component along the average input flow direction at $Re = 50$ (a) and $Re = 150$ (b,c); $\Delta u = 10\%$. Isodensity curves (at $\rho = .95 \rho_{max}$) at $Re = 150$ (d). (Note 2x expanded spatial scale in c and d.) Arrow (in b) indicates reattachment point (Noullez, Lallemand, and d'Humieres, 1986).

3.4. Free boundaries flow

The lattice-gas models proved to be extremely appropriate to study mixture of fluids (miscible or immiscible) and an example in that respect is the simulation of the Rayleigh-Taylor instability (see Figure 13, a heavy fluid penetrates a lighter fluid layer) and Kelvin-Helmholtz instability (see Figure 14, two fluid layers moving in opposite directions with respect to each other, develop, by shear constraint, a roll up at the interface).

The Rayleigh-Taylor instability was simulated on a 512×512 lattice, initially set up without overall motion, between two rigid horizontal plates.

At the initial time, a gravity potential is applied in a such a way that the initial state become unstable, and depending on the initial form of the interface, an instability develops in time.

If the interface is planar, a distortion will evolve, which shape depends on the initial microscopic conditions. If the interface is sinusoidal, the distortion amplitude increases exponentially (periodic boundary conditions is assumed in the horizontal direction) and after some time they are no longer harmonic, and the typical shapes are observed (figure 13).

The Kelvin-Helmholtz instability (Clavin et al. 1990), was simulated between two parallel plates of length 1024, separated by 256 lattice sites, set as channel boundaries (assumed to be periodic in the direction of the plates).

Stick conditions are implemented at the boundaries and the initial conditions set a half of the channel with A particles with $+u$ velocity (parallel to the plates) and the other half with B particles with $-u$ velocity (see Figure 14). In time, an instability is developed and A particles are advected by the flow into the B zone.

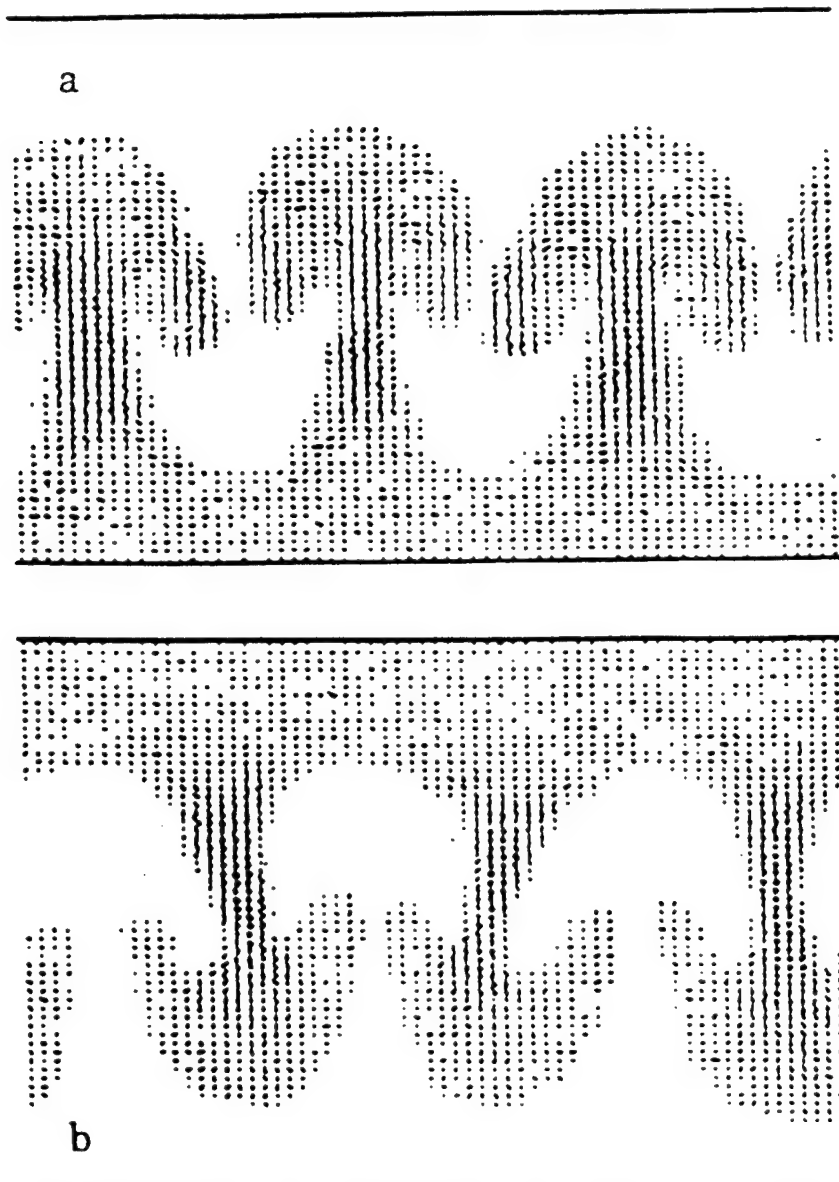


FIGURE 13. 2-D lattice gas simulation of the Rayleigh-Taylor instability. Maps of A-particle flux (a) and of B-particle flux (b) after $t = 1600$ (Clavin, d'Humieres, Lallemand, and Pomeau, 1986).

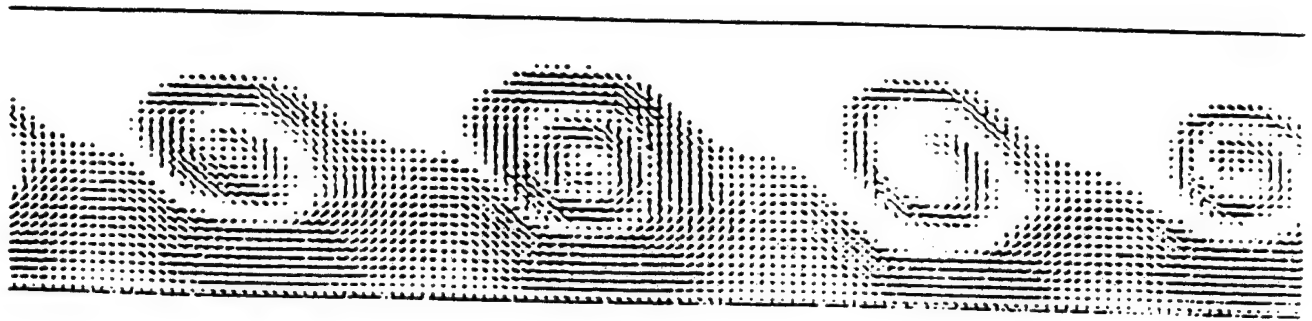


FIGURE 14. 2-D lattice gas simulation of the Kelvin-Helmholtz instability. Average velocities are $+u$ (left to right) and $-u$ (right to left) in lower half and in upper half of channel respectively. Map shows flux of particles of one species (d'Humieres, Lallemand, and Searby, 1987).

4. Applications

4. 1. Flow through porous media

The lattice-gas models are particularly efficient in complex geometry's as it is the case of the flow through porous media. The lattice-gas models, due to their flexibility in dealing with complex boundary conditions, and due to their intrinsic particle tracking techniques, can easily manage the intricacies associated with flow in complex geometries.

The first lattice-gas simulations of flows in porous media were performed with 2D FHP model (Rothman and Keller 1988) and this pioneering work was subsequently extended to 3D, using either the FCHC (Rivet et al. 1991) either the lattice-gas Boltzmann method (Gunstensen and Rothman 1991, Benzi et al. 1992).

The porous medium (either in 2D or 3D) is modeled as a random sequence of elementary blocks, of at least four lattice units wide. The distribution is such that no pore with cross section narrower than a 4×4 lattice units could be found (the minimal size of pore could be found by running preliminary tests to ascertain under which parameter conditions - Re , Mach number and pore size h - the model reproduces the Poiseuille flow in a square-section of the pore channel).

The pore size has to be as small as possible in order to have a large granularity of the porous medium, and in the same time it cannot be too small, because otherwise gradients of the order of the pore size develop and would impair the convergence of the lattice-Boltzmann equation to the Navier-Stokes equations (see figure 15).

Here again the possibility to "tune" the particle mean free path turns to be very important in order to improve the convergence to hydrodynamics at small scales.

In general, the emphasis is on the empirical investigation of the dependence of bulk properties of flow on aspects of microscopic disorder: assess the parameter range in which Darcy's law is fulfilled, and measure the permeability of the medium.

4. 1. 1. Immiscible multi-phase flow through porous media

There are two basic approaches to the simulation of multiphase flow through porous media. The first is to make some simplifying assumptions about the flow, such a linear force-flux law (e.g. Darcy type), and also about the geometric properties of the porous medium (e.g. a network of pores and throats). The second simulates the hydrodynamics of the immiscible fluids through a microscopic model of the porous medium, without any restrictive assumptions about the flow (Rothman and Keller 1988, Gunstensen and Rothman 1992).

The lattice-gas model of immiscible fluids (ILG) is based on the Lattice-Boltzmann method in which a new parameter was introduced to account for the type of fluid: "the color".

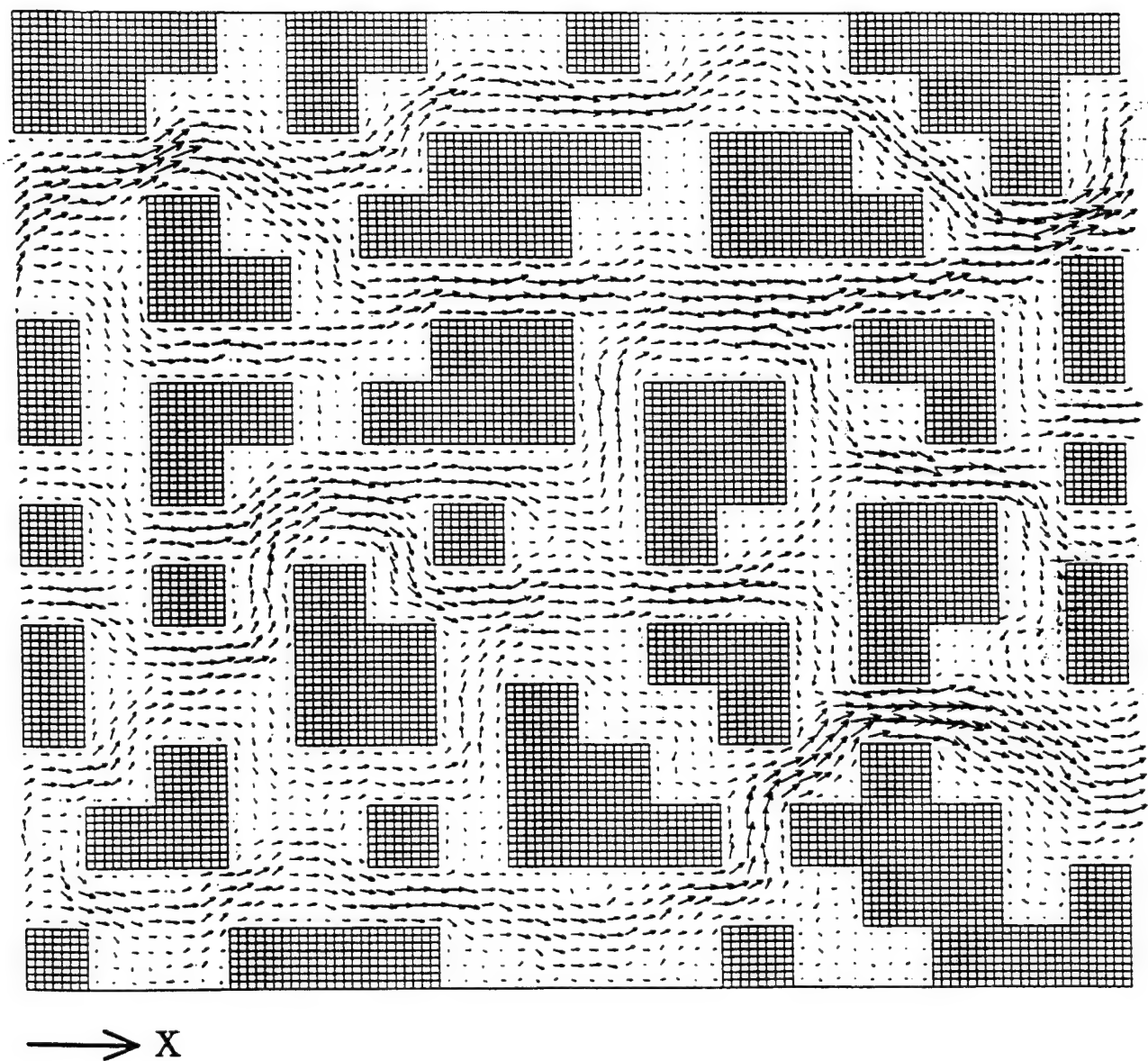


FIGURE 15. Lattice-gas simulation of flow through a two-dimensional porous medium (Rothman, 1988). The fluid is forced from left to right.

The particles are colored either red or blue (or other color if there are more than two phases) and the usual collision operator is altered to obtain the correct interfacial dynamics between phases.

No-slip boundary conditions at the solid-fluid boundaries and the appropriate surface tension boundary conditions are imposed at the fluid-fluid interfaces.

The particle configuration at a site is described by the variables $r = \{r_i, i = 1, \dots, 6\}$ for the red particles, and $b = \{b_i, i = 1, \dots, 6\}$ for the blue particles. The evolution of the particles is as usual: first particles are moving to the nearest-neighbor sites with velocity c_i , but in the collision step, it is conserved not only the total number and momentum of particles, but also the "color"!

To achieve the surface tension, the configuration resulting from a collision depends on the configurations at the nearest-neighbor sites of the lattice. To simulate attraction between the particles of like color, those collisions that send red particles in the direction where the neighbors contain a relative majority of red particles are favored, while blue particles are sent toward neighboring blue particles.

Two new vector fields are defined: the color flux and the color field, respectively:

$$q[r(x), b(x)] = \sum_i c_i [r_i(x) - b_i(x)] \quad (133)$$

$$f(x) = \sum_i c_i \sum_j c_j [r_j(x + c_i) - b_j(x + c_i)]$$

The particle configuration that results from collision is then that configuration which maximizes the product $(f \cdot q)$ such that the number of reds, the number of blues and total momentum are conserved (Rothman and Zaleski 1989). By these rules, the adherence of the original lattice (un-colored LB method) to the Navier-Stokes equations applies equally well to single-color regions of ILG (Rothman and Keller 1988, Succi et al 1989).

The porous medium used in the 2D simulations of immiscible fluids was constructed by placing solid squares of random size on the lattice. The length of the square's side is uniformly distributed between 16 and 8 lattice units when they are placed on the 128 x 128 lattice used in simulations.

Figure 16 illustrates the case in which a nonwetting fluid (black) is injected into a porous medium filled with a wetting fluid (white). The solid sites are gray, and there are an average a number of 4.9 particles per site (both fluids have the same viscosity).

When the capillary number ($Ca = \mu u / \sigma$, the ratio of viscous forces to surface tension) $Ca \ll 1$, capillarity dominates the flow, causing the invading nonwetting fluid to follow the path in which the critical capillary pressure is the smallest (in figure 16, $Ca \approx 10^{-2}$ small enough that the nonwetting fluid is unable to penetrate the narrowest channels).

Figure 17, illustrates the opposite case, in which the wetting fluid (black) invades the same porous medium now initially occupied by the nonwetting fluid. In the same conditions as in

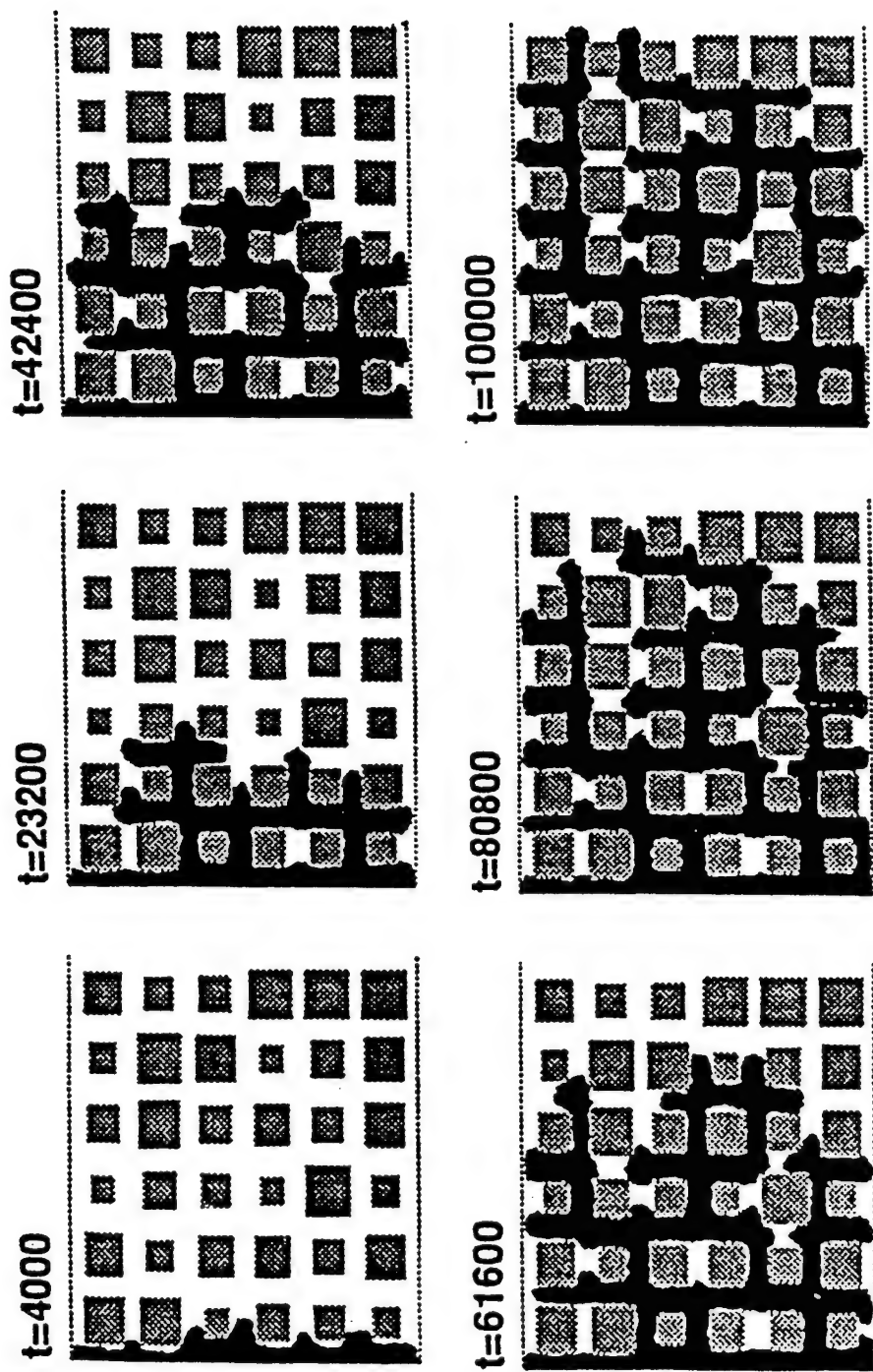


FIGURE 16. Two-phase flow in a 2-D model of a porous medium. The invading nonwetting fluid is colored black and the solid areas are grey. The capillary number is approximately 10^{-2} . Time t is given in time steps.

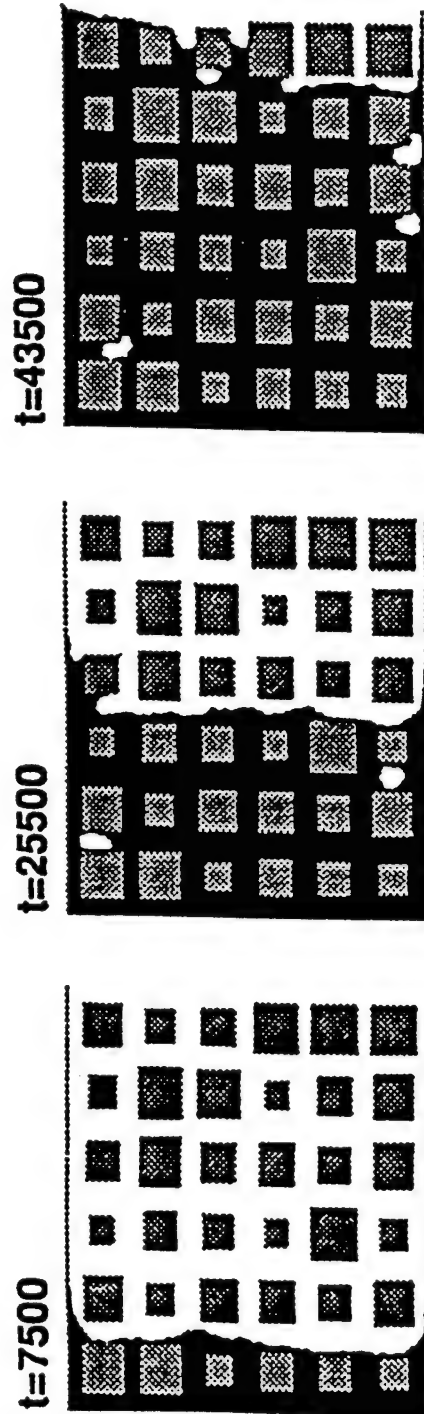


FIGURE 17. Two-phase flow in a 2-D model of a porous medium. In contrast to Figure 16 the invading fluid (black) now wets the grey solid. Note the smoothness of the invasion front as compared to the previous example.

the previous experiment, the wetting fluid fills the porous medium relatively quickly, and comparatively smoothly without appearance of the capillary fingers as in Figure 16.

Some other coloring schemes were proposed, for the spinodal decomposition in porous media, based on the LB method (Cyeplak et al. 1992, d'Ortona et al. 1994, Rybka et al. 1995).

This approach, use the "coloring scheme" way of the ILG but with a drastic change of the re-coloring algorithm (Cyeplak et al. 1992, d'Ortona et al. 1994, Rybka et al. 1995). As the phase separation in porous media, due to the spinodal decomposition, depends crucially on the way the surface tension effects are implemented, the new re-coloring scheme allows for a more flexible control of the interfaces in the kinetic model.

The surface tension is controlled by two microscopic parameters, one determining the magnitude of the jump in the density and the other the thickness of the interface. More, the LB model is not liniarized around the equilibrium and is Galilean-invariant.

The recoloring scheme is defined by the equations:

$$\begin{aligned} r'_i(\mathbf{x}) &= \frac{R_t}{R_t + B_t} f_i + \beta_1 \frac{R_t B_t}{(R_t + B_t)^2} \cos \varphi_i \\ b'_i(\mathbf{x}) &= \frac{B_t}{R_t + B_t} f_i - \beta_2 \frac{R_t B_t}{(R_t + B_t)^2} \cos \varphi_i \end{aligned} \quad (134)$$

with:

$$f'_i(x) = f_i + \beta_1 |g| \cos(2\varphi_i)$$

where f_i refers to the initial state of density, f'_i is the density after redistribution, φ_i is the angle with the i -th direction of the lattice links, R_t, B_t refers to the total red and blue densities at a node, and g is the gradient vector at each node. The parameters β_1 and β_2 control the values of the surface tension and interfacial width respectively. They allow to avoid having an abrupt interface whose properties are sensitive to its orientation with respect to the underlying lattice.

The simulation was carried out on a 256 x 256 lattice, the fluid density was 1/3 and the relative content of red particle was 0.5, with Re between 3 and 7.

Figure 18 displays the spinodal decomposition for wetting fluid (a) and a neutral fluid (b). For longer times one can see easily the difference in the shape of separated phases. In the wetting case the red fluid sticks to the solid wall and the domains show much greater connectivity. In the neutral case the domains are more spherical and less connected together.

4. 1. 2. Phase separation

There are many difficulties in numerically simulating multi-phase flow or immiscible fluids through porous media, with conventional methods. Usually, the multi-phase flow through porous media is a mixture of water/oil/gas or any other combination of two of them. Phase

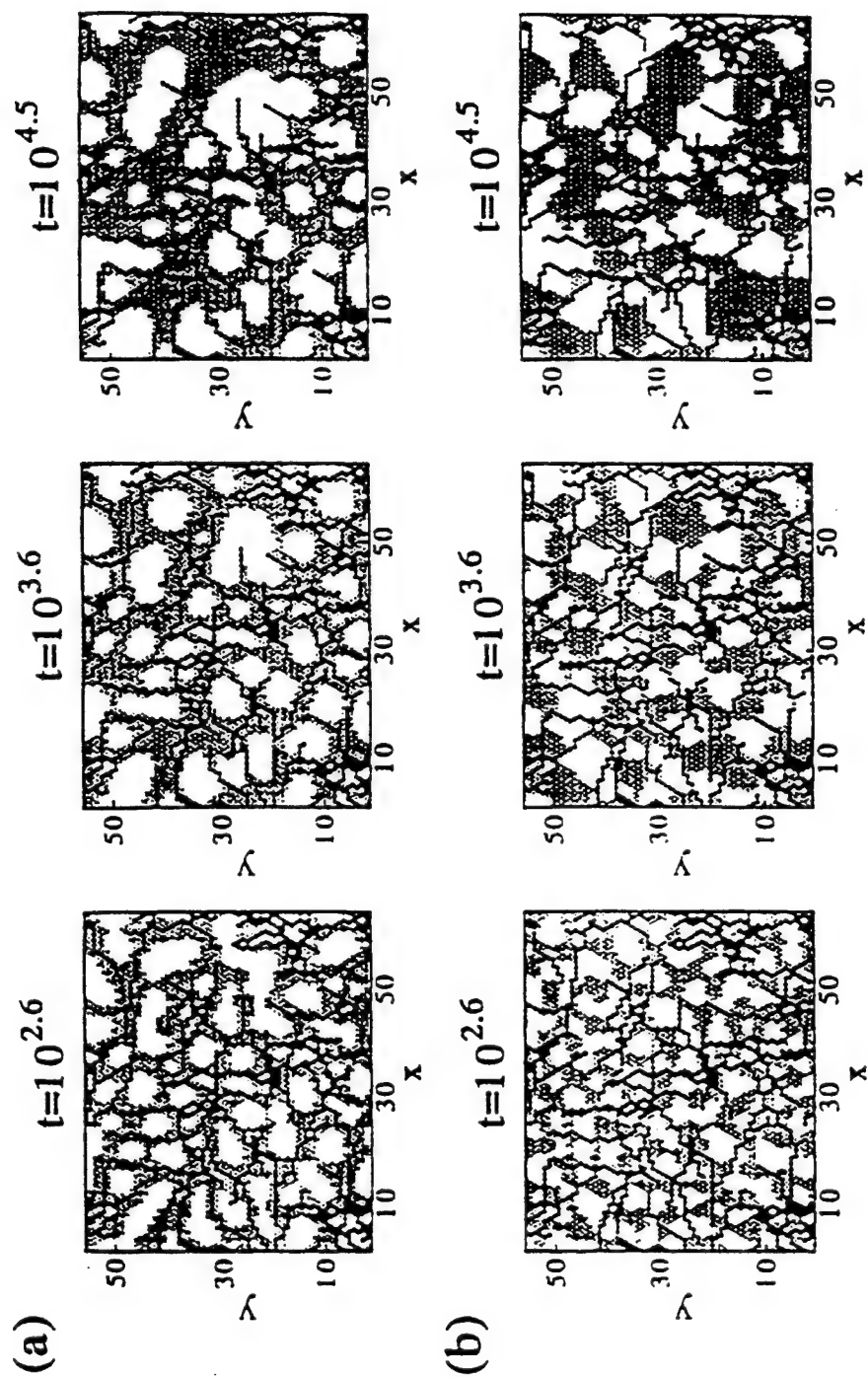


FIGURE 18. The snapshots of the deep quench spinodal decomposition in porous media modelled by random threads. (a) wetting and (b) neutral "solid" nodes.

separation, due to spinodal decomposition, is associated with first order transitions such as liquid-gas transition, fluid separation in binary fluid systems and in binary metallic solutions.

One approach starts from the LB-ILG (Rothman and Keller 1988, Gunstensen et al. 1991) but introducing S total components (on 2D hexagonal lattice or 4D FCHC):

$$N_i^\sigma(\mathbf{x} + \mathbf{c}_i, t+1) - N_i^\sigma(\mathbf{x}, t) = \Delta_i^\sigma(\mathbf{x}, t) \quad (135)$$

$$\sigma = 1, \dots, S \quad a = 0, \dots, b$$

where $N_i^\sigma(\mathbf{x}, t)$ is the single-particle distribution function for the σ component and $\Delta_i^\sigma(\mathbf{x}, t)$ is the collision term. The set of vectors $\{\mathbf{c}_i, i = 1, \dots, b\}$ are the velocities of the particles moving on the lattice links to the one of the b nearest-neighboring sites, each time step ($\mathbf{c}_0 = 0$ is associated with the rest particles).

The collision parameters has the LB-BGK form with the corresponding modification due to the S components:

$$\Delta_i^\sigma(\mathbf{x}, t) = -\frac{1}{\tau_\sigma} [N_i^\sigma(\mathbf{x}, t) - N_i^{\sigma(eq)}(\mathbf{x}, t)] \quad (136)$$

where τ_σ is the mean collision path (Qian et al. 1992, Chen et al. 1992) for the σ -th component and determines its fluid viscosity.

$N_i^{\sigma(eq)}(\mathbf{x}, t)$ is the equilibrium distribution at site \mathbf{x} and time t , with its explicit form chosen as is specific for the LB-BGK models.

In order to simulate multiple components fluids or fluids with non ideal gas equation of state, the nonlocal interactions among particles are incorporated through an interaction potential:

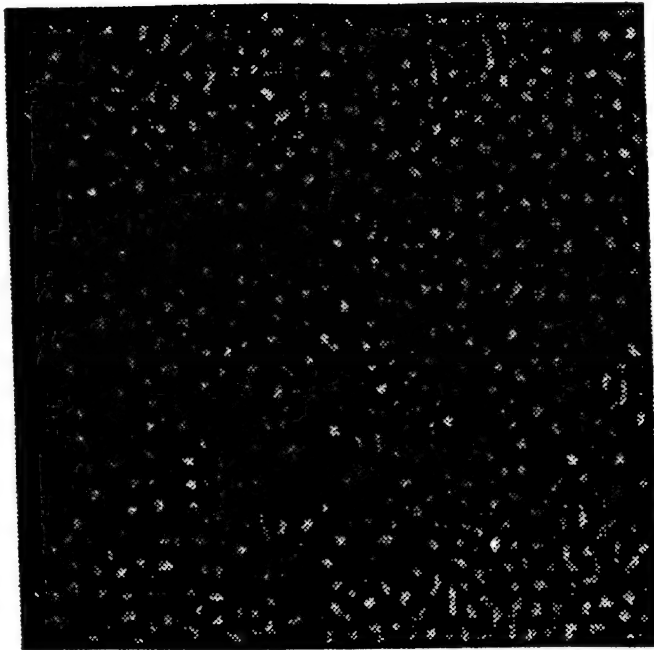
$$V(\mathbf{x}, \mathbf{x}') = G_{\sigma\sigma'}(\mathbf{x}, \mathbf{x}') \Psi^\sigma(\mathbf{x}) \Psi^{\sigma'}(\mathbf{x}') \quad (137)$$

where $G_{\sigma\sigma'}(\mathbf{x}, \mathbf{x}')$ is a Green's function controlling the sign (attractive/repulsive) and the strength of interaction, while $\Psi^\sigma(\mathbf{x})$ plays a role as the effective number density for the component σ .

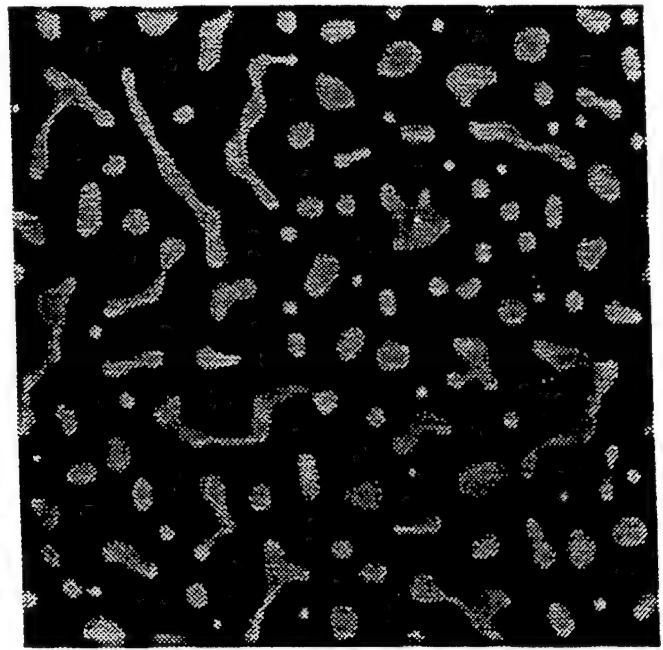
With this interaction potential, the LB-BGK model exhibits thermodynamic phase transitions shown in Figure 19.

The numerical simulation was done on a 2D 256 x 256 hexagonal lattice, with relative density $d = 0.5$. The lattice was initialized with a homogenous density distribution with only 1% random perturbation.

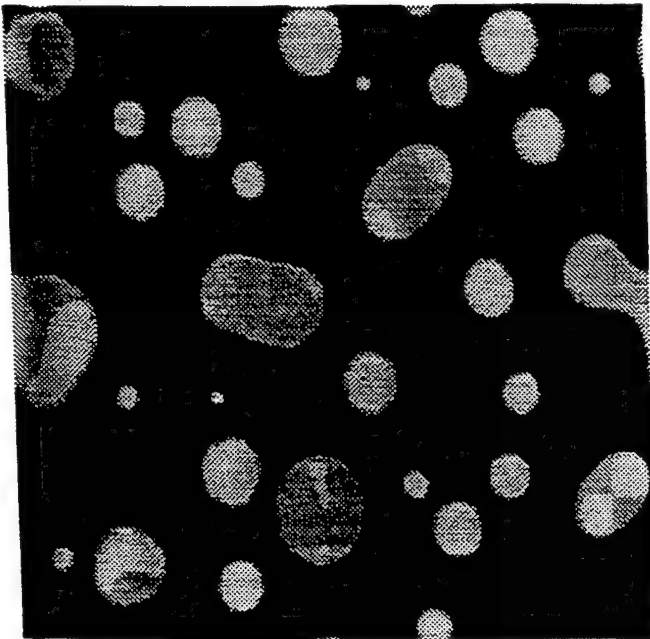
Figure 19 displays, in gray scale, the evolution of the mass density distribution. As G gets below the critical value, the system changes from a single-phase to a two-phase fluid.



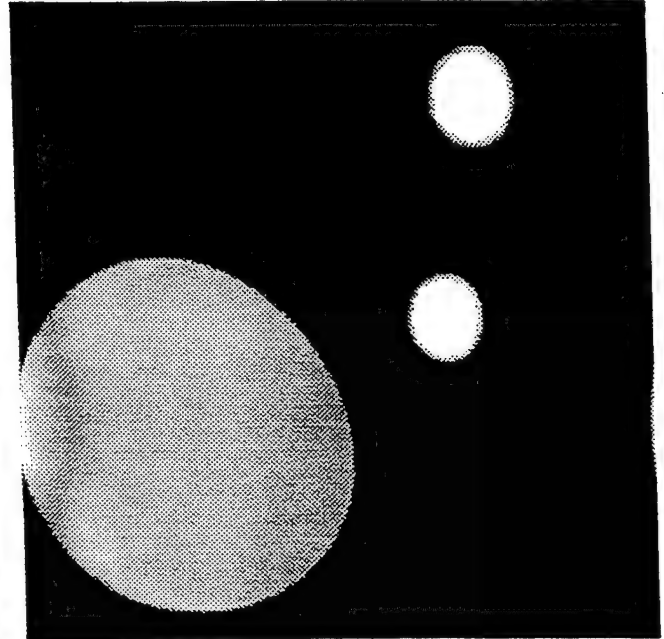
(a)



(b)



(c)



(d)

FIGURE 19. Phase transition in a LB simulation on a 256×256 lattice with a single component. Shown are the time evolution of the number density distribution at $t = 20$ (a), $t = 200$ (b), $t = 2000$ (c), and $t = 20000$ (d). The variation of the density is shown in gray scale with the minimum in black and the maximum in white. Since the lattice is hexagonal, the graphics are distorted by a factor of $\sqrt{3}/2$ in one direction. $G = -0.45$, $\rho_0 = 1$, and $(\rho) = 0.693 \cong \ln 2$.

It can be seen the separation of the different thermodynamics phases and the existence of the surface tension.

4. 1. 3. Viscous fingering

Viscous fingering is a complicate phenomenon which arises as a result of instabilities that occur when a dense viscous fluid, filling a porous material, is forced to be displaced by the local injection of a less viscous fluid.

This instability is analogous to the Saffman-Taylor instability observed in Hele-Shaw cells. In porous media the underlying mechanism is basically two dimensional and so the phenomenon is well suited for lattice-gas investigation.

The porous medium is simulated by a random spatial distribution of static scattering nodes (3% of the total number of nodes) on a 320 x 512 hexagonal lattice. The two fluids are miscible and have a viscosity ratio of 33.

The viscosity difference is set by selecting specific collision rules for each fluid: for the more viscous fluid only 12 efficient collisions are used among the 64, which in turn are all present for the low viscosity fluid.

Particles colliding with the scattering nodes of the porous material undergo bounce-back collisions, yielding momentum dissipation at these nodes. During collisions involving particles of both fluids, the particles are redistributed so as to minimize mutual diffusion, such that the mixing be a slow process on the hydrodynamic scale. Minimizing the diffusion coefficient D one maximizes the Peclet number ($Pe = Ud/D$, where U is the average Darcy's velocity, d is the pore size, and D is the diffusion coefficient, is the ration between rate of transport by convection to the rate of transport by molecular diffusion), which favors the development of large body waves modes.

The lattice was initialized with a slab of low viscosity fluid along the left boundary and with a highly viscous fluid in the rest. At initial time, both fluids are at rest and have the same density. The right edge of the lattice is continuously maintained at this constant density in order to simulate an infinitely extended medium. Periodic boundary conditions are imposed on the upper and lower boundaries. A pressure gradient is set up and maintained by a density gradient oriented to the left, which pushes the less viscous fluid from left to right through the medium.

Viscous penetration then occurs and develops progressively into viscous fingering (Figure 20 and Figure 21) with a characteristic wavelength, the rate of growth being proportional to the porosity of the medium.

The experiments have shown that viscous fingering occurs only if there is a sufficiently large viscosity difference between the two fluids and when there is a density gradient on the less viscous fluid, otherwise the system will exhibit only mutual or forced diffusion.

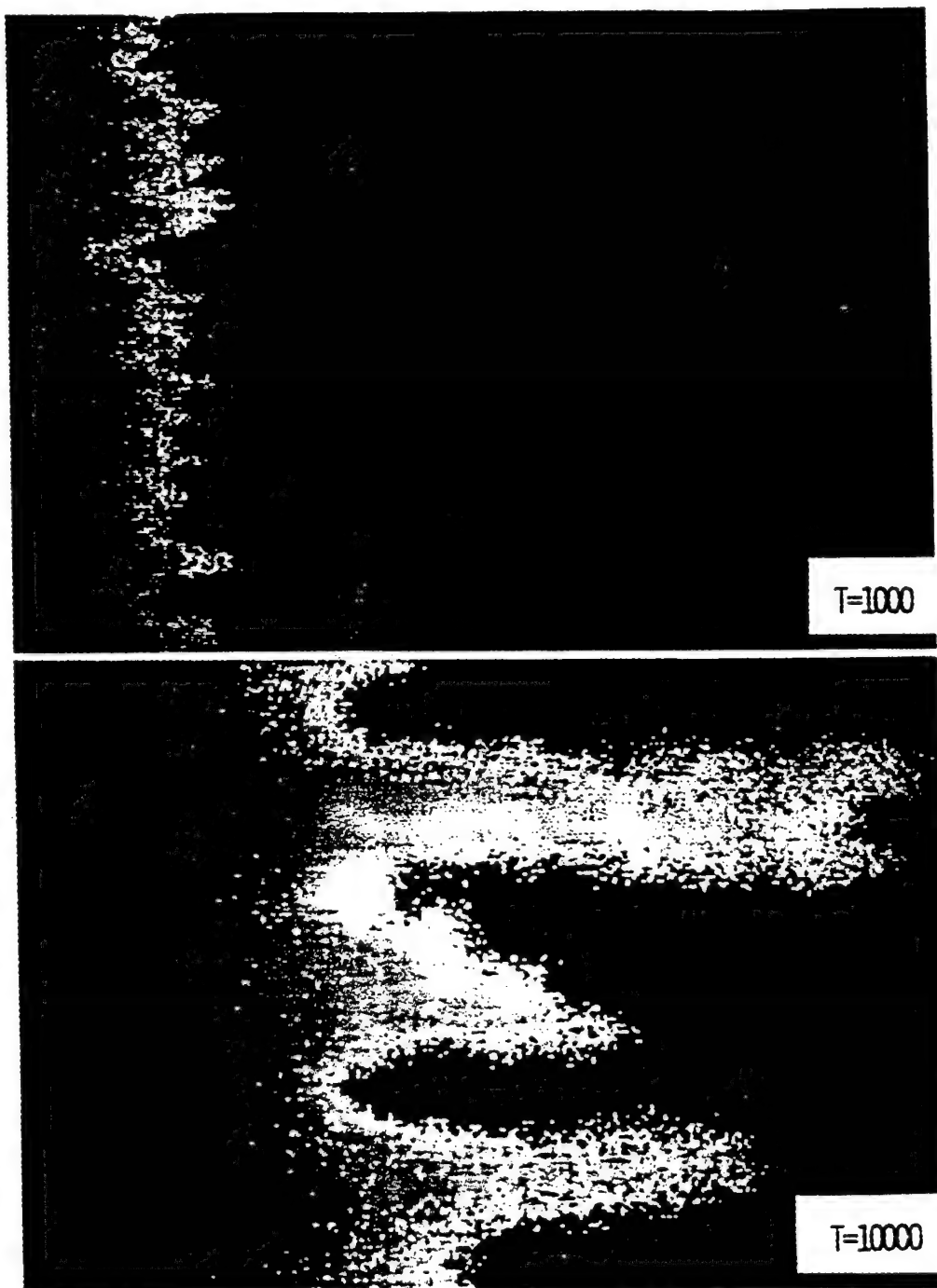


FIGURE 20. Viscous fingering in 2-D porous lattice. Time is given in lattice gas time step units. Notice tip-splitting at $t = 10000$.

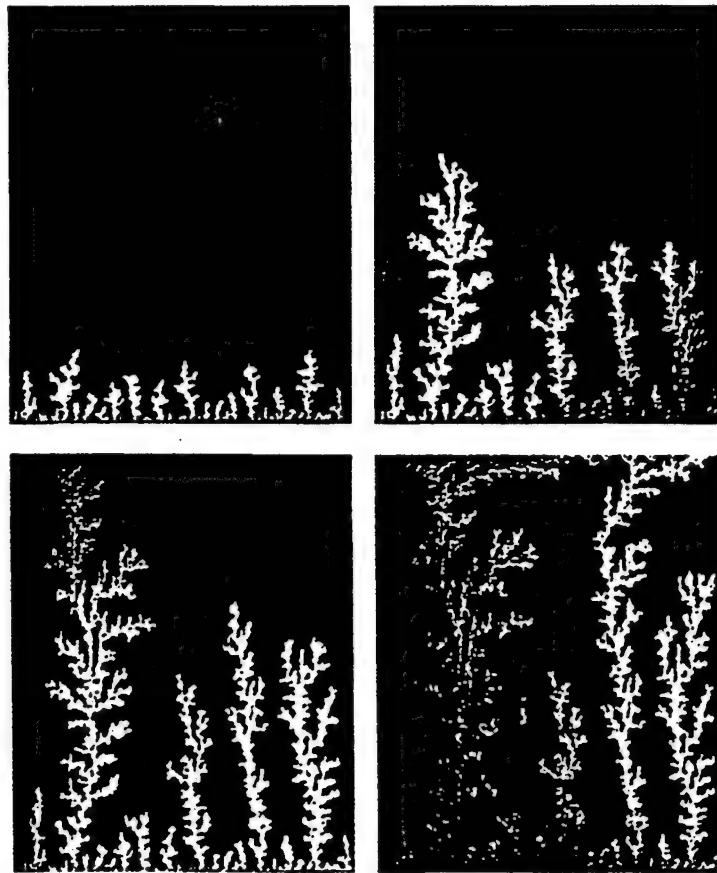


FIGURE 21. Simulation of viscous fingering: a high-mobility fluid (entering from below) displacing a much less mobile fluid (leaving from above). The simulation is done on a 256×256 lattice.

4. 2. Transport of particle suspensions

Simulation of transport of particle suspensions by fluids is of considerable interest for industrial processes, biological liquids, in oil reservoir exploitation, etc. The theoretical description of these systems at particle volume fractions exceeding the dilute limit is considerable complicated by the presence of indirect (hydrodynamic) interactions between the particles. These interactions result from the velocity fields set up in the suspending liquid by the relative motion of solid particles (Landau and Lifshitz 1967). The treatment of these forces is complicated by the fact that they are of many-body and long-ranged nature and therefore the numerical simulations become extremely important of studying the dynamical properties of particle transport. Most simulations algorithms (Brownian dynamics, Stokesian dynamics, the multipole method) are based on the clear time-scale separation that exists between the dynamics of fluid and that of solid particles. This separations implies that the development of the hydrodynamic interactions is instantaneous and therefore they depend on the positions and velocities of all particles. For this reason, all these algorithms scale as the square root or cube of the number of particles.

In the Lattice-Boltzmann/BGK method (Behrend 1995, Ladd 1990, 1991, 1993, 1994a, b) the state of fluid is updated on a regular lattice while the solid particles move continuously in space and interact with the fluid at a set of special lattice nodes. This technique takes advantage of the fact that the hydrodynamic interactions are time dependent and develop from purely local interactions at the solid-liquid interface. Therefore it is not necessary to consider the global system, but one can update one particle at a time. The methods scale linearly with the number of solid particles and therefore allows far larger and more significant simulations than those possible with conventional methods.

The hydrodynamic interactions between solid particles are fully accounted for in the lattice-Boltzmann methods, both at zero and finite Reynolds numbers (Ladd 1994 a, b).

The crucial part of the algorithm is the mechanism of interaction between the solid particles and the fluid, the so-called "boundary rules", implemented at a set of lattice-sites, the "boundary nodes". The analytical developments of the effects of the boundary rules are possible only for simple geometries (such as planar Couette flow) while for more complex boundaries, such in particulate suspensions, the only judge of the quality of a boundary method is the comparison of the results of numerical computation with independent calculations.

The solid particles are defined by a boundary surface, of any size and shape, which cuts some of the links between the lattice nodes (see figure 22) and defines a set of boundary nodes whose positions are \mathbf{r}_b . At each update of the lattice a special rule at the boundary nodes is implemented on the distribution functions n_i . This boundary rule exchange momentum between the fluid and the particle (the total momentum being conserved) and enforces a stick boundary conditions on the fluid. Therefore the fluid velocity at the boundary nodes is matched to the local

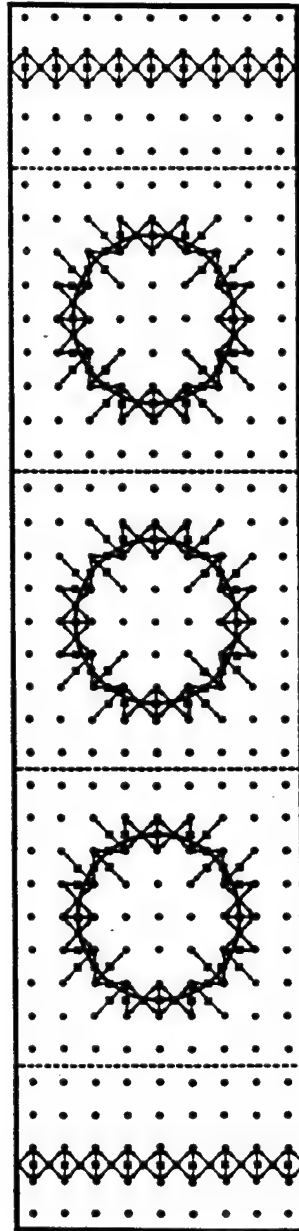


FIGURE 22. Geometry for quasi-periodic simulations. The figure illustrates a system that closely approximates a periodic one under an external flow. The lattice nodes are shown by solid circles and the boundary nodes by solid squares. The arrows indicate velocity directions c_i and c'_i at the boundary nodes. Periodic boundary conditions are applied across the planes indicated by solid lines; the configuration of solid particles within the quasi-periodic unit cells (bounded by dashed lines) are identical. Macroscopic flows can be set up by the planes of boundary nodes at either end of the system. With this geometry we can set up uniform flow perpendicular to the boundary walls or an approximately linear shear flow parallel to the boundary walls. The properties of the central cell are close to those of a truly periodic system; it is not necessary, apparently, to include more cells, although this can be done if required.

solid-body velocity \mathbf{u}_b and is determined by the solid-particle velocity \mathbf{U} , its angular velocity $\boldsymbol{\Omega}$, and the position of its center of mass \mathbf{R} (Behrend 1995):

$$\mathbf{u}_b = \mathbf{U} + \boldsymbol{\Omega} \times (\mathbf{r}_b - \mathbf{R}) \quad (138)$$

The momentum density exchange causes a local force density to be exerted on the particle at node \mathbf{r}_b , $\mathbf{f}(\mathbf{r}_b)$. The total force and torque on the particle are obtained by summing $\mathbf{f}(\mathbf{r}_b)$ and $(\mathbf{r}_b - \mathbf{R}) \times \mathbf{f}(\mathbf{r}_b)$ over all boundary nodes associated with the particle. These forces and torque are used to update the position and velocities of the particle according to the laws of Newtonian mechanics, using pre-assigned mass and moment of inertia.

As a test was computed the drag forces between the solid particles. The simulations comprise a periodic unit cell, $2L \times L \times L$, with spheres located at $(L \pm 1/2 L, 1/2 L, 1/2 L)$. The two spheres move with opposite velocities \mathbf{u} and $-\mathbf{u}$ (thus there is no momentum flux).

For all velocities the drag force was found to be linear and superposable function of \mathbf{u} . In Figure 23 the simulation results are compared with integral-equation solutions for an identical geometry, including an exact calculation of the lubrication forces. The overall agreement is good, the simulation being accurate for particle separation of 1 lattice space. Further on, the hydrodynamic transport coefficients of equilibrium distributions were calculated (Ladd 1994a, b). Have been computed the permeability of fixed random arrays of spheres (K), the collective mobility or sedimentation velocity (μ), the short-time self-diffusion coefficient (D_s) and the high-frequency viscosity (η_∞). In Figure 24 the results from the Lattice-Boltzmann method simulations are compared with independent calculations, based on multipole moment expansions of the Oseen equation. The results when corrected for finite-size effects are in excellent agreement with experiment.

The self-diffusion coefficient D_s was also computed from the average mean-square displacement or from the velocity auto correlation function. Figure 25 gives the ratio D_s/D_0 for various volume fractions and particle sizes. The agreement is quite good but compared with the steady non-equilibrium flows (figure 24) larger particles are required at higher densities for the same accuracy. These discrepancies could come from the effects of insufficient shared boundary nodes, because for larger spheres the agreement is good. Also the results for the collective mobility are reported in Figure 25 and the agreement is quite good.

These results as well as other reported recently (Behrend 1995) show that the lattice Boltzmann method as well as lattice Boltzmann-BGK is a viable technique for quantitative simulations of hydrodynamically interacting particles. Even using small solid particles, with radii less than 5 lattice spacing, accurate results for hydrodynamic transport coefficients (permeability, sedimentation velocity, self-diffusion coefficient and viscosity) have been obtained over a whole range of packing fractions.

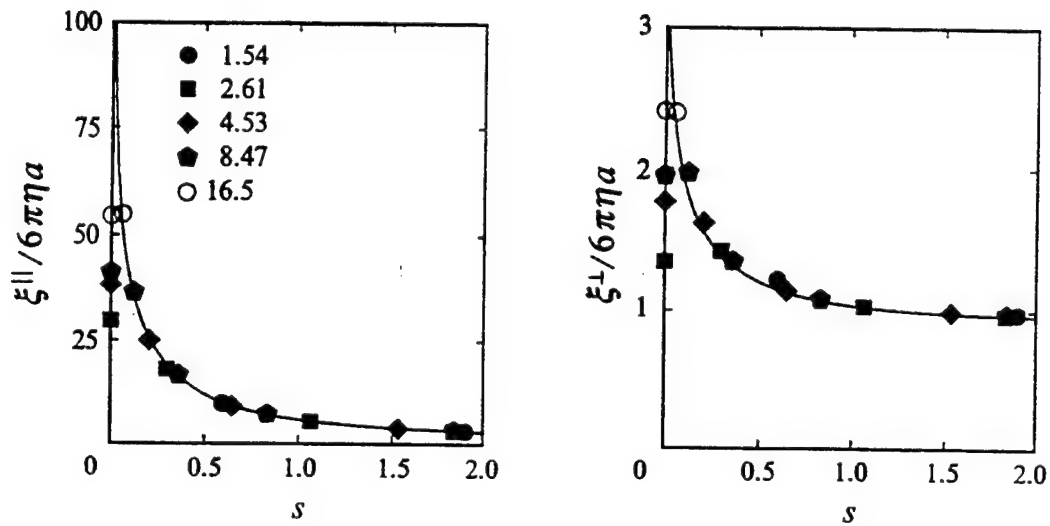


FIGURE 23. Hydrodynamic interactions between pairs of spheres. The parallel and perpendicular friction coefficients are plotted as a function of $s = R/a - 2$. The results at $s = 0$ are for objects in closest possible proximity. The systems are periodic, with a two-sphere unit cell. The solid lines are again solutions of the Stokes equations in the same periodic geometry.

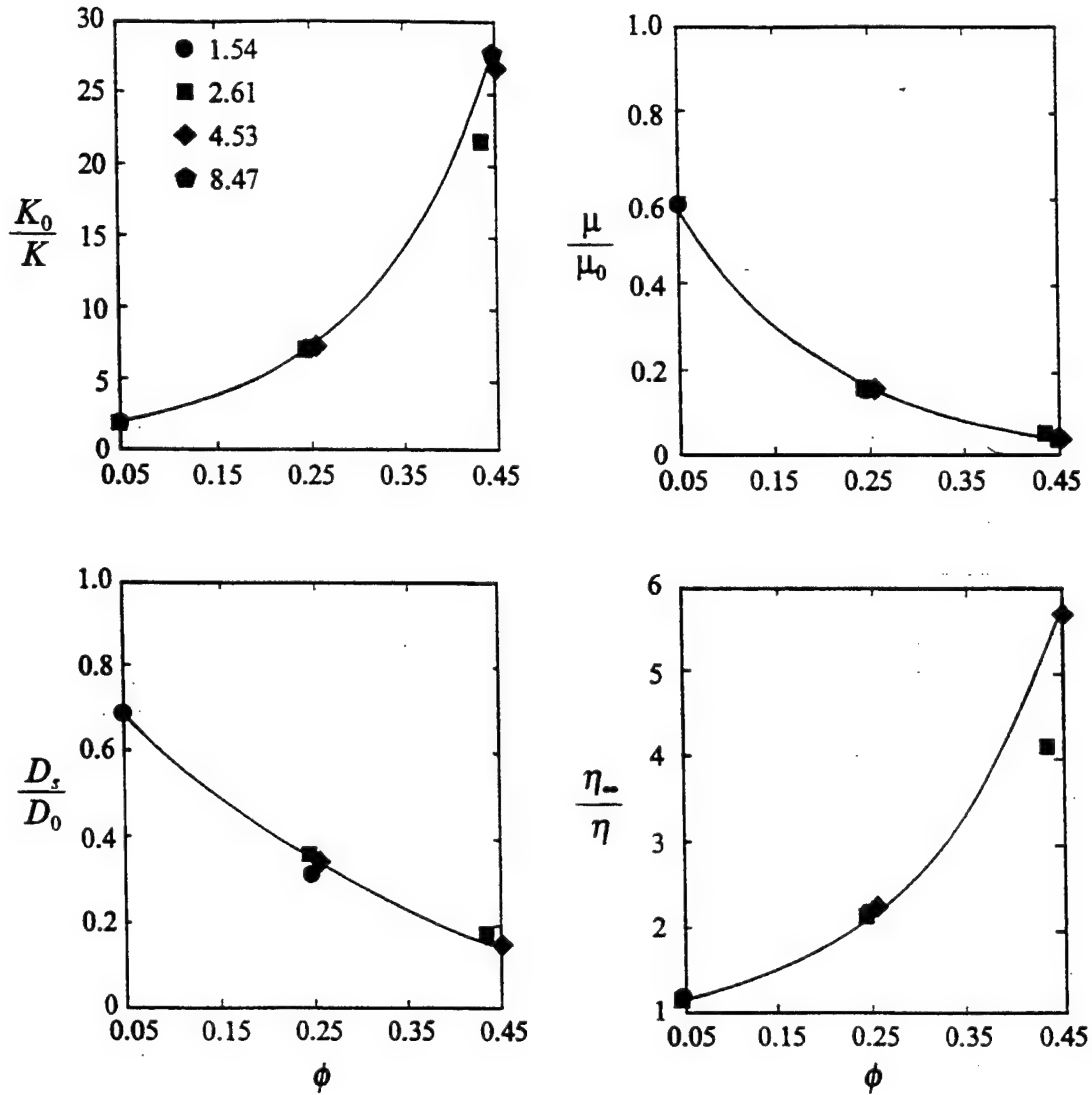


FIGURE 24. Hydrodynamic transport coefficients of random arrays of spheres. Results from simulations of 16 spheres (with periodic boundary conditions) are compared with accurate numerical solutions of the Stokes equations (Ladd, 1990). The lattice-Boltzmann results (present work) are plotted as symbols; results from Ladd (1990) are shown as solid lines. The statistical errors in both sets of calculations are smaller than the plotting symbols.

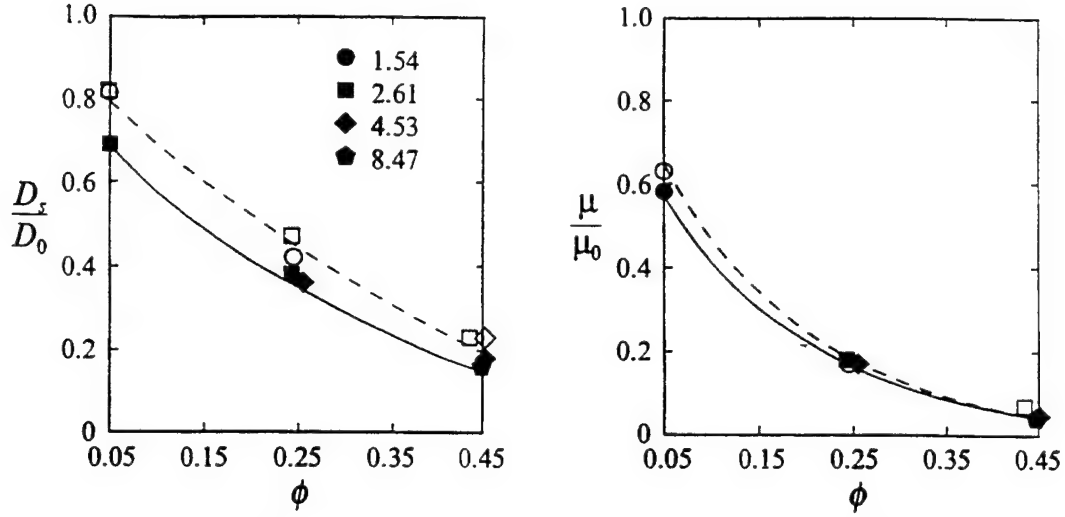


FIGURE 25. Diffusion coefficients of random arrays of spheres. Self-diffusion coefficient D_s and collective mobility μ from simulations of 16 spheres (filled symbols) and 128 spheres (open symbols) are compared with numerical solutions of the Stokes equations (Ladd, 1990). Results from moment expansions of the Oseen equation are shown as solid lines ($N = 16$) and dashed lines ($N = 128$). The statistical errors in the fluctuating lattice-Boltzmann simulations are comparable to the size of the plotting symbols.

4. 3. Free boundary flows

The Lattice-Boltzmann methods was extended by a reservoir of rest particles to model the flow and pressure distribution in a lid-driven cavity at high Reynolds numbers.

By introducing a reservoir of rest particles with a density d_0 , the dependence of pressure p on velocity u can be removed (Chen et al 1992). The total density of the system is then given by:

$$\rho = d_0 + M_c d \quad (139)$$

with d of moving particles per node and with the usual LB-BGK equations changing accordingly (Miller 1995, Eggels 1995).

The lattice size was 150 x 150 mesh points was used to study the flow in a cavity with different types of boundary conditions (uniform and non uniform Dirichlet, uniform and non uniform Neumann).

For Reynolds number around 1000 and a uniform shear flow applied at the top of the lattice, two strong vortices are formed on the right-hand side of the cavity (Figure 26). For the case with the non uniform shear flow, only one strong vortices are formed at the right hand side, due to a high pressure zone formation at the end of the cavity.

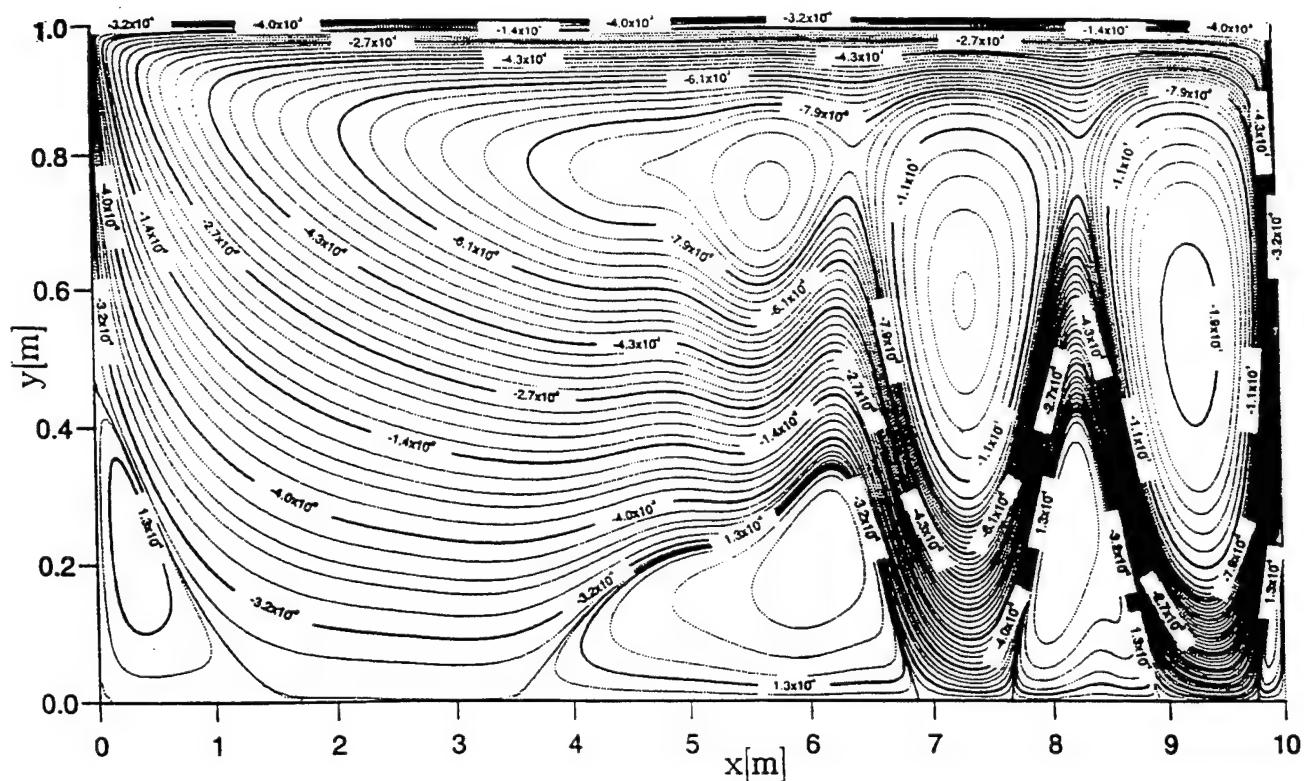


FIGURE 26. Streamlines for $Re = 1000$, aspect ratio $A = 10$, and the uniform Dirichlet boundary condition at the top.

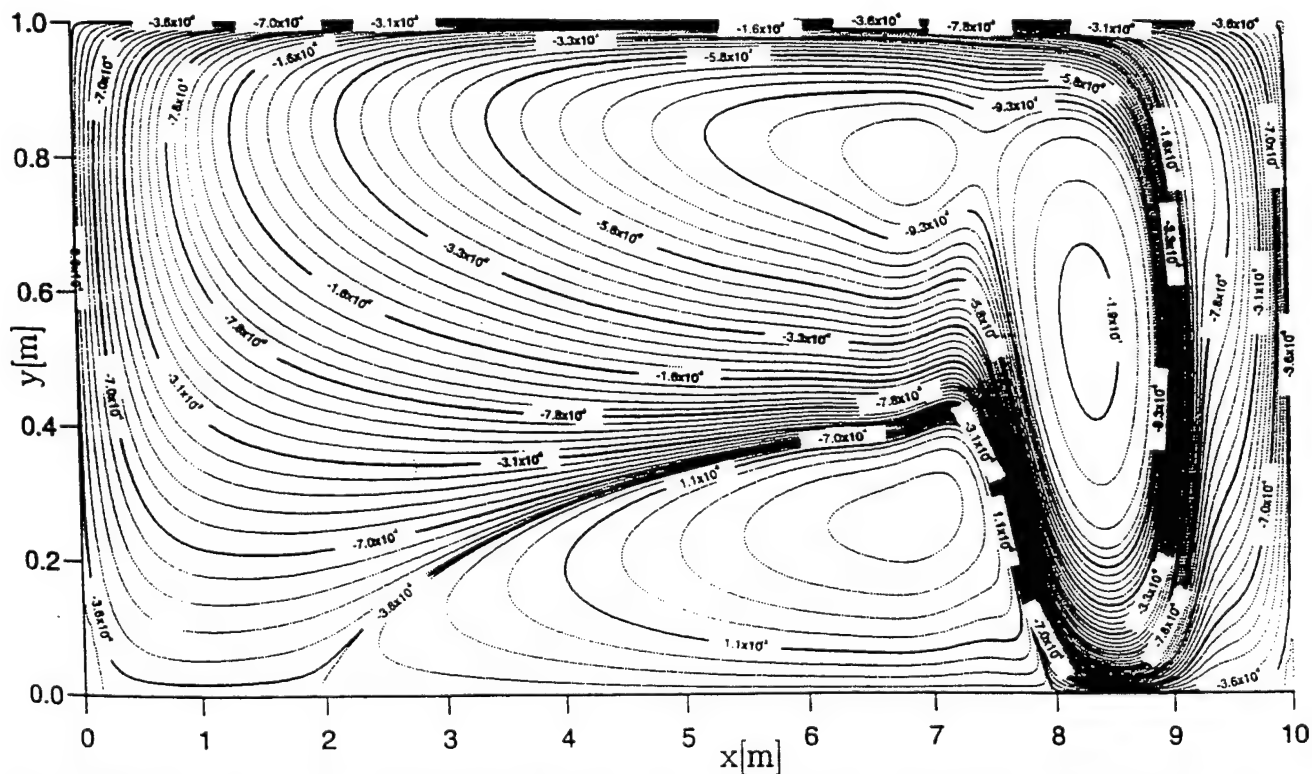


FIGURE 27. Streamlines for $Re = 1000$, aspect ratio $A = 10$, and the nonuniform Dirichlet boundary condition at the top.

5. Conclusions

The lattice-gas models (assuming identical particles that hop from site to site on a regular triangular lattice and obeying simple collision rules that conserve mass and momentum) demonstrated that the full details of real molecular dynamics are not necessary to create a microscopic model with a macroscopic hydrodynamic behavior.

Further on, the LGA became an alternative means for the numerical simulation of hydrodynamic flows and gave rise to new ideas for constructing models of complex fluids: fluid mixture including interfaces, exhibiting phase transitions or multi-phase flows through porous media, etc.

The main advantages of LGA's techniques are: intrinsic stability, easy introduction of boundary conditions and therefore a great facility to deal with complex geometries, simple numerical codes and an intrinsic parallel structure allowing an efficient parallel implementation.

The early drawbacks of the LGA models: statistical noise (and therefore the need for spatial/time averaging), not-Galilean invariant, (the presence of the $g(\rho)$ factor in the nonlinear advection term of the Navier-Stokes equations), the velocity-dependent pressure and the presence of the spurious invariants, have been cured by the recent developments of the Lattice-Boltzmann and the Lattice-Boltzmann BGK method.

The LGA techniques, while developed initially for the fluid hydrodynamics, proved to be applicable to a wide range of phenomena through a proper choice of the equilibrium distribution function (the actual choice being just an example which is suitable for the recovering of the Navier-Stokes equations): reaction-diffusion systems, crystal growth, heterogeneous chemical reactions, diffusion, wave propagation, and magneto-hydrodynamics.

SELECTED REFERENCES

Lattice-gas

F. J. Alexander, I. Edrei, P.L. Garrido, J. L. Lebowitz (1992) Phase transitions in a probabilistic cellular automaton: growth kinetics and critical properties. *J. Stat. Phys.* vol. 68, nos. 3/4, pp. 497-514.

C. Appert, D. Rothman, S. Zaleski (1991) A liquid-gas model on a lattice. *Physica D*, vol. 47, pp.85-96.

C. Appert (1993) Gas-liquid dynamical phase-change and interface generation on lattice gases. Phd. Thesis, Ecole Normale Sup., Univ. Paris 6, Paris. (in french).

G. K. Batchelor (1967) An introduction to fluid dynamics. Cambridge Univ. Press, NY.

D. Bernardin, O. E. Sero-Guillaume, C. H. Sun (1991) Multispecies 2D lattice gas with energy levels: diffusive properties. *Physica D* 47, pp. 169-188.

B. M. Boghosian, D. Levermore (1987) A cellular automaton for Burger' equation. *Complex. Syst.* no. 1, pp.17-30.

J. P. Boon (1991) Statistical mechanics and hydrodynamics of lattice gas automata: An overview. *Physica D*, vol. 47, pp.3-8.

L. Brieger, E. Bonomi (1991) A stochastic cellular automaton simulation of the non-linear diffusion equation. *Physica D*, vol. 47, pp.159-168.

C. Burges, S. Zaleski (1987) Buoyant mixtures of cellular automaton gases. *Complex. Syst.* vpl. 1, pp. 31-50.

C. K. Chan, N. Y. Liang (1990) Critical phenomena in an immiscible lattice-gas cellular automaton. *Europhysics Letters*, vol. 13, no. 6, pp. 495-500.

H. Chen, S. Chen, G. Doolen, Y. C. Lee (1988) Simple lattice gas models for waves. *Complex. Syst.* vol.2, pp. 259-267.

S. Chen, D.O. Martinez, W. H. Mattheus, H. Chen (1992) Magnetohydrodynamics computations with lattice gas automata. *J. Stat. Phys.*, vol. 68, nos. 3/4.

S. Chen, H. Chen, G.G. Doolen, Y. C. Lee, H. Rose (1991) Lattice gas models for nonideal gas fluids. *Physica D*, vol. 47, pp. 97-111.

S. Chen, K. Diemer, G. D. Doolen, K. Eggert, C. Fu, S. Gutman, K. Eggert, B. J. Travis (1991) Lattice gas automata for flow through porous media. *Physica D*, vol. 47, pp. 72-84.

B. Chopard, M. Droz (1990) Cellular automata model for thermo-hydrodynamics, in 'Numerical methods for simulation of multi-phase and complex flow', Proc. of a Workshop held at Koninklijke/Shell-Lab., 30 May-1 June.

P. Clavin, D. d'Humieres, P. Lallemand, Y. Pomeau (1990) Cellular automata for hydrodynamics with free boundaries in two and three dimensions. in "Lattice gas methods for partial differential equations", Eds. Dolen et al., Addison-Wesley Publ. Co.

K. A. Cliffe, R.D. Kingdon, P. Schofield, P.J. Stopford (1991) Lattice gas simulation of free boundary flows. *Physica D*, vol. 47, pp. 275-280.

A. Clouqueur, D. d'Humieres (1987) RAP1, a cellular automaton machine for fluid dynamics. *Complex Syst.* vol.1, pp. 585-597.

R. Cornubert, D. d'Humieres, D. Levermore (1991) A Knudsen layer theory for lattice gases. *Physica D*, vol. 47, pp. 241-259.

B. Dubrulle, U. Frisch, M. Henon, J-P. Rivet (1991) Low-viscosity lattice gases. *Physica D*, vol. 47, pp. 27-29.

M. H. Ernst, S. P. Das, D. Kammann (1990) Heat conductivity in a thermal LGCA. in 'Numerical methods for simulation of multi-phase and complex flow', Proc. of a Workshop held at Koninklijke/Shell-Lab., 30 May-1 June.

U. Frisch, J. P. Rivet (1986) Lattice gas hydrodynamics, Green-Kubo formula. *Comptes Rendus* 303, II, pp. 1065.

U. Frisch, B. Hasslacher, Y. Pomeau (1986) Lattice-gas automata for the Navier-Stokes equation. *Phys. Rev. Lett.*, vol. 56, no.14, pp. 1505-1508.

U. Frisch, D. d'Humieres, B. Hasslacher, P. Lallemand, Y. Pomeau, J-P. Rivet (1987) Lattice gas hydrodynamics in two and three dimensions. *Complex Syst.* no.1, pp. 649-707.

R. Gatignol (1987) The hydrodynamical description for a discrete velocity model of gas. *Complex Syst.* no.1, pp. 709-725.

A. K. Gunstensen, D. H. Rothman (1991) A Galilean-invariant immiscible lattice gas. *Physica D*, vol. 47, pp. 53-63.

R. Gutfraind, A. Hansen (1994) Study of hydrodynamic permeability of fractures using lattice gas automata. *Techn. Rep. Univ. of Trondheim, UNIT*, no.3.

R. Gutfraind, I. Ippolito (1995) Study of tracer dispersion in self-affine fractures using lattice-gas automata. *Phys. Fluids*. vol.7, no.8, pp. 1938-1948.

B. Hasslacher (1987) Discrete fluids. *Los Alamos Science Special Issue* (preprint).

T. Hatori, D. Montgomery (1987) Transport coefficients for magnetohydrodynamic cellular automata. *Complex Syst.* vol. 1, pp.735-752.

F. Hayot (1987) The effect of Galilean non-invariance in lattice gas automaton one-dimensional flow. *Complex Syst.*, no. 1, pp. 753-761.

F. Hayot (1991) Fingering instability in a lattice gas. *Physica D*, vol 47, pp. 64-71.

M. Henon (1987a) Viscosity of a lattice gas. *Complex Syst.* no.1, pp. 763-789.

M. Henon (1987b) Isometric collision rules for the four-dimensional FCHC lattice gas. *Complex Syst.* vol. 1, pp. 475-494.

M. Henon (1992) Implementation of the FCHC lattice gas model on the connection machine. *J. Stat. Phys.*, vol. 68, nos. 3/4, pp. 353-377.

F. Higuera (1990) Modified lattice gas method for high Reynolds number incompressible flows. in "Numerical methods for simulation of multi-phase and complex flow", Proc. of a Workshop held at Koninklijke/Shell-Lab., 30 May-1 June.

M. A. van der Hoef, D. Frenkel (1991) Tagged particle diffusion in 3D lattice gas automata. *Physica D*, vol. 47, pp. 191-197.

D. d'Humieres, P. Lallemand (1987) Numerical simulations of hydrodynamics with lattice gas automata in two dimensions. *Complex. Syst.* no. 1, pp. 599-632.

D. d'Humieres, P. Lallemand, G. Searby (1987) Numerical experiments on lattice gases: Mixtures and galilean invariance. *Complex. Syst.* no. 1, pp. 633-647.

D. d'Humieres, P. Lallemand (1990) Flow of a lattice gas between two parallel plates: Development of the Poiseuille profile. in "Lattice gas methods for partial differential equations", Eds. Dolen et al., Addison-Wesley Publ. Co.

D. Jeulin (1990) Flow and diffusion in random porous media from lattice gas simulations. in "Numerical methods for simulation of multi-phase and complex flow", Proc. of a Workshop held at Koninklijke/Shell-Lab., 30 May-1 June.

L. P. Kadanoff, G. R. McNamara, G. Zanetti (1987) A Poiseuille viscometer for lattice gas automata. *Complex. Syst.* no.1, pp. 791-803.

J. M. V. A. Koelman, M. Nepveu (1990) Darcy flow in porous media: Cellular automata simulations, in "Numerical methods for simulation of multi-phase and complex flow", Proc. of a Workshop held at Koninklijke/Shell-Lab., 30 May-1 June.

G. A. Kohring (1992) The cellular automata approach to simulating fluid flows in porous media. *Physica A*, vol. 186, pp. 97-108.

A. W. Kolmogorov (1941) *C. R. Acad. Sci. USSR*, 30, pp. 301-538.

R. H. Kraichnan (1967) *Phys. Fluids*, 10, pp. 1417.

L. D. Landau and E. M. Lifschitz (1959) *Fluid mechanics*. Pergamon Press. NY.

F. Liu, N. Goldenfeld (1991) Deterministic lattice models for diffusion-controlled crystal growth. *Physica D*, vol. 47, pp. 124-131.

J. F. Lutsko, J. P. Boon, J. A. Somers (1990) Lattice gas automata simulations of viscous fingering in porous media, in "Numerical methods for simulation of multi-phase and complex flow", Proc. of a Workshop held at Koninklijke/Shell-Lab., 30 May-1 June.

P. Manneville, N. Boccara, G.Y. Vichniac, R. Bidaux, eds. (1989) *Cellular automata and modeling of complex physical systems*. Springer-Verlag.

N. Margolus, T. Toffoli (1990) Cellular automata machines. in "Lattice gas methods for partial differential equations", eds. Doolen et al., Addison-wesley Publ. Co.

G. R. McNamara (1990) Diffusion in a lattice automaton. *Europhysics Letters*, vol.12, no.4, pp. 329-334.

P. Mora (1992) The lattice Boltzmann phononic lattice solid. *J. stat. Phys.*, vol. 68, nos. 3/4.

F. R. Mujica-Fernandez (1991) Lattice gas wind tunnel. M.S. Thesis, Dep. Nucl. Eng., MIT, Cambridge, MA.

T. Naitoh, M.H. Ernst, M.A. van der Hoef (1990) Effects of sound modes on the VACF in cellular automaton fluids, in "Numerical methods for simulation of multi-phase and complex flow", Proc. of a Workshop held at Koninklijke/Shell-Lab., 30 May-1 June.

J. von Neumann (1966) Theory of self-reproducing automata. (Univ. of Illinois press),

J. F. Olson (1995) Two-fluid flow in sedimentary rock: complexity, transport and simulation. PhD Thesis, Dep. of Earth, Atms. and Planetary Sciences, MIT, Cambridge, MA.

S. A. Orszag, V. Yakhot (1986) Reynolds number scaling of cellular automaton hydrodynamics. Phys. Rev. Lett., vol. 56, no. 16, pp. 1691-1693.

V. Pot (1994) Microscopical study of flow and phase-change in porous media via lattice gas models. Phd Thesis, Univ. Paris 6, (in french).

Y. H. Qian, D. d'Humieres, P. Lallemand (1992) Diffusion simulation with a deterministic one-dimensional lattice-gas model. J. Stat. Phys., vol. 68, nos. 3/4, pp. 563-573.

F. Reif (1988) Fundamental of statistical and thermal physics. Mc.Graw-Hill, NY.

J. -P. Rivet, U. Frisch (1987) Green-Kubo formalism for lattice gas hydrodynamics and Monte-Carlo evaluation of shear viscosities. Complx. Syst. no. 1, pp. 839-851.

J.-P. Rivet, M. Henon, U. Frisch, D. d'Humieres (1988) Simulating fully three-dimensional external flow by lattice gas methods. Europhysics Letters, vol. 7, no. 3, pp. 231-236.

D. Rothman, J. M. Keller (1988) Immiscible cellular-automaton fluids. J. Stat. Phys., vol. 52, nos. 3/4, pp. 1119-1127.

D. Rothman (1988) Cellular-automaton fluids: A model for flow in porous media. Geophysics, vol. 53, no.4, pp. 509-518.

D. Rothman (1990) Macroscopic laws for immiscible two-phase flow in porous media: Results from numerical experiments. J. Geoph. Res., vol. 95, no. B6, pp. 8663-8674.

D. Rothman (1992) Simple models of complex fluids. in "Microscopic simulations of complex hydrodynamics", eds. M. Marechal and B. Holian, Plenum Press.

D. Rothman, L. P. Kadanoff (1994) Bubble, bubble, boil, and trouble. Comp. Phys., vol. 8, no. 2, pp.199-204.

D. Rothman, S. Zaleski (1994) Lattice gas models of phase separation: interfaces, phase transitions, and multiphase flow. Rev. Mod. Phys., vol. 66, pp.1417-1479.

D. Rothman and S. Zaleski (1996) Lattice-gas cellular automata: Simple models of complex hydrodynamics. (in print).

T. Shimomura, G. D. Doolen, B. Hasslacher, C. Fu (1987) Calculation using lattice gas techniques. Los Alamos Sci., Special Issue, pp. 210-210.

J. A. Somers, P. C. Rem (1990) Obtaining numerical results from the 3D-FCHC lattice gas, in "Numerical methods for simulation of multi-phase and complex flow", Proc. of a Workshop held at Koninklijke/Shell-Lab., 30 May-1 June.

J. A. Sommers, P. C. Rem (1991) Flow computation with lattice gases. in R. V. Oliemans (ed.) *Comp. Fluid Dyn.*, Kluwer Ac. Publ.

J. A. Sommers, P. C. Rem (1991) Analysis of surface tension in two-phase lattice gases. *Physica D*, vol. 47, pp. 39-46.

G. Y. Vichniac (1990) cellular automata and complex systems. in "Microscopic simulations of complex hydrodynamics", eds. M. Marechal and B. Holian, Plenum Press.

G. Zanetti (1990) Lattice gas automata: Comparison of simulation and theory, in "Microscopic simulations of complex hydrodynamics", eds. M. Marechal and B. Holian, Plenum Press.

G. Zanetti (1991) Counting hydrodynamic modes in lattice gas automata. *Physica D*, vol. 47, pp. 30-35.

J.T. Wells, D.R. Janecky, B.J. Travis (1991) A lattice gas automata model for heterogenous chemical reactions at mineral surfaces and in pore networks, *Physica D*, fol. 47, pp.115-123.

S. Wolfram (1986) Cellular automaton fluids 1: Basic Theory. *J. Stat. Phys.*, vol 45, nos.3/4, pp. 471-526.

Lattice-gas Boltzmann

R. Benzi, S. Succi, M. Vergassola (1992) The lattice Boltzmann equation: theory and applications. *Phys. Rep.* 222, no. 3, pp. 145-197, North-Holland.

J.G.M. Eggels, J.A. Sommers (1995) Numerical simulation of free convective flow using the lattice-Boltzmann scheme. *Int. J. Heat and Fluid Flow* (pre-print).

J. G. M. Eggels (1995) Direct and large-eddy simulation of turbulent fluid flow using the lattice-Boltzmann scheme. *Int. J. Heat and Fluid Flow* (pre-print).

U. Frisch (1991) Relation between the lattice Boltzmann equation and the Navier-Stokes equations. *Physica D*, vol. 47, pp. 231-232.

B. Ferreol, D. Rothman (1995) Lattice-Boltzmann simulations of flow through Fontainebleu sandstone. *Trans. in Porous Media*. (pre-print).

I. Ginzbourg, P.M. Adler (1994) Boundary flow condition analysis for the three-dimensional lattice-Boltzmann model. *J. Phys. II, France*, vol. 4, pp. 191-214.

A. K. Gunstensen (1992) Lattice-Boltzmann studies of multi-phase flow through porous media. Phd Thesis, Dep. of Earth Atms. and Planetary Science, MIT, Cambridge, MA.

A. K. Gunstensen, D.H. Rothman (1993) Lattice-Boltzmann studies of immiscible two-phase flow through porous media. *J. Geoph. Res.*, vol. 98, no. B4, pp. 6431-6441.

F.J. Higuera, S. Succi, R. Benzi (1989) Lattice gas with enhanced collisions. *Europhys. Lett.* vol.9, no.4, pp. 345-349.

F. J. Higuera, J. Jimenez (1989) Boltzmann approach to lattice gas simulations. *Europhys. Lett.*, vol.9, no.7, pp. 663-668.

- F.J. Higuera, S. Succi (1989) Simulating the flow around a circular cylinder with a lattice Boltzmann equation. *Europhysics Letters*, vol. 8, no. 6, pp. 517-521.
- R. Holme, D.H. Rothman (1992) Lattice-gas and Lattice-Boltzmann models of miscible fluids. *J. of Stat. Physics*, vol. 68, nos. 3/4, pp. 409-429.
- D. d'Humieres (1992) Generalized lattice Boltzmann equations. (pre print)
- G. R. McNamara, G. Zanetti (1988) Use of the Boltzmann equation to simulate lattice-gas automata. *Phys. Rev. Lett.*, vol.61,no. 20.
- D.R. Noble, S. Chen, J. G. Georgiadis, R. O. Buckius (1995) A consistent hydrodynamic boundary condition for the lattice Boltzmann method. *Phys. of Fluids*, vol. 7, no.1, pp. 203-207.
- U. d'Ortona, D. Salin, M. Cieplak, J.R. Banavar (1995) Interfacial phenomena in Boltzmann cellular automata. *Europhys. Lett.*, vol. 28, no.5, pp. 317-322.
- U. d'Ortona, D. Salin, M. Cieplak, R. Rybka, J.R. Banavar (1995) Two-color nonlinear Boltzmann cellular automata: Surface tension and wetting. *Phys. rev. E*, vol. 51, no.4, pp. 3718-3728.
- R.B. Rybka, M. Cieplak, D. Salin (1995) Boltzmann cellular automata studies of the spinodal decomposition. *Physica A*, vol. 222, pp. 105-118.
- J.P. Rivet, U. Frisch (1986) Lattice gas automata in the Boltzmann approximation. *Compte Rendus* 302, II, pp. 267.
- P. A. Skordos (1995) Modeling flue pipes: Subsonic flow, lattice Boltzmann and parallel distributed computers. Phd Thesis, Dep. Elec. Eng. and Comp. Sci., MIT, Cambridge, MA.
- S. Succi, R. Benzi, F. Higuera (1991) The lattice Boltzmann equation: A new tool for computational fluid-dynamics. *Physica D*, vol. 47, pp.219-230.
- C.M. Teixeira (1992) Continuum limit of lattice fluid dynamics. Phd Thesis, Dep. Nucl. Eng., MIT, Cambridge, MA.

Lattice-gas BGK

- F. J. Alexander, H. Chen, S. Chen, G.D. Doolen (1992) Lattice Boltzmann model for compressible fluids. *Physical Rev. A*, vol. 46, no. 4, pp. 1967-1970.
- O. Behrend, R. Harris, P. B. Warren (1994) Hydrodynamic behavior of lattice Bhatnagar-Gross-Krook models. *Phys. Rev. E*, vol. 50, no.6, pp. 4586-4595.
- O. Behrend (1995) Solid-fluid boundaries in particle suspension simulations via the lattice Boltzmann method. *Phys. Rev. E*, vol.52, no.1, pp.1164-1175.
- B. M. Boghosian, W. Taylor (1995) Correlations and renormalizations in lattice gases. *Phys. Rev. E*, vol. 52, no.1, pp. 510-554.
- H. Chen, S. Chen, W.H. Matthaus (1992) Recovery of the Navier-Stokes equations using a lattice-Boltzmann method. *Phys. Rev. A*, vol. 45, no. 8, pp. 5339-5342.

S. Chen, Z. Wang, X. Shan, G.D. Doolen (1992) Lattice Boltzmann computational fluid dynamics in three dimensions. *J. of Stat. Phys.*, vol. 68, nos. 3/4.

Y. Chen, H. Ohashi, M. Akiyama (1994) Thermal lattice Bhatnagar-Gross-Krook model without nonlinear deviations in macrodynamic equations. *Phys. Rev. E*, vol. 50, no.4, pp. 2776-2783

E.G. Flekkoy, J. Feder, T. Jossang (1992) Lattice gas simulations of osmosis. *J. of Stat. Phys.*, vol. 68, nos. 3/4.

E.G. Flekkoy (1993) Lattice BGK for miscible fluids. (preprint).

E.G. Flekkoy (1993) Modelling miscible fluids. Phd Thesis, Centre for Advance Study, Oslo, Norway.

M. Gerits, M.H. Ernst (1993) Lattice-gas automata with attractive and repulsive interactions. *Phys. Rev. E*, vol. 48, no.2, pp. 988-999.

S. Hou (1995) Lattice Boltzmann method for incompressible viscous flow. Ph.D.. Thesis, Kansas State Univ., Manhattan, Kansas.

J. M. V. A. Koelman (1991) A simple lattice Boltzmann scheme for Navier-Stokes fluid flow. *Europhys. Lett.*, vol. 15, no.6, pp. 603-607.

D. O. Martinez, S. Chen, W.H. Matthaeus (1993) Lattice Boltzmann magneto hydrodynamics. *Phys. Plasmas*, vol.1, no. 6, pp. 1850-1867.

W. Miller (1995) Flow in the driven cavity calculated by the lattice Boltzmann method. *Phys. Rev. E*, vol.51, no.4, pp. 3659-3669.

A.C. Ladd (1990) Hydrodynamic interactions and transport coefficients in a suspension of spherical particles, *Microsc. Sim. of Complex. Flows*, (ed. M. Mareschal), NY.

A.C. Ladd (1991) Dissipative and fluctuating hydrodynamic interactions between suspended solid particles via Lattice-gas Cellular Automata, in M.Meyer and V. Pontikis ed., *Computer Sim. in mat. Sci.*, Kluwer Acad. Pub., pp. 481-504.

A. J. C. Ladd (1993) Short-time motion of colloidal particles: Numerical simulation via a fluctuating lattice-Boltzmann equation. *Phys. Rev. Lett.*, vol. 70, no. 9, pp. 1339-1342.

A.C. Ladd (1994, a) Numerical simulations of particulate suspensions via a discretized Boltzmann equation. Part 1. Theoretical foundation. *J. Fluid Mech.*, vol. 221, pp. 285-309, Cambridge Univ. Press.

A.C. Ladd (1994, b) Numerical simulations of particulate suspensions via a discretized Boltzmann equation. Part 2. Numerical Results. *J. Fluid Mech.*, vol. 221, pp. 285-309, Cambridge Univ. Press.

A. C. Ladd, Hu Gang, J.X. Zhu, D. A. Weitz (1995) Time-dependent collective diffusion of colloidal particles. *Phys. Rev. Lett.*, vol.74, no. 2, pp. 318-321.

A. Lawniczack, D. Dab, R. Kapral, J.P. Boon (1991) Reactive lattice gas automata. *Physica D*, vol.47, pp. 132-158.

D. R. Noble, S. Chen, J. G. Georgiadis, R. O. Buckius (1995) A consistent hydrodynamic boundary condition for the lattice Boltzmann method. *Phys. Fluids*, vol. 7, no. 1, pp. 203-209.

Y. H. Qian, D. d'Humieres, P. Lallemand (1992) Lattice BGK for Navier-Stokes equations. *Europhys. Lett.* vol.17, no. 6, pp. 479-484.

Y. H. Qian, S. A. Orszag (1993) Lattice BGK models for the Navier-Stokes equation: Nonlinear deviation in compressible regimes. *Europhys. Lett.*, vol. 21, no. 3, pp. 255-259.

S. Schwarzer (1995) Sedimentation and flow through porous media: Simulating dynamically coupled discrete and continuum phases. *Phys. Rev. E*, vol. 52, no.6, pp. 6461-6475.

X. Shan, H.Chen (1992) Lattice Boltzmann model for simulating flows with multiple phases and components. *Phys.. Rev. E*, vol. , no. , pp. 1815-1819.

X. Shan, H. Chen (1995) Simulation of non ideal gases and liquid-gas phase transitions by the lattice Boltzmann equation. *Phys. Rev. E*, no. 49, vol.4, pp. 2941-2948.

P.A. Skordos (1993) Initial and boundary conditions for the lattice Boltzmann method. *Phys. Rev. E*, vol. 48, no.6, pp. 4823-4842.

Data Report for the 1995 Wind River Mountains - Green River Basin, Wyoming, Seismic Refraction Profile

**Stephan H. Koester
Boston College
Phillips Laboratory/GPE
29 Randolph Road
Hanscom AFB, MA 01731**

**John J. Cipar
Phillips Laboratory/GPE
29 Randolph Road
Hanscom AFB, MA 01731**

14 May 1996

The 1995 Wind River Mountains - Green River Basin, Wyoming, Seismic Refraction Profile

1.0 Introduction

During the summer of 1995, the Earth Sciences Division of Phillips Laboratory (PL/GPE) undertook an extensive seismic experiment in southwestern Wyoming. The experiment had two parts: (a) recording a seismic refraction profile across the Green River Basin using explosions fired east of Lander, Wyoming as part of the Deep Probe experiment; and (b) installation and operation of a large-aperture array during August and September. A description of the technical aspects of the refraction profile is the subject of this first report; a separate report covers data recorded by the large-aperture array.

In August, 1995, several US and Canadian universities along with the Canadian Geological Survey performed the Deep Probe Experiment, an ultra-large scale active seismic experiment in western North America (Henstock et al, 1995). The main Deep Probe profile was oriented north-south from Edmonton, Alberta, to Crownpoint, New Mexico, a distance of 1900 km. An intermediate shot point was located approximately 50 km east of Lander, Wyoming, and provided the sources for the Wind River Mountains - Green River Basin Seismic Refraction Profile described in this report. This profile consisted of 47 shot-station points extending from Big Sandy, Wyoming, west to the Idaho-Wyoming border, a distance of about 150 km.

We plan to use the data from this experiment to study:

- regional wave propagation in the central Rocky Mountains
- spatial variability of earthquake/explosion discriminants
- crustal structure beneath the Wind River Mountains and Green River Basin

2.0 Previous Geophysical Work

The Green River Basin is an extensive Cenozoic sedimentary basin bounded by the Precambrian Wind River Mountains on the east, the Wyoming Range on the west, and the Uinta Mountains of Utah to the south. The southern part of the basin contains the Mesozoic Rock Springs uplift. While the underlying rocks are of various ages, the overall structure of mountain bounded basin was formed during the late Cretaceous-early

Tertiary Laramide orogeny. The Wind River Mountains are a thrust-faulted basement anticline that over rode the eastern part of the Green River basin (Smithson et al, 1979).

The Green River basin abuts the eastern edge of the Intermountain Seismic Belt with considerable seismicity to the south and west of the basin (Pechmann et al, 1995). Previous geophysical studies include a seismic refraction profile from American Falls Reservoir, Idaho, to Flaming Gorge Reservoir, Wyoming, with an intermediate shot point at Bear Lake, Idaho-Utah (Prohdel, 1979). Pechmann et al (1995) use the Prohdel (1979) P-wave velocity-depth model to infer S-wave velocities and densities. This model has crustal thickness of 40 km and is underlain by 7.9 km/s mantle material. Braile et al (1974) interpreted a single-ended refraction profile extending from the Bingham Canyon copper mine near Salt Lake City, Utah, across the Green River Basin to the Wind River Mountains. They infer that the crustal thickness is 40 km or greater beneath the Green River Basin and southern Rocky Mountains. Smithson et al (1979) and Brewer et al (1980) discuss COCORP deep seismic reflection data collected across the southern end of the Wind River Mountains and adjacent Green River and Wind River Basins. These observations indicate the shallow overthrust nature of the Wind River Mountains.

3.0 The Wind River Mountains - Green River Basin Seismic Refraction Profile

The Wind River Mountains - Green River Basin Seismic Refraction Profile was deployed during the Deep Probe project of August 1995 to image the crustal structure beneath the Wind River Mountains and the Green River Basin. Unlike the Deep Probe profiles, the Wind River Mountains - Green River Basin Seismic Refraction Profile was oriented east-west. The refraction profile begins on the west side of the Wind River Mountains, 135 km from the quarry, and extends in the general azimuth of 265° across the Green River Basin and the Wyoming Range to a total distance of about 280 km from the quarry (Figure 1). A total of 47 stations were installed, spaced approximately 3.2 km apart from each other.

The refraction study utilized two Deep Probe explosions east of Lander, Wyoming, as its energy source. The first explosion (labeled 143) was about 15,000 lbs. of ammonium nitrate/fuel oil (ANFO) detonated on the bottom of a water filled quarry (G. R. Keller personal communication). The second explosion (labeled 243) was fired one week later with

approximately the same amount of ANFO in the same location (Table 1). The large source size and excellent coupling in the quarry provided exceptional signal-to-noise ratios across the profile.

3.1 Installation and Instrumentation of the Profile

Three different types of portable stations were deployed along the profile (Table 2). Figure 2 shows the basic setup of a refraction profile station. In particular, the station setup displayed uses RefTek and GeoSpace instruments, but can also be used as a general guideline for every station configuration used in the profile. Common to each configuration is a seismometer buried about one foot deep, a data acquisition recorder, a power supply, and a timing system.

The first configuration consisted of 3 component, 1.0 Hz GeoSpace HS-10-1b seismometers recorded and digitized by a 24 bit Refraction Technology data acquisition system (DAS). The DAS contained a hard disk drive to store the digitized signal and was powered by two 12v gel cells. A global positioning satellite (GPS) clock was connected to the DAS to provide accurate timing and geographic location. The DAS was set up to record a continuous single data stream at 100 samples per second consisting of 3 data channels at 24 bit resolution with a preamplifier gain of 32. The nominal sensitivity of the HS-10-1b seismometer is 600 v/m/sec.

The second station configuration deployed along the profile included a single vertical component 1.0 Hz GeoSpace HS-10/1b seismometer digitized by a Terra Technology recorder with WWVB radio timing. The Terra Technology recorders used an alarm clock to start data acquisition before the anticipated chemical explosion. Once triggered, the recorders acquired data for about 10 to 15 minutes and stored the data onto a cassette tape. The Terra Technology recorders were set to record one data channel with 12 bit resolution using a static gain of either 100 or 1000 at 100 samples per second.

The final station configuration consisted of 1.0 Hz MARK-L-4C-3D geophones recorded and digitized by a Teledyne Brown Engineering Portable Data Acquisition System (PDAS). The PDAS used GPS for both timing and geographic location. The PDAS system was configured to record for 15 minutes starting at the shot origin time. The parameters were set to acquire 3 data channels at 14/2 bit resolution with a preamplifier gain of 1 at 100 samples per second. The PDAS data was later resampled at 125 samples per second to conform with other Deep Probe data sets.

In addition, data from three large aperture array stations are included in the data set. These stations are spaced approximately 50 km from each other in nearly a straight line and are located in the same azimuth as the refraction profile.

3.2 Operation of Profile

The profile was deployed in two stages to increase the offset from the shot point. Since the two chemical explosions were at the same location, all of the instruments were re-deployed to different locations along the profile resulting in a longer and denser profile. The first deployment occurred on August 8th, one day before the first ANFO detonation. Fourteen stations were installed for this deployment. Seven stations were equipped with RefTek recorder configurations and seven stations were equipped Terra Technology recorder configurations. The deployment of stations began at the entrance to the Bridger National Forest with a Refraction Technology recorder configuration, continued through the national forest alternating recorder configurations, and ended at the border of Wyoming and Idaho with a Terra Technology recorder configuration. The stations were removed the following day (August 9th) in the reverse order in which they were deployed. Thus, the stations that were retrieved first include less data than those retrieved last.

The second deployment occurred on August 16th, one day before the second explosion. Thirty three stations were deployed including Refraction Technology, Terra Technology and PDAS recording configurations. The second deployment stretched from the edge of the Wind River Mountains west to the entrance of the Bridger National Forest. The stations were removed the following day on August 17th.

Stations were located along existing roads which necessitated several jogs of up to 3 km from the profile azimuth. A vehicle odometer was used to deploy the stations, then the latitude and longitude were measured using a hand-held GPS receiver. The final geographic locations listed in Table 2 are obtained by taking multiple RefTek GPS locations at each site. Individual GPS locations not within the $L1 - \sigma$ of the median location at each site were discarded. The remaining GPS locations were averaged to give a final location. Final geographic locations for sites that either did not have a RefTek GPS installed, or did not receive more than 5 RefTek GPS locations, were picked off a USGS 30X60 minute quadrangle map. At each station, the sensors were placed in shallow holes, leveled and then covered to reduce wind noise. The recording instruments were placed

several feet from the sensors and were then sheltered from the sun by using garbage bags and vegetation cover to avoid over-heating.

3.3 Profile Data

The data from both Wyoming Deep Probe explosions have been combined to form a seismic profile that extends from about 134 km to 280 km from the source (Figure 3). The whole profile displays exceptionally high signal-to-noise ratios due to the large source size and excellent coupling in the quarry. Unfortunately, other Deep Probe shots outside Wyoming were of only marginal quality in our data and are not shown. The complete profile data set is currently archived in SAC format on Exabyte tape and is currently available from us at Phillips Laboratory. We intend to archive the data at the IRIS Data Management Center at a later date.

The Wind River Mountains - Green River Basin Seismic Refraction Profile can be used for a variety of seismic studies due to similar source properties of both blasts. We verified the similarity of both sources by comparing seismograms from each shot recorded at the same location. Stations 33 and 34 (Table 2) were occupied for the first and second blast, respectively. Both stations are at the same location and both were equipped with Refraction Technology recorders and HS-10 seismometers. Figure 4a shows time domain traces from the two blasts. The only obvious difference is the peak at 108 seconds in blast #1 (upper panel) which is not evident in blast #2 (lower panel). Otherwise, the two waveforms are relatively similar. To more accurately determine the differences between the two blasts, spectral amplitudes of the entire blast, the P-wave, and a pre-event ambient noise sample are examined (Figures 4b - 4d). Figure 4b shows the spectral amplitudes of a six minute window around the blasts. The energy of both blasts is predominantly in the 1.0 - 8.0 Hz frequency band. Within this frequency band, the blasts contain different spectral amplitude peaks. The most notable is that blast #1 (upper panel) contains a higher amplitude peak at 1.0 Hz while blast #2 (lower panel) contains a higher peak at 6.0 Hz. Figure 4c examines the spectral amplitudes of only the P-wave. In this figure, blast #2 displays a more prominent peak at 3.0 and 7.0 Hz, while blast #1 shows a peak at around 4.5 Hz. Figure 4d displays the spectral amplitudes of a 50 second pre-event noise sample. Most of the noise occurs between 0.0 and 1.0 Hz (which is not within the 1.0 - 8.0 Hz frequency band in which the seismic signal resides). In addition, the seismic noise is also an order of magnitude smaller in amplitude than the seismic signal. The preliminary spectral study confirms that although the seismic signals are not identical, the signals from both

blasts have enough similarity to justify combining both data sets for this refraction study.

4.0 Future Work

This report documents the Wind River Mountains - Green River Basin Seismic Refraction Profile data set using 2 large chemical explosions east of Lander, Wyoming as the source. The chemical explosions were recorded across the Wind River Mountains and Green River Basin of southwestern Wyoming. We plan to use this data set to constrain the crustal model for the region using one and two dimensional travel time and waveform modeling. Finally, the seismograms will be archived for use by other investigators.

5.0 Acknowledgments

We would like to thank the following people for their help in making this a successful experiment: The Wyoming field crew including James Steeves, Jim Cipar, Frank & Petra Lorenz, Jose Granillo, Eileen O'Pray and Tom Anderson; Bill Lanning at the Pinedale Bureau of Land Management for help in station scouting and BLM permits; Greg Clark and Jim Wickel, Big Piney and Kemmerer USFS District Rangers in Wyoming, for facilitating station installation on Forest Service land; Andrew Gorman at the University of British Columbia for help in pre-processing the PDAS data; Dru Roberts, Jim and Jane Roscoe, and Myles McGinnis for generously hosting the seismic sites in Wyoming; Dr. Randy Keller and Dr. Steven Harder of the University of Texas at El Paso for guidance throughout the experiment; and Bill Clement of the Earth Sciences Division of Phillips Laboratory for the final editing of this report. We would also like to thank Dr. Stanley Dickinson of the Air Force Office of Scientific Research for moral support and the funding necessary to make this experiment possible.

6.0 References

- Braile, L. W., R. B. Smith, G. R. Keller, R. M. Welch, and R. P. Meyer (1974). Crustal Structure Across the Wasatch Front from Detailed Seismic Refraction Studies, *Jour. Geophys. Res.*, 79, 2669-2677
- Brewer, J., S. B. Smithson, S. Kaufman, and J. Oliver (1980). The Laramide Orogeny: Evidence from the COCORP deep crustal seismic

profiles in the Wind River Mountains, Wyoming, *Tectonophysics*, 62, 165-189.

Henstock, T. J., A. Levander, G. R. Keller, K. C. Miller, E. D. Humphreys, L. W. Braile, R. M. Clowes, and R. M. Ellis (1995). The 1995 US Deep Probe Seismic Experiment: Overview and Controlled Source Results, *EOS (Trans. Am. Geophys. Union)*, 76, F399.

Koester, S. H., J. J. Cipar, J. R. Steeves, J. A. Cipar, F. Lorenz, P. Lorenz, J. Granillo, E. M. O'Pray, T. Anderson (1995). The Western Wyoming Seismic Refraction Profile, *EOS (Trans. Am. Geophys. Union)*, 76, F401.

Pechmann, James C., William R. Walter, Susan J. Nava, and Walter J. Arabasz (1995). The February 3, 1995, M_L 5.1 Seismic Event in the Trona Mining District of Southwestern Wyoming, *Seism. Res. Lett.*, 66, 25-40.

Prodehl, Claus (1979). Crustal Structure of the Western United States, US Geological Survey Professional Paper 1034, 74p.

Smithson, S. B., J. A. Brewer, S. Kaufman, J. E. Oliver, and C. A. Hurich (1979). Structure of the Laramide Wind River Uplift, Wyoming, from COCORP Deep Reflection data and from Gravity Data, *Jour. Geophys. Res.*, 84, B11, 5955-5972.

List of Tables

1.	Shot Locations	106
2.	Station Locations	107

Table 1. Shot Locations

Shot#	Date	Time (GMT)	Latitude	Longitude	Elev. (m) ¹	Depth (m) ²
143	08-09-95	11:30:00.000	42.731 N	107.667 W	1958.0	46.0
243	08-17-95	11:30:00.000	42.730 N	107.665 W	1958.0	46.0

¹Elevation refers to quarry water level relative to sea level.
²Depth refers to distance between quarry water level and quarry bottom where the ANFO was detonated.

Table 2. Station Locations

Station #	Latitude	Longitude	Z (m)	Recorder	# of Channels	Data Available
1	42 32.09 N	109 12.54 W	2450	TerraTek	1	No
2	42 33.84 N	109 14.85 W	2425	TerraTek	1	No
3	42 34.20 N	109 17.14 W	2430	TerraTek	1	Yes
4	42 33.13 N	109 19.45 W	2350	TerraTek	1	Yes
5	42 33.58 N	109 21.80 W	2200	TerraTek	1	No
6	42 36.73 N	109 24.11 W	2250	PDAS	3	Yes
7	42 37.32 N	109 26.36 W	2250	TerraTek	1	Yes
8	42 36.67 N	109 28.70 W	2190	TerraTek	1	Yes
9	42 36.92 N	109 31.13 W	2180	PDAS	3	Yes
10	42 35.42 N	109 33.50 W	2200	PDAS	3	Yes
11	42 33.65 N	109 35.78 W	2215	PDAS	3	Yes
12	42 36.22 N	109 38.20 W	2200	PDAS	3	Yes
13	42 36.05 N	109 40.57 W	2210	PDAS	3	Yes
14	42 36.17 N	109 42.88 W	2200	PDAS	3	Yes
15	42 36.33 N	109 45.22 W	2150	PDAS	3	Yes
16	42 35.95 N	109 48.64 W	2120	PDAS	3	Yes
17	42 36.07 N	109 49.97 W	2100	PDAS	3	Yes
18	42 35.99 N	109 52.18 W	2100	PDAS	3	Yes
19	42 35.44 N	109 54.54 W	2100	PDAS	3	Yes
20	42 33.95 N	109 56.90 W	2110	PDAS	3	Yes
21	42 34.68 N	109 59.27 W	2110	PDAS	3	Yes
22	42 34.67 N	110 01.53 W	2120	PDAS	3	Yes
23	42 34.80 N	110 03.20 W	2110	PDAS	3	Yes
24	42 34.07 N	110 06.24 W	2100	PDAS	3	Yes
25	42 32.67 N	110 08.59 W	2100	PDAS	3	Yes
26	42 32.59 N	110 10.96 W	2125	PDAS	3	Yes
27	42 32.44 N	110 13.28 W	2150	PDAS	3	Yes
28	42 32.37 N	110 15.62 W	2190	RefTek	3	Yes
29	42 32.44 N	110 18.01 W	2250	RefTek	3	Yes
30	42 31.92 N	110 20.35 W	2250	RefTek	3	Yes
31	42 31.56 N	110 22.75 W	2300	RefTek	3	Yes
32	42 31.61 N	110 24.99 W	2300	RefTek	3	No
33	42 30.71 N	110 28.60 W	2380	RefTek	3	Yes
34	42 30.71 N	110 28.60 W	2380	RefTek	3	Yes
35	42 30.48 N	110 31.03 W	2450	TerraTek	1	Yes
36	42 28.92 N	110 33.06 W	2500	RefTek	3	Yes
37	42 27.50 N	110 35.29 W	2500	TerraTek	1	No
38	42 28.82 N	110 37.50 W	2500	RefTek	3	Yes
39	42 30.29 N	110 40.34 W	2600	TerraTek	1	No
40	42 31.68 N	110 42.20 W	2650	RefTek	3	No
41	42 31.63 N	110 44.65 W	2450	TerraTek	1	Yes
42	42 29.69 N	110 48.12 W	2350	RefTek	3	Yes
43	42 29.38 N	110 50.50 W	2300	TerraTek	1	No
44	42 30.61 N	110 53.05 W	2250	RefTek	3	Yes
45	42 29.17 N	110 55.12 W	2150	TerraTek	1	Yes
46	42 23.99 N	111 00.46 W	1950	RefTek	3	Yes
47	42 24.14 N	111 02.70 W	1950	TerraTek	1	Yes

Table 2. (Continued)

Merna Jct	42 56.34 N 110 20.79 W 2340	RefTek	3	Yes
Big Sandy	42 37.91 N 109 28.04 W 2200	RefTek	3	Yes
Big Piney	42 32.06 N 110 16.53 W 2250	RefTek	3	Yes
Fontenelle	42 05.44 N 110 10.06 W 2000	RefTek	3	Yes
Allred	42 29.55 N 110 57.74 W 1900	RefTek	3	Yes

List of Figures

- FIGURE 1. Location map. The Green River refraction profile is shown by the heavy dashed line. The Wyoming shot points are denoted by the star SE of Riverton. The profile was selected to take advantage of large-aperture array stations (house symbol). Dotted lines indicate approximate location of the Wind River and Wyoming Range Mountains.
- FIGURE 2. Refraction Station Schematic. Stations consisted of sensor, recorder, battery power, and timing system. The arrangement for a Refraction Technology recorder station is shown here.
- FIGURE 3. Green River Seismic Profile record section. Data from both shots are displayed in trace normalized record section format reduced at 6 km/sec. East (Big Sandy) is to the left; the right side is at the Idaho-Wyoming border.
- FIGURE 4a. Seismograms from co-located stations for shot 143 (upper panel) and 243 (lower panel). Windows for noise and P-wave spectra are shown at bottom.
- FIGURE 4b. Amplitude spectra for entire window shown in Figure 4a. Most of the energy is between 0.5 and 8 Hz, although spectral peaks are different.
- FIGURE 4c. Amplitude spectra for P-wave window (see Figure 4a). Main peaks correlate in frequency, but not in amplitude. Note extra energy at ~5 Hz for shot 143.
- FIGURE 4d. Amplitude spectra for noise window (see Figure 4a). Noise is predominantly below 1 Hz and is a factor of 200 less than the signal in the 2 - 4 Hz range.

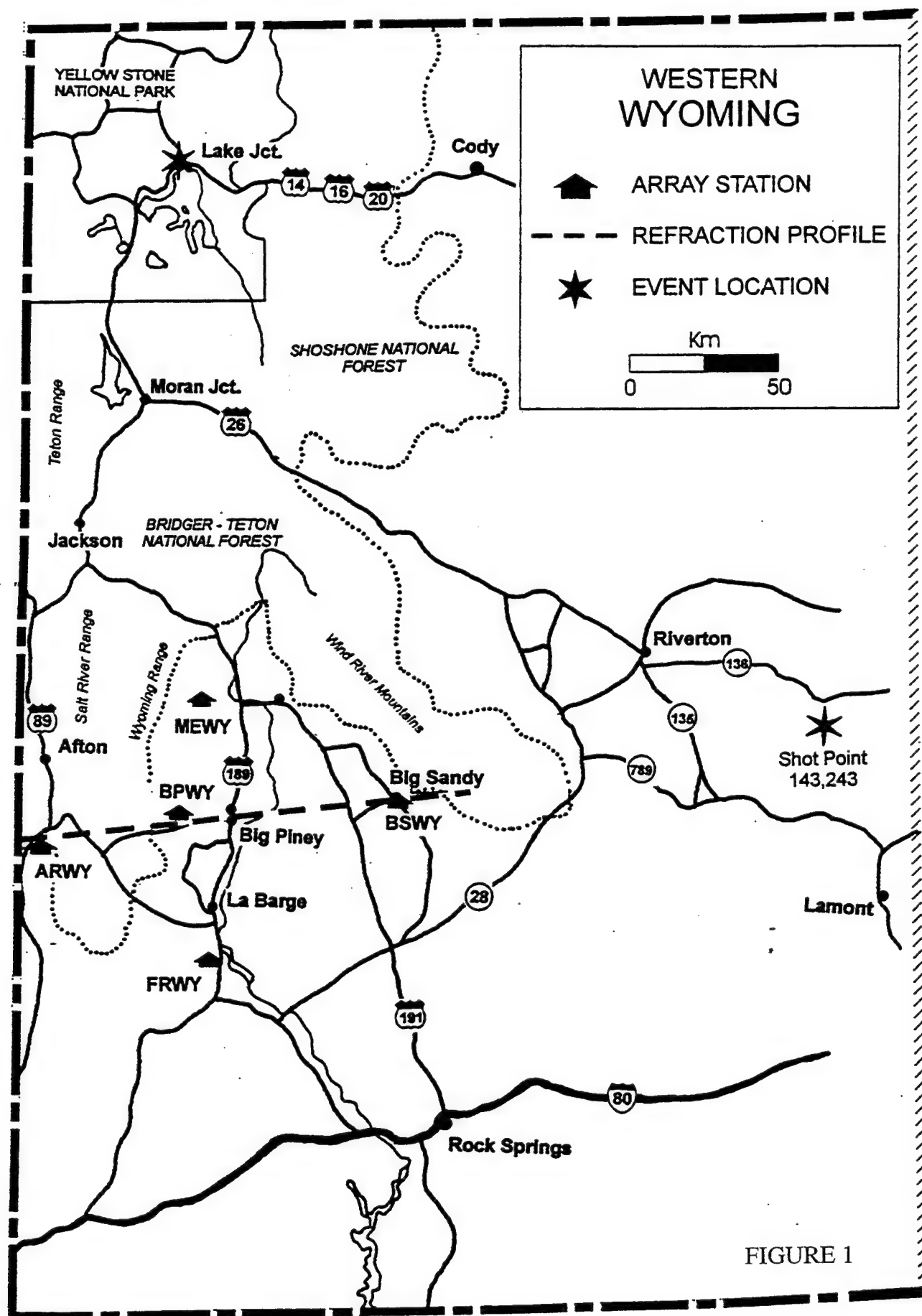


FIGURE 1

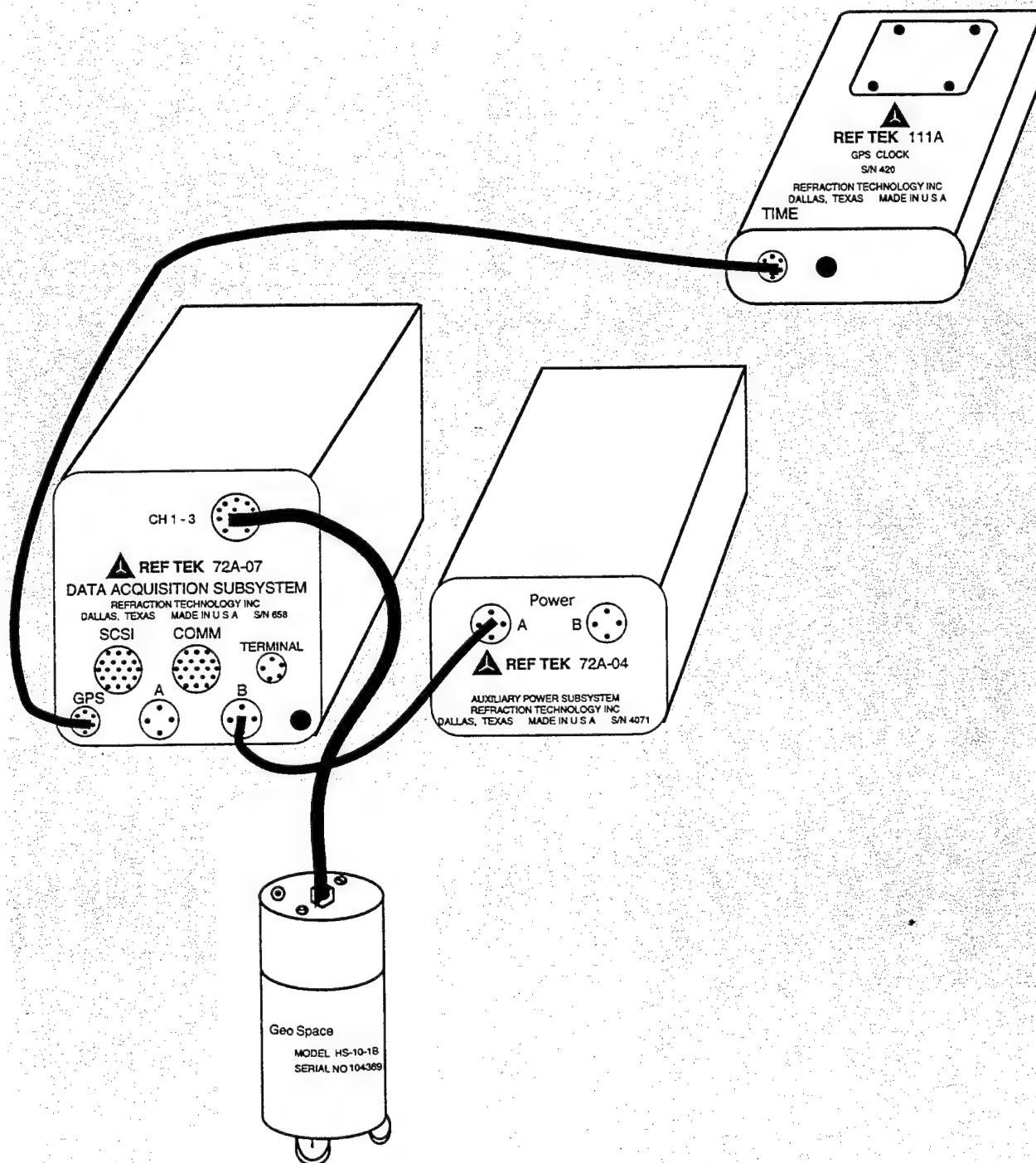


FIGURE 2

112

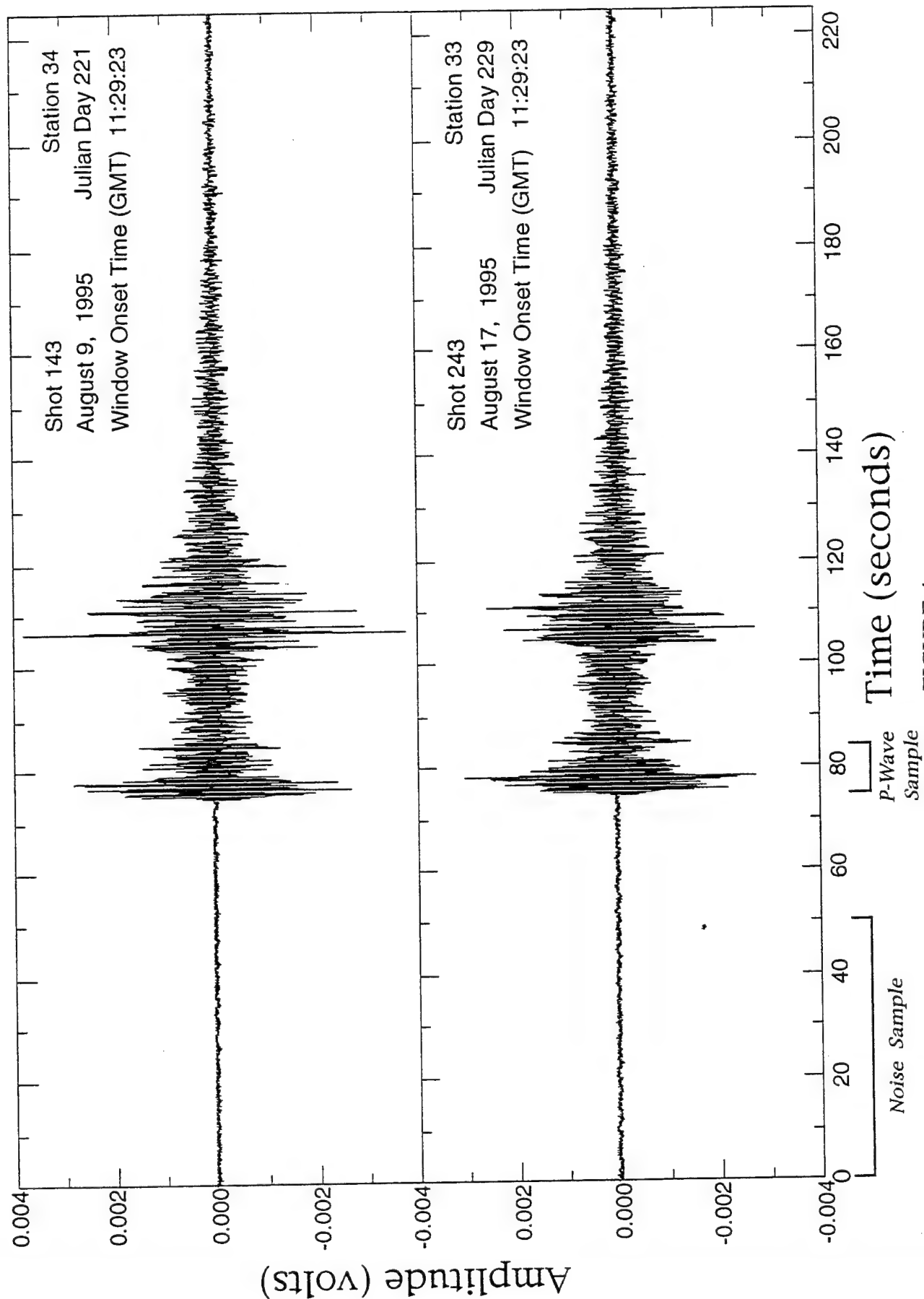


FIGURE 4a

ENTIRE WINDOW

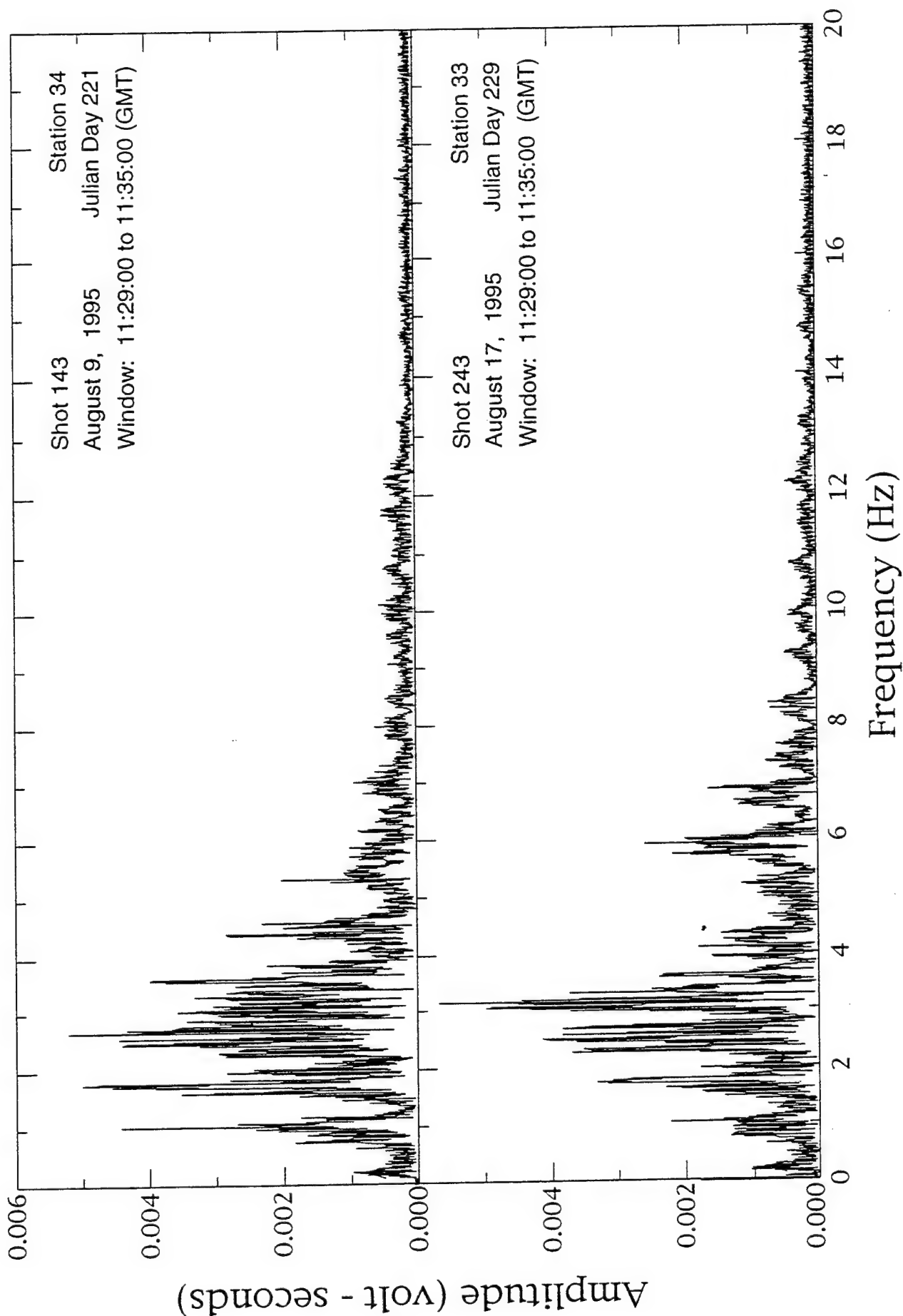


FIGURE 4b

P-WAVE WINDOW

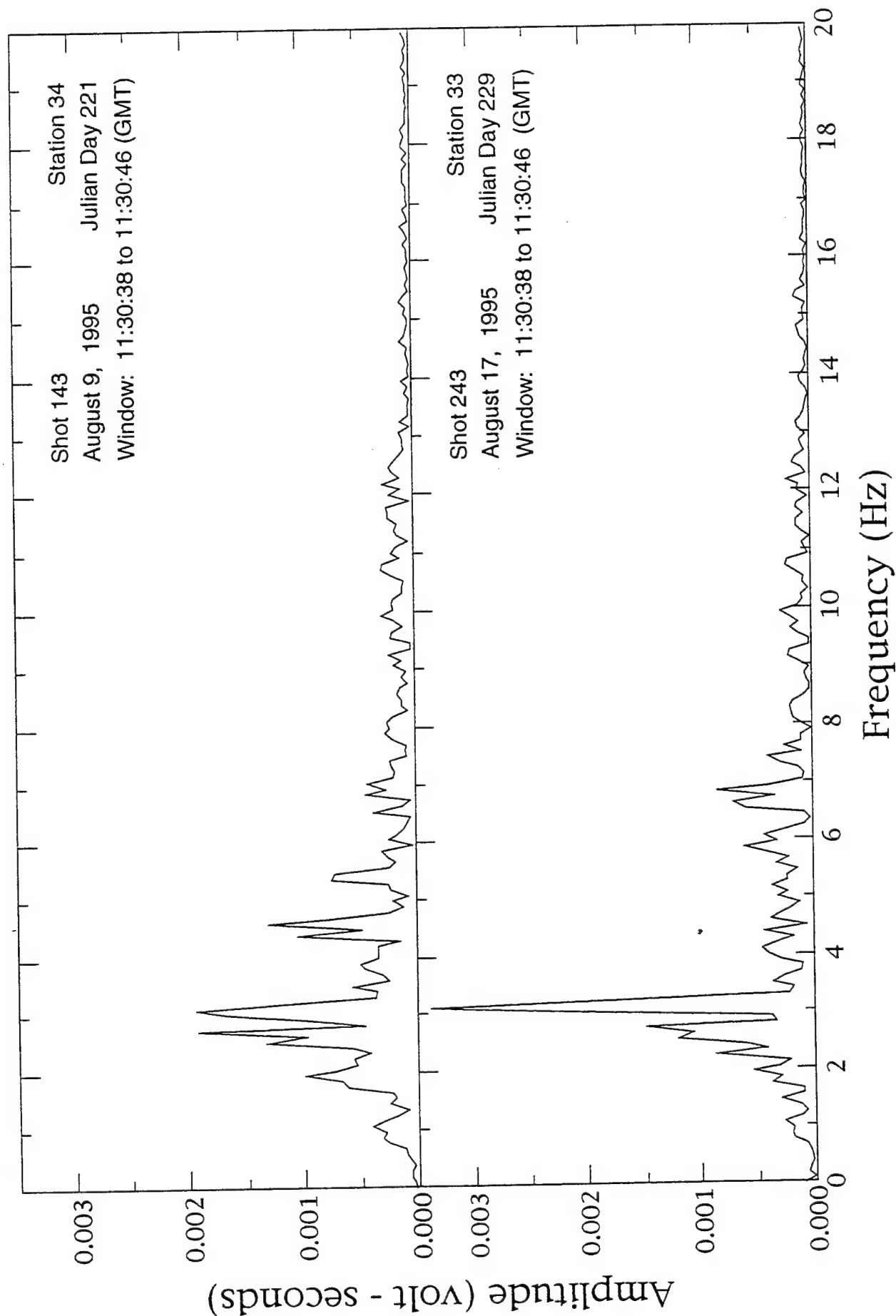


FIGURE 4c

PRE-EVENT NOISE WINDOW

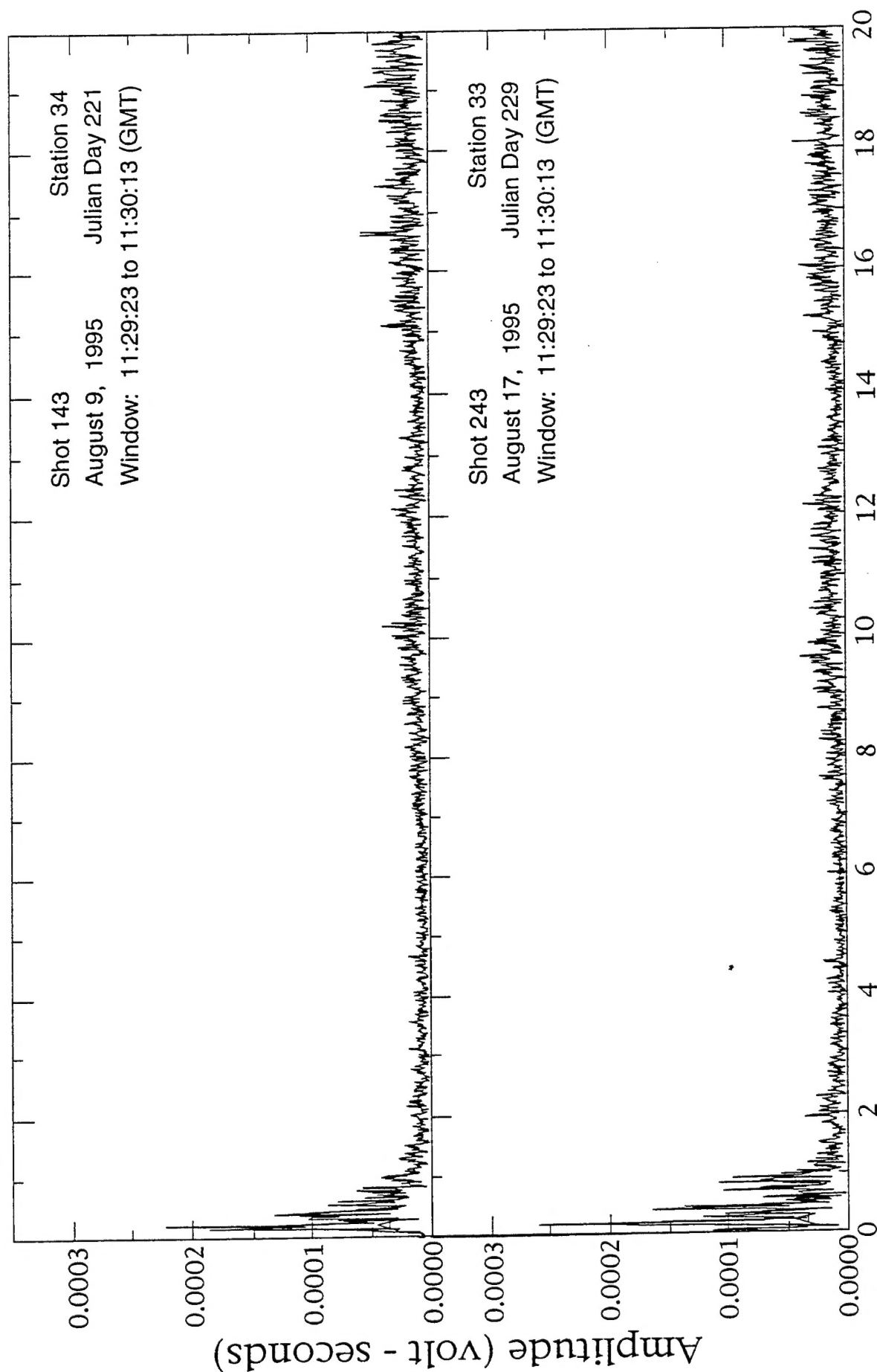


FIGURE 4d

WILLIAM CLEMENT
PL/GPE
29 RANDOLPH ROAD
HANSCOM AFB, MA 01731-3010

CAPT MICHAEL CHIPLEY
AFOSR/NA
110 DUNCAN AVENUE
BOLLING AFB, DC 20332-0001

ANTHONY ENDRES
PL/GPE
29 RANDOLPH ROAD
HANSCOM AFB, MA 01731-3010

LT. MIKE GEER
ARMSTRONG LAB/EQW-OL
139 BURNS DRIVE, SUITE #2
TYNDALL AFB, FL 32403

DAVID JOHNSON
OFFICE OF NAVAL RESEARCH
CODE 4513
800 NORTH QUINCY STREET
ARLINGTON, VA 22217-5660

JANE LONG
E.O. LAWRENCE BERKELEY NATIONAL LAB
UNIVERSITY OF CALIFORNIA
BLDG. 90/1114
BERKELEY, CA 94720

ALDO T. MAZZELLA
U.S. ENVIRONMENTAL PROTECTION AGENCY
ENVIRONMENTAL MONITORING SYSTEMS LAB.
P.O. BOX 93478
LAS VEGAS, NV 89193-3478

STEVEN J. CARDIMONA
PL/GPE
29 RANDOLPH ROAD
HANSCOM AFB, MA 01731-3010

STEVEN A. JOHNSON
TECHNISCAN, INC.
958 WEST LEVOY DRIVE
SUITE 200
SALT LAKE CITY, UT 84123

MUNG YUEN
AFCEE/ERCE
8004 CHENNAULT ROAD
BROOKS AFB, TX 78235-5359

ROBERT F. BALLARD JR.
WATERWAYS EXPERIMENT STATION
3909 HALLS FERRY ROAD
VICKSBURG, VA 39180-6199

ALLEN H. COGBILL
LOS ALAMOS NATIONAL LAB.
PO BOX 1663, MS C335
LOS ALAMOS, NM 87545

T. GREGORY GATES
MISSION RESEARCH CORPORATION
1720 RANDOLPH ROAD, SE
ALBUQUERQUE, NM 87106-4245

F. PETER HAENI
USGS
WATER RESOURCES DIVISION
450 MAIN STREET, ROOM 525
HARTFORD, CT 06103

KATHARINE KADINSKY -CADE
PHILLIPS LABORATORY/GPE
29 RANDOLPH ROAD
HANSCOM AFB, MA 01731-3010

NAFI TOKSOZ
MIT/EARTH RESOURCES LABORATORY
42 CARLETON STREET
CAMBRIDGE, MA 02142

DAVID T. BORUP
TECHNISCAN, INC
958 WEST LEVOY DRIVE
SUITE 210
SALT LAKE CITY, UT 84123

RUSSELL S. HARMON
UNITED STATES ARMY
RESEARCH OFFICE
RESEARCH TRIANGLE PARK, NC 27709-2211

WARREN BARRASH
BOISE STATE UNIVERSITY
1910 UNIVERSITY DRIVE
CGISS, MG206
BOISE, ID 83725

DEFENSE TECHNICAL INFORMATION CENTER
8725 JOHN J. KINGMAN ROAD
FT BELVOIR, VA 22060-6218 (2 COPIES)

PHILLIPS LABORATORY
ATTN: GPBP
29 RANDOLPH ROAD
HANSCOM AFB, MA 01731-3010

PHILLIPS LABORATORY
ATTN: GPE
29 RANDOLPH ROAD
HANSCOM AFB, MA 01731-3010

PHILLIPS LABORATORY
ATTN: TSML
5 WRIGHT STREET
HANSCOM AFB, MA 01731-3004

PHILLIPS LABORATORY
ATTN: PL/SUL
3550 ABERDEEN AVE SE
KIRTLAND, NM 87117-5776 (2 COPIES)

DWAIN K. BUTLER
UNITED STATES ARMY
ENG. WATERWAYS EXP. STATION
3909 HALLS FERRY ROAD
VICKSBURG, MS 39180

JOHN O. CURTIS
UNITED STATES ARMY
ENG. WATERWAYS EXP. STATION
3909 HALLS FERRY ROAD
VICKSBURG, MS 39180

EARL V. EDRIS
UNITED STATES ARMY
ENG. WATERWAYS EXP. STATION
3909 HALLS FERRY ROAD
VICKSBURG, MS 39180

BEN G. FITZPATRICK
NORTH CAROLINA STATE
BOX 8205
RALEIGH, NC 27695-8205

BRIAN J. HARKINS
ROME LABORATORY/ERCS
31 GRENIER STREET
HANSCOM AFB, MA 01731-3010

JAMES F. LEWKOWICZ
PL/GPE
29 RANDOLPH ROAD
HANSCOM AFB, MA 01731-3010

ROSEMARY J. KNIGHT
UNIVERSITY OF BRITISH COLUMBIA
129-2219 MAIN MALL, U.B.C.
VANCOUVER, B.C. V6T 1Z4

JOHN F. LENNON
ROME LABORATORY/ERC
31 GRENIER ST.
HANSCOM AFB, MA 01731-3010

REX MOREY
APPLIED RESEARCH ASSOCIATES
BOX 120A, WATERMAN ROAD
SOUTH ROYALTON, VT 05068

JACK MURPHY
S-CUBED
MAXWELL LABORATORY
11800 SUNRISE VALLEY DR., SUITE 1212
RESTON, VA 22091

BRUCE NIELSEN
ARMSTRONG LABORATORIES/EQW
139 BARNES DRIVE
SUITE 2
TYNDALL AFB, FL 32403-5323

GARY R. OLHOEFT
COLORADO SCHOOL OF MINES
DEPT. OF GEOPHYSICS
1500 ILLINOIS STREET
GOLDEN, CO 80401-1887

JEFF W. RISH III
WRIGHT LABORATORIES/FIVCO-OL
139 BARNES DRIVE
SUITE 2
TYNDALL AFB, FL 32403-5323

MARTIN L. SMITH
NEW ENGLAND RESEARCH
76 OLCOTT DRIVE
WHITE RIVER JUNCTION, VT 05001

VICTOR F. LABSON
U.S. GEOLOGICAL SURVEY
BOX 25046 FEDERAL CENTER
MS 964
DENVER, CO 80225

DALE F. MORGAN
MIT/EARTH RESOURCES LABORATORY
42 CARELTON STREET
BLDG. E34-462
CAMBRIDGE, MA 02142

ARJE NACHMAN
AFOSR/NA
110 DUNCAN AVE.
BOLLING AFB, DC 20332

• IJ WON
• GEOPHEX, LTD.
605 MERCURY STREET
RALEIGH, NC 27603-2343

DAVID L. WRIGHT
U.S. GEOLOGICAL SURVEY
MS 964, BOX 25046
FEDERAL CENTER
DENVER, CO 80225

BOSTON COLLEGE OFFICE OF RESEARCH
ADMINISTRATION
140 COMMONWEALTH AVE.
MIDDLESEX COUNTY
CHESTNUT HILL, MA 02167

YUN WANG
ARMSTRONG LABORATORY/OES
8308 HAWKS ROAD
BROOKS AFB, TX 78235